Master's thesis

NTNU
Norwegian University of Science and Technology
Faculty of Engineering
Department of Energy and Process Engineering

Simen Aleksander Rolland Ormstad

Digital Twin for Compressor Systems

Inlet Guide Vanes Impact on Performance

Master's thesis in Energy and Environment
Supervisor: Lars Eirik Bakken
Co-supervisor: Erik Langørgen
June 2023

NTNU
Norwegian University of
Science and Technology

Simen Aleksander Rolland Ormstad

Digital Twin for Compressor Systems

Inlet Guide Vanes Impact on Performance

Master's thesis in Energy and Environment
Supervisor: Lars Eirik Bakken
Co-supervisor: Erik Langørgen
June 2023

Norwegian University of Science and Technology
Faculty of Engineering
Department of Energy and Process Engineering

NTNU
Norwegian University of
Science and Technology

Preface

I would like to thank my supervisor Professor Lars Eirik Bakken for frequent guidance and invaluable insights during this work and for helping me stay on track. I would also like to thank Senior Engineer Erik Langørgen for all the support at the test facility. At last, I would like to thank my fellow students for motivating discussions, important insights, and great collaboration.

Abstract

This research investigates the application of Digital Twin (DT) technology to enhance the efficiency of centrifugal compressors, critical components in power generation and processing industries. Utilizing the Compressor Test Lab at the Norwegian University of Science and Technology (NTNU), the study provides valuable validation data for a future DT model and insights into compressor operations and behaviors.

The research primarily aimed to establish an accurate compressor map under thermally stable conditions for a precise DT model and to simulate different compressor deterioration scenarios by varying the Inlet Guide Vanes (IGV) angles. Precise prediction of Time to Surge (TTS) and Time in Surge (TIS) was of central interest as critical indicators of potential surge-induced damage.

A detailed compressor map was developed using static tests under thermally stable conditions, effectively bridging the physical system and its digital counterpart. Following this, transient tests were conducted to study TTS, Head Rise to Surge (HRTS), and TIS under different operational scenarios. Several methods were implemented to determine the onset of surge accurately.

Significantly, the transient tests revealed a relationship between HRTS and TTS. It was observed that higher HRTS results in a longer TTS, providing a broader safety margin before surge onset. Additionally, a higher HRTS can counterbalance the operating point moving toward lower flow, thereby expanding the operational envelope of the compressor. Frequency analysis of the transient test data presented an early warning sign of surge onset, as a significant increase in system magnitude was observed when approaching the surge point.

Sammendrag

Oppgaven undersøker bruken av Digital Twin (DT)-teknologi for å forbedre effektiviteten til sentrifugalkompressorer, som er viktige komponenter i energiproduksjon og prossessindustrier. Ved å bruke Kompressorlabben ved Norges Teknisk-Naturvitenskapelige Universitet (NTNU), gir oppgaven valideringsdata for en fremtidig DT-modell og innsikt i kompressoroperasjoner.

Hovedmålet med oppgaven var å etablere et nøyaktig kompressorkart under termisk stabile forhold for en presis DT-modell, og å simulere ulike degraderingsscenarioer ved å variere vinklene på Inlet Guide Vanes (IGV). Å nøyaktig kunne forutsi Time to Surge (TTS) og Time in Surge (TIS) var av sentral interesse, da dette er viktige indikatorer på potensiell skade forårsaket av surge.

Et detaljert kompressorkart ble utviklet ved hjelp av statiske tester under termisk stabile forhold, dette ble gjort for å kunne danne en forbindelse mellom det fysiske systemet og dets digitale motpart. Deretter ble det gjennomført transiente tester for å studere TTS, Head Rise to Surge (HRTS) og TIS under forskjellige driftsscenarioer. Flere metoder ble implementert for å nøyaktig bestemme når surge er i ferd med å intreffe.

De transiente testene viste et forhold mellom HRTS og TTS. Det ble observert at høyere HRTS resulterer i en lengre TTS, noe som gir en bredere sikkerhetsmargin før surge begynner. I tillegg kan en høyere HRTS motvirke at driftspunktet har beveget seg mot lavere flow, og dermed utvide kompressorens operasjonelle område. Frekvensanalysen av de transiente testdataene viste et tidlig varselsignal om begynnelsen av surge, da en betydelig økning i størrelsen på oscilleringer ble observert når systemet nærmet seg surge.

Table of Contents

List of Figures

List of Tables

Nomenclature

Symbol	Unit	Elaboration
β	-	Diameter ratio
C	-	Discharge coefficient
D	[m]	Outer diameter
d	[m]	Inner diameter
f	-	Correction factor or Frequency
H	[J/kg]	Head
h	[J/kg]	Specific enthalpy
κ	-	Isentropic exponent
m	[kg]	Mass
$\dot{m}$	[kg/s]	Massflow
MW	[kg/Kmol]	Molecular weight
n	-	Polytropic exponent
P	[kW]	Power
p	$[N/m^2, Pa]$	Pressure
Q	$[m^3/\mathrm{s}]$	Volumetric flow
ρ	$[kg/m^3]$	Density
R	[J/kg K]	Specific Gas Constant
s	[J/kg K]	Specific entropy
T	[K]	Kelvin
τ	[Nm]	Torque
U	[m/s]	Tangential velocity
v	[m/s]	Velocity
W	[J]	Work
ω	[rad/s]	Rotational speed
Z	-	Compressibility factor
ϵ	-	Expansion factor
η	-	Efficiency
μ	[kg/ m s]	Dynamic viscosity
ν	$[m^2/s]$	Kinematic viscosity

Subscripts	Unit	Elaboration
1		Inlet
2		Outlet
A		Condition A/Operation point A
B		Condition B/Operation point B
p		polytropic
s		isentropic
θ		Circumferential direction

Abbrevation	Unit	Elaboration
ASCV		Antisurge Control Valve
BEP		Best Efficiency Point
BPF		Blade Passing Frequency
CL		Choke Line
DFT		Discrete Fourier Transform
DP		Differential pressure
DCV		Discharge valve
EOS		Equation of state
FFT		Fast Fourier Transform
HRTS		Head rise to surge
IGV		Inlet Guide Vanes
PMMA		Poly(methyl methacrylate)
RANS		Reynolds-Averaged Navier-Stokes
RMS		Root Mean Square
RPM		Rounds per minute
SL		Surge Line
SNR		Signal-to-Noise Ratio
TDMS		Technical Data Management Streaming
TIS		Time in Surge
TTS		Time to Surge
VIGV		Variable Inlet Guide Vanes
VSD		Variable Speed Drive

1 Introduction

The primary objective of this thesis is to build upon the earlier research at NTNU focused on the development of a digital twin for the centrifugal compressor in the NTNU wet gas compressor laboratory. The aim is accomplished by delivering additional experimental data, specifically concerning the headrise to surge and its consequential effect on the time to surge in the compressor. All the experimental data and findings presented in this thesis are derived from the single-stage centrifugal compressor at NTNU, functioning under air conditions close to atmospheric levels.

This chapter lays the foundation for the thesis by detailing the background and outlining the motivation behind this research. It also defines the scope of the work and presents an overview of the thesis structure.

1.1 Background

The evolution of energy availability over recent centuries has significantly shaped human progress. The discovery and utilization of diverse energy sources, from fossil fuels to nuclear, hydropower, and contemporary renewable technologies, has amplified production and consumption capacities [18]. This advancement faces hurdles because of pollution and greenhouse gas emissions. Innovative solutions are necessary, prompting a transition in the energy sector towards greener energy sources. Figure 1 shows the energy consumption increase from 1970 to 2021. Increasing the energy efficiency of already existing energy sectors is of great importance to achieve a reduction in greenhouse emissions while the energy needs are increasing.

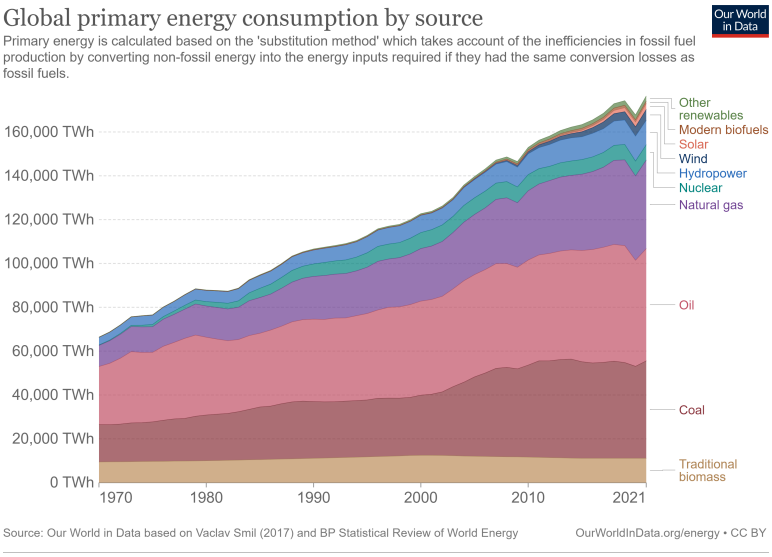

Figure 1: Global primary energy consumption by source.

A promising technology in increasing energy efficiency is the Digital Twin (DT) technology, which has emerged as a revolutionary tool for enhancing the sustainability of operations in diverse industries. DT technology facilitates the creation of virtual replicas

of physical systems, processes, or entities, thus offering multiple benefits such as design optimization, performance assessment, predictive maintenance, and process control [10]. One such critical system where digital twin technology proves particularly beneficial is in the realm of centrifugal compressors. Despite their significant construction and maintenance costs, Centrifugal compressors are essential in various sectors, including power generation, oil and gas, and chemical processing. In the context of the ongoing transition towards greener and more sustainable practices, these compressors significantly influence the efficiency and environmental impact of the industries they serve [24]. Digitizing compressor systems for remote and sub-sea operations offers a pathway to extend platform service life, as seen with Equinor's Åsgard field [9]. This practice, associated with lower costs, reduced risk, and environmental benefits compared to launching new fields, aids in diminishing the environmental footprint of the oil and gas sector.

One crucial aspect that requires in-depth understanding for enhancing energy efficiency is the entire operating region of compressors. A thorough comprehension of Time to Surge (TTS) under diverse operating conditions is vital to expand the operating range effectively. Consequently, this improves the compressor's efficiency and surge margin, paving the way for broader energy-saving measures [25][27].

Despite digital controls being in use since the 1980s, the evolution of digital models and simulations remains crucial for compressor operations. Institutions like NTNU persist in experimenting and advancing these digital tools. The latest step in this experimentation is utilizing the Gas Compressor Test Facility and DT technology to detect equipment conditions that affect the compressor system capacity and energy efficiency.

1.2 Scope of work

The compressor test lab at NTNU enables opportunities to develop, test and validate equipment deterioration. Of specific interest is utilizing new modeling techniques to detect equipment conditions that affect the compressor system capacity and energy efficiency. A comprehensive compressor map, accurately documented under thermally stable conditions, forms the essential foundation for a compressor DT model. This map is a critical connection between the physical system and its digital equivalent, contributing to accurate compressor simulations.

Sufficient validation data is crucial for the accurate operation of the DT under varying operating scenarios. Using varying Inlet Guide Vanes (IGV) angles one can simulate different compressor deterioration by varying the Headrise to Surge (HRTS) of the characteristic curve. Precise predictions of TTS across a range of deterioration scenarios can substantially impact the actual operating envelope of the compressor. Time in Surge (TIS) serves as a reliable predictor of potential surge-induced damage to the compressor.

With this in mind, the primary tasks of the thesis comprise:

- Develop a detailed compressor map of the NTNU compressor rig under thermally stable conditions.

- Establish representative compressor operating scenarios.
- Test and document "as new" and "deteriorated" equipment performance for the operating scenarios.

1.3 Thesis Structure

This thesis is structured as follows:

- **Chapter 1: Introduction -** This chapter provides an overview of the background and scope of work of the project.
- **Chapter 2: Theory -** This chapter presents the theoretical background related to the study.
- **Chapter 3: NTNU Testing Facility -** This chapter describes the NTNU testing facility setup. It also gives an overview of the scripts used to post-process the experimental results.
- **Chapter 4: Experimental Campaign -** This chapter details the experimental campaign undertaken for the study. It presents how each Case was carried out, and provides some definitions necessary for accurate interpretation of the results.
- **Chapter 5: Results and Discussion -** This chapter presents the results and discussion. Results from each Case are presented individually.
- **Chapter 6: Conclusion and Further Work -** This chapter concludes the thesis and suggests directions for further research.
- **Bibliography** Contains the bibliography.
- **Appendices** Includes all appendices for this thesis.

2 Theory

This chapter outlines the essential theory necessary to create a substrate for a future digital model of the NTNU Compressor rig. It introduces fundamental compressor theory, including the Schultz method, along with the procedure for calculating mass flow in a pipe utilizing an orifice plate. However, it does not cover every theoretical aspect related to turbomachinery. Other topics in this chapter include the general theory surrounding Fast Fourier Transform (FFT) analysis, compressor operation, compressor degradation, and the implementation of Variable Inlet Guide Vanes (VIGV).

2.1 The basics of compressors

Compressors are typically large mechanical equipment designed to increase the fluid pressure from the inlet, reducing the volume. The inlet fluid generally is gas. The gas is compressible, so the main objective of the compressor is to change the fluid's density or volume. Incompressible fluids like water are rarely used in compressors, as it is near impossible to change the volume or density of liquids, and it will also damage the compressor.

Compressors have a wide range of applications and are used in various industries. Different areas require different types of compressors. Compressors are divided into two main types; positive displacement and dynamic compressors. Positive displacement compressors draw in and capture a chamber's air volume. They then reduce the volume of the chamber to compress the air; reciprocating and screw compressors are examples of positive displacement compressors. Dynamic compressors increase the pressure by supplying kinetic energy to the inlet fluid; the kinetic energy is then converted to static pressure [28]. The primary focus of this thesis will be on dynamic compressors, which are divided into axial and centrifugal compressors. The main focus will be on centrifugal compressors.

The purpose of this chapter is to cover fundamental theory and to relate to the processing of experimental results in relation to the future DT of the NTNU compressor test lab.

2.2 Centrifugal compressor

The thesis will be based on results obtained at the NTNU wet gas compression testing facility, which has a centrifugal compressor at its heart. As such, this thesis's primary focus will be on centrifugal compressors. This section is a review based on Fluid Mechanics and Thermodynamics of Turbomachinery [16], courses [4, 5], the master thesis of Arnstad [1] and Ueland [28], and the project thesis of Simen Ormstad and Martin Hummervoll. Finally, the section documents the theoretical foundation for the use of the test rig.

Centrifugal compressors are dynamic turbomachinery used in various applications, including gas turbines, refrigeration, and air conditioning. The primary purpose of a centrifugal compressor is to increase fluid pressure by using centrifugal force. The primary parts of the centrifugal compressor is a rotating part called an impeller followed by a static dif-

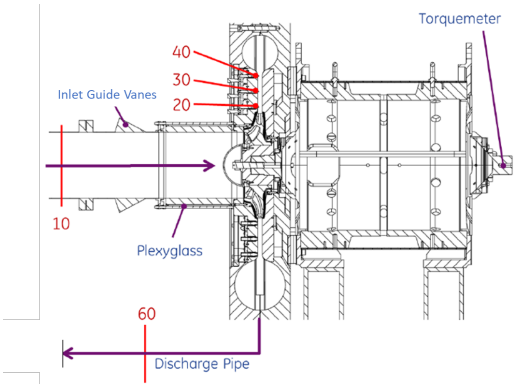

(a) Cross section of the compressor used in the NTNU testing facility

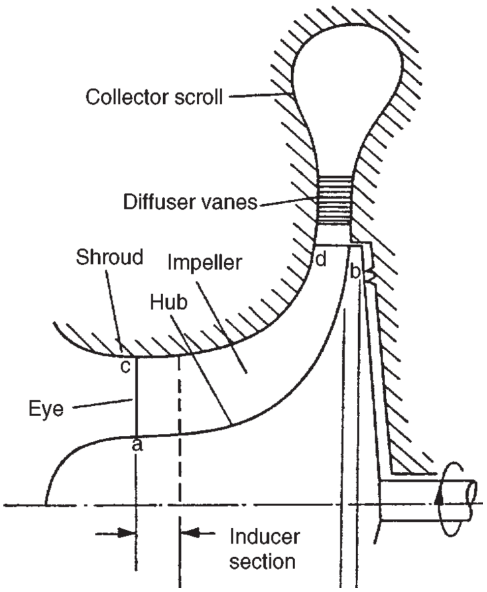

(b) Centrifugal compressor stage schematic. From Dixon [16]

Figure 2: Overview of centrifugal compressor stage.

fuser. The main task of the diffuser is to reduce the flow velocity and thereby increase the pressure. The flow streams into the compressor's inlet eye into the impeller section shown in figure 2, with the function of increasing the angular momentum of the fluid. IGVs are used to obtain the velocity triangle. In the impeller, static pressure and velocity are also increased [16]. The power P delivered by centrifugal compressors, or the rate at which work is done upon the fluid by the impeller running at angular velocity ω, is given in Equation 1:

$$P = \dot{W}_{compressor} = \tau\omega = \dot{m}(U_2 c_{\theta 2} - U_1 c_{\theta 1}) \tag{1}$$

Doing the specific work (work done on every unit mass of fluid):

$$\frac{P}{\dot{m}} = \frac{\dot{W}_{compressor}}{\dot{m}} = H = U_2 c_{\theta 2} - U_1 c_{\theta 1} > 0 \tag{2}$$

Equation 2 is also known as Euler's pump or compressor equation. Since $U = \omega r$, increasing the difference between the entry-radius r_1 and the exit-radius r_2 will increase the work done on the fluid by the compressor. This reveals a great advantage centrifugal compressors have over other types of compressors. While, for example, axial compressors can only increase the circumferential velocity c_θ, centrifugal compressors can increase both the circumferential velocity and the rotational radius to increase the work done by a single stage.

2.2.1 Performance analysis

A thorough understanding of performance is essential when testing, validating, designing, and operating a centrifugal compressor. For example, one can choose a polytropic or isentropic approach to understand the performance better.

Using the traditional isentropic approach, deviations can be significant when looking at actual gas behavior. Therefore, this thesis emphasizes polytropic analysis to facilitate the relationship of test results from one compressor to another or from one liquid medium to another.

2.2.2 Polytropic analysis

It is vital to obtain accurate compression calculations for the actual gas performance parameters. This applies to both the isentropic and polytropic approaches. A polytropic analysis is preferred for high pressure and various operating conditions.

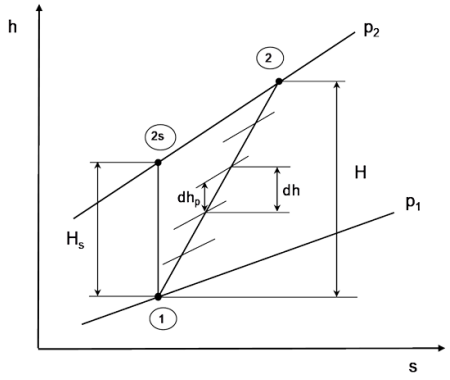

Figure 3: Compression process

Figure 3 states the combination of the isentropic and polytropic compression processes. H_s is defined as the isentropic head, $H_p = \sum dh_p$ polytropic head and $H = \sum$ dh is the actual head. Thermodynamic properties change, but it is clear that the polytropic process is more likely to be an actual compression process than the isentropic, even though it is mordantly less than the actual head. Isentropic compression consists of constant entropy and increasing enthalpy. Polytropic compression can be described as the sum of infinitesimal isentropic compression steps along the compression path determined by the compressor efficiency.

$$T = \left(\frac{\partial h}{\partial s}\right)_p \tag{3}$$

The two inlet and outlet isobars diverge with increasing temperatures, as seen in Figure 3. Figure 3 illustrates these isobaric lines; the isobaric outlet line has a higher and steeper gradient than the inlet one. Due to this description of figure 3, polytropic head and efficiency are always higher than for the isentropic process.

At constant efficiency, the generalized polytropic process is defined by the following equation:

$$p\, v^n = const \tag{4}$$

To obtain accurate performance calculations for real gas behavior, it is essential to use the polytropic volume exponent, n_v. This is based on Schultz's polytropic approach which is used by international standards such as ISO 5389 and ASME PTC10; Schultz provides detailed descriptions [21]. At given suction and discharge conditions, the polytropic volume exponent is given by the following equation;

$$n_v = \frac{ln(\frac{p_2}{p_1})}{ln(\frac{v_1}{v_2})} \tag{5}$$

InEquation5, subscript 1 refers to inlet pressure and specific volume, and subscript 2 refers to outlet pressure and volume. By using this, it is possible to calculate the polytropic exponent.

During the compressor process cycle, the polytropic exponent varies. Therefore it is impossible to get an exact solution of the polytropic head. This leads to assuming that the polytropic exponent is constant for solving the polytropic head in the equation below:

$$H_p = \int_1^2 v dp \approx \frac{n_v}{n_v - 1} \left[p_2\, v_2 - p_1\, v_1\right] \tag{6}$$

Due to this assumption, there will be an approximate solution of the integral. The polytropic head is multiplied with the correction factor f to make the approximation more reliable. The correction factor will consider the polytropic exponent n_v variations along the compression cycle.

$$f = f_s = \frac{h_{2_s} - h_1}{\frac{k_v}{k_v - 1}[p_2 v_{2s} - p_1 v_1]} \tag{7}$$

In Equation 7, h refers to specific enthalpy, and subscript 2s refers to the constant isentropic value at level 2.

Introducing the expression for the compressibility factor Z;

$$Z = \frac{p}{\rho\, R_{spec}\, T} \tag{8}$$

By use of this equation and Equation 7, it is possible to calculate the polytropic head from this equation;

$$H_p \approx f\, \frac{n_v}{n_v - 1}\, \frac{Z_1\, R_0\, T_1}{MW}\, \left[\left(\frac{p_2}{p_1}\right)^{\frac{n_v - 1}{n_v}} - 1\right] \tag{9}$$

The polytropic head factor normally accounts for a 0.1-0.5% change in H_p [4]. It is also possible to determine the polytropic efficiency and power from these equations, respectively:

$$\eta_p = \frac{v\, dp}{dh} = \frac{H_p}{H} \tag{10}$$

$$P_{fluid} = \frac{\dot{m} H_p}{\eta_P} \tag{11}$$

In the end, this review demonstrates useful equations to determine head and efficiency built upon thermodynamic conditions for real gases. Inlet and outlet conditions can be determined in the NTNU testing facility lab or using the future DT model. These methods are heavily leveraged to obtain the results shown in section 5.

Affinity laws

Following is a review of the affinity laws. These relationships are used in section 5 to determine compressor curves.

The affinity laws demonstrate the relationship between the head (H), volumetric flow rate (Q), rotational speed (ω), and power (P). The affinity laws are often referred to as fan laws, these equations can be used to extrapolate a point at one rotational velocity to a corresponding point at a different rotational velocity. It can be used to extrapolate characteristic curves, expanding from one characteristic curve to a fuller compressor map. A prerequisite for these equations is the assumption that the polytropic efficiency remains constant.

$$\frac{Q_A}{Q_B} = \frac{\omega_A}{\omega_B} \tag{12}$$

$$\frac{H_A}{H_B} = \left(\frac{\omega_A}{\omega_B}\right)^2 \tag{13}$$

$$\frac{P_A}{P_B} = \left(\frac{\omega_A}{\omega_B}\right)^3 \tag{14}$$

2.2.3 Compressor operation

A compressor is only one element within a comprehensive system that includes elements such as valves, separators, and connecting tubes, among others. There's typically many additional components, each one interacting with the others in some way. For example, the functioning of the compressor is tied to the conditions both upstream and downstream of it. This interaction is visualized in Figure 4, where the compressor's performance curve

intersects with the system resistance curve, thus establishing the compressor's operating point. Even small changes in these conditions can shift the system resistance curve. Assuming that the compressor's speed remains constant, this would result in the operating point moving along the operation line.

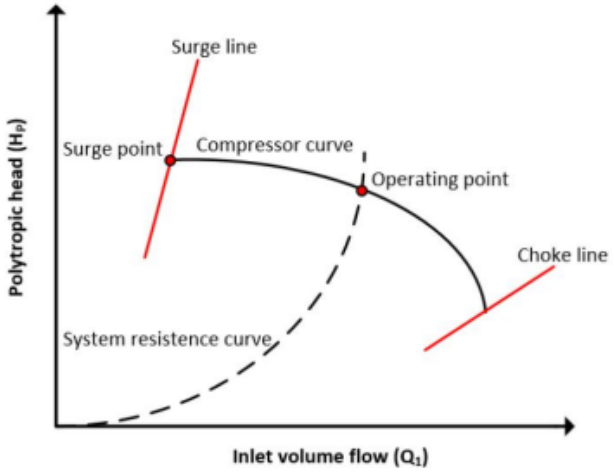

Figure 4: A generic compressor curve, highlighting the SL, CL operating point, and the system resistance curve. From Rande [17]

Surge, TTS and HRTS

TTS is an essential parameter in the analysis of centrifugal compressors, as it denotes the period between the initiation of a transient event and the onset of surge. Surge is an unfavorable phenomenon characterized by an abrupt decline in the compressor's flow rate accompanied by a corresponding increase in pressure, which may lead to vibrations, fatigue, and potential damage to the compressor [3]. Investigating the factors influencing TTS is vital for optimizing compressor design and operation to avert surge and ensure dependable performance. As shown in [27], a time delay in the trip signal from 150 to 300 ms makes the hot gas bypass system unable to protect the compressor from entering surge. On the same note, a delay in TTS could be enough for the hot gas bypass system to protect the compressor from entering surge.

The gradient of the compressor characteristic curve, representing the relationship between the pressure ratio and the flow rate, significantly affects the TTS. A steeper characteristic curve implies a more extended TTS, as the compressor demonstrates an enhanced ability to tolerate variations in operating conditions without entering surge [3]. In contrast, a flatter characteristic curve indicates a more sensitive compressor operation, resulting in a shorter TTS.

Another crucial factor influencing TTS is the HRTS, which is the difference between the head developed by the compressor at its peak efficiency point and the head at the surge limit. A higher HRTS generally corresponds to a longer TTS. Conversely, a lower HRTS can result in a shorter TTS [3].

Choke

Choke in centrifugal compressors, refers to an operation where the compressor runs at very high flow rates beyond its best efficiency point (BEP). This is typically discouraged because it dramatically reduces the compressor's efficiency and subjects its components, like impeller vanes, to destructive aerodynamic forces. Choke occurs when flow passages in the compressor become blocked due to compression shocks or massive flow separation. To avoid choke, manufacturers install additional throttle valves or select intricate recycle and anti-surge valve mechanisms, increasing operational costs and limiting the compressor's operating range. Therefore, understanding and managing choke is a critical aspect of compressor operation in the industry [13].

Rotating stall

Rotating stall disrupts a compressor's fluid flow, often leading to uneven air flow and violent vibrations. It can cause significant internal damage, reducing the compressor's operational flexibility and efficiency. It typically occurs during power outages or specific transient scenarios and is closely associated with surge events. Managing a compressor's transient response is crucial in preventing rotating stall events from ensuring compressor stability and longevity[26].

2.2.4 Compressor degradation

In an ideal scenario, a compressor would consistently operate at its design point, allowing it to keep the optimal efficiency level. However, fatigue and damage to the sealing system can cause the compressor to deteriorate over time. This deterioration can manifest in various forms, such as fouling, inter-leakage, and erosion. Therefore, it is crucial to identify these issues and document their effects to maintain the compressor's proper functioning.

This part will create the substrate to create representative cases for simulation and validation of a digital twin of the model for later use.

Fouling

Fouling is a typical deterioration problem in a compressor. Fouling is a slow-growing process, a non-uniform and non-linear mechanism in the machine that happens over time. A compressor typically contains a solid filtration system. However, due to heavy mass flow and industrial location, these machines will experience contaminants such as soot, dirt, salt, and other particles that will cause problems for the compressor. Fouling mechanisms involve three specific aspects: the environmental conditions such as airborne contaminants, salt and other elements present in the air where the gas turbine operates; the power plant's design and management, including factors like filtration system and washing operation; and compressor characteristics like pressure ratio and the number of stages [23].

The result would be a reduction of the flow area and an increase in surface roughness, which further causes an increase in frictional losses—due to the reduction of the flow area; fouling mainly influences the characteristics of the compressor during high volumetric flow. Ultimately, this will result in a lack of overall performance parameters such as polytropic head and efficiency, as documented in Bakken's article [27].

Gradually flatter characteristics of the compressor have a very harmful effect on stability when driver trips occur; the machine enters the surge area more easily. During surge, it usually causes high vibrations and mechanical stress, which causes further degradation.

Figure 5 shows compressor run-down characteristics at fouled impeller and diffuser performance. Here new characteristics refer to the original characteristic before any deterioration.

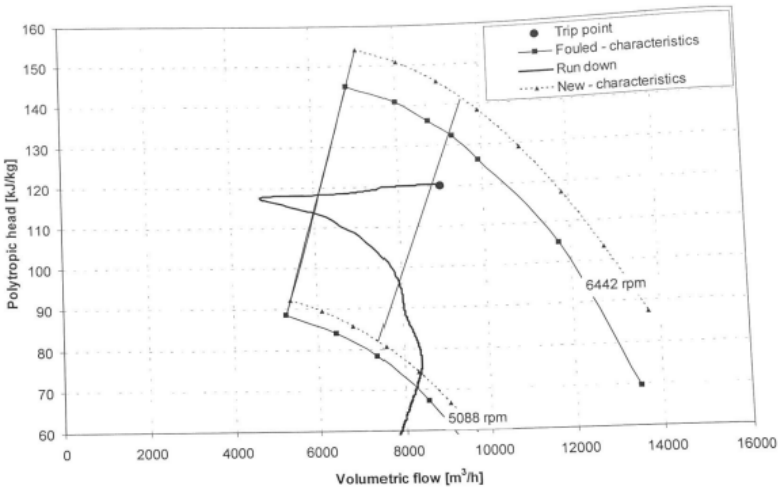

Figure 5: Compressor run-down characteristics at impeller and diffuser fouling. From [27].

Interleakage in labyrinths

Another phenomenon that causes deterioration to the compressor system is internal leakage in the sealing system. Internal leakage can relate to the deterioration of the impeller, balancing piston, and shaft labyrinths running in the compressor system. Also, when the machine operates in surge area, this will result in overweening wear of the internal labyrinths in the system. This phenomenon mainly influences the ability to maintain the pressure increase against a high-pressure ratio before the surge area. However, it also influences the shape of performance characteristics [27]. Typically, the HRTS is reduced, and the Surge Line (SL) is shifted towards reduced inlet volume flow. Even though the surge margin is increased, the shift in performance makes the compressor less stable concerning surge [26].

Figure 6 shows compressor run-down characteristics at increased internal leakage. Here new characteristics refer to the original characteristic before any deterioration.

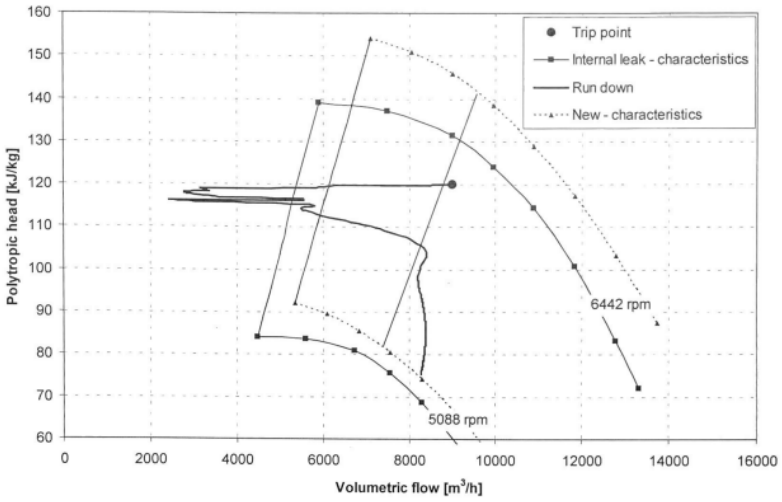

Figure 6: Figure showing compressor run-down characteristics at increased internal leakages. From [27].

Erosion

The effects of erosion on turbomachinery can be challenging to detect, as the degree of deterioration can vary greatly depending on the specific conditions and factors involved. Erosion can result in an increase in roughness on the blades, particularly on the leading edge, which can affect the inlet profile of the blade. This can cause the angle of incidence to deviate from the optimal design for the impeller, leading to reduced performance and efficiency. Therefore, to mitigate the effects of erosion, it is essential to implement appropriate measures, such as protective coatings or frequent inspections, to ensure the longevity and performance of the turbomachinery [27].

2.3 Variable inlet guide vanes

The stationary blades, known as IGV, are mounted on the compressor casing upstream of the impeller. These guide vanes play a crucial role in controlling the impeller's inlet angle, thereby impacting the compressor's characteristics and stability. By adjusting the angle of the IGV, the compressor can be optimized to operate at its BEP, even under off-design conditions. Adding IGV to a system can improve the flow guiding and distribution at the impeller eye, mitigating inefficiencies. Many industrial compressors, subject to varying operational conditions, are equipped with VIGV to enhance their performance in off-design scenarios. Guide vanes are also commonly found in various gas turbine and turbocharger applications. Figure 7 depicts a VIGV assembly for a fan, where the vanes are controlled by a rotating actuator ring on the outer casing.

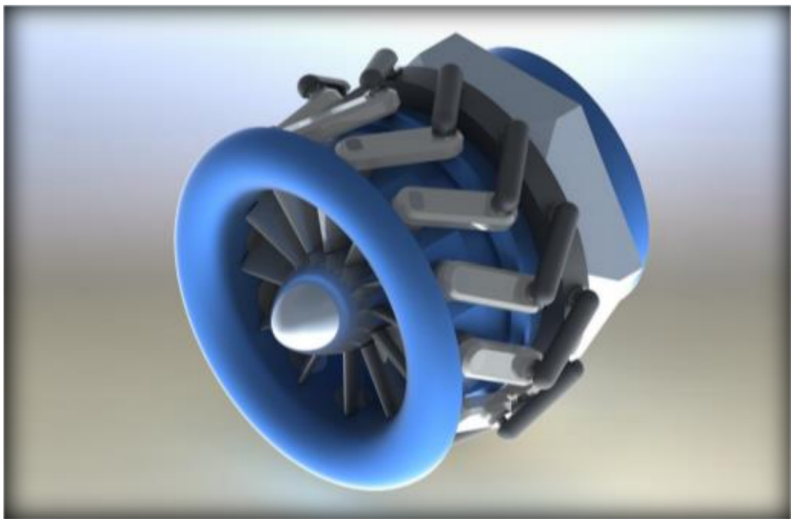

Figure 7: IGV assembly for a small turbine engine. Extracted from [20]

This section aims to present the principle of operation and dry gas performance. The VIGV will only be discussed in connection to centrifugal compressors. This section will be based on theory from [16].

The inlet guide vane

Figure 8 shows the nomenclature used on compressor cascade and blades; this notation will be used going forward in the thesis.

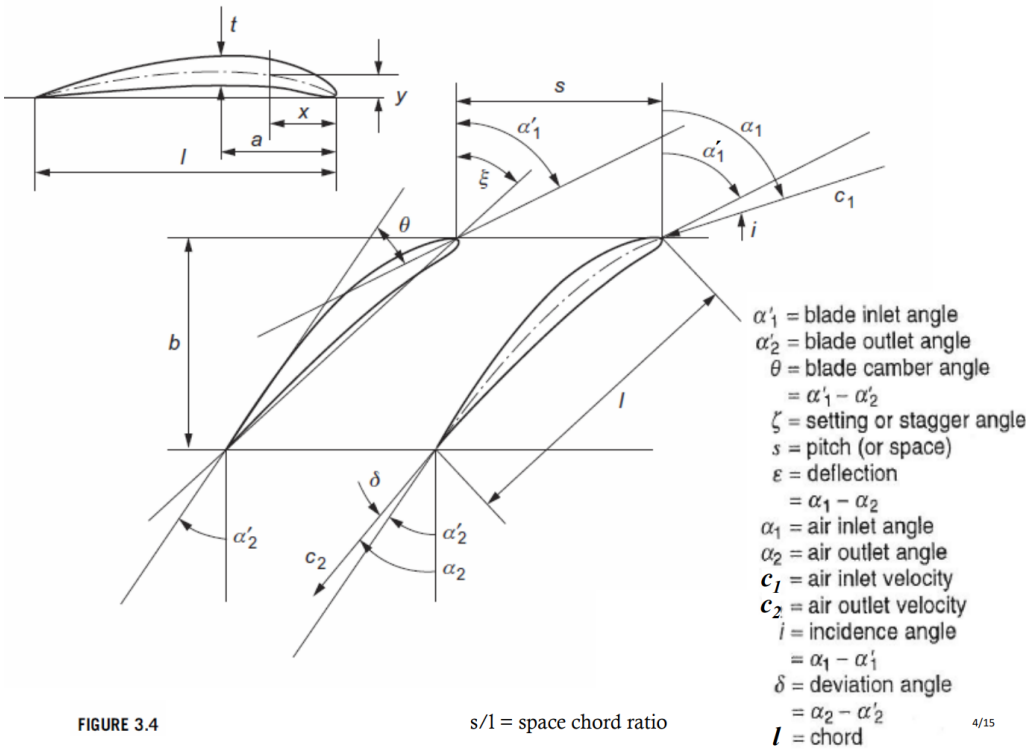

Figure 8: Compressor cascade and blade notation. From [16]

Pre Whirl

Euler's turbine equation is fundamental for understanding the energy transfer in turbomachinery, such as centrifugal compressors. It relates the change in enthalpy of the fluid to the blade velocity and change in tangential fluid velocity, as described in Equation 2. This equation is of great significance in IGV operation.

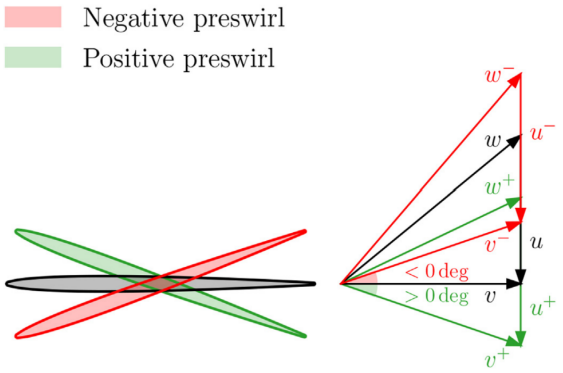

Figure 9: Effect of prewhirl on velocity triangles at the impeller inlet. From [19]

Prewhirl is a phenomenon observed in turbomachines, referring to the induced swirl in the fluid flow upstream of the impeller due to the rotation of the IGVs. This rotation gives the flow a tangential velocity component before it enters the impeller, impacting the performance parameters of the machine.

The prewhirl can be either positive or negative depending on the direction of the IGVs rotation relative to the impeller. A negative prewhirl is achieved when the IGVs rotate in the opposite direction to the impeller. This increases the impeller incidence angle at high flow rates, resulting in a higher relative Mach number and Eulerian work than in a fully open condition. On the other hand, a positive prewhirl, characterized by IGVs rotating in the same direction as the impeller, reduces these parameters. This opposite effect illustrates how the direction of the IGV rotation significantly impacts the performance characteristics of a turbomachine [19].

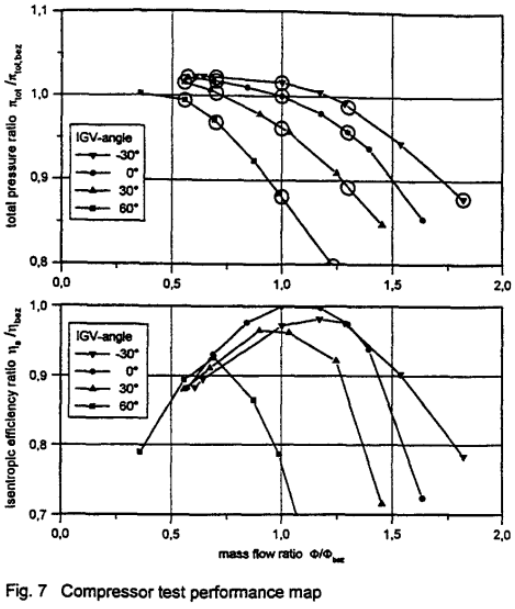

Fig. 7 Compressor test performance map

(a) Effect of prewhirl on isentropic pressure ratio and efficiency ratio. From [12]

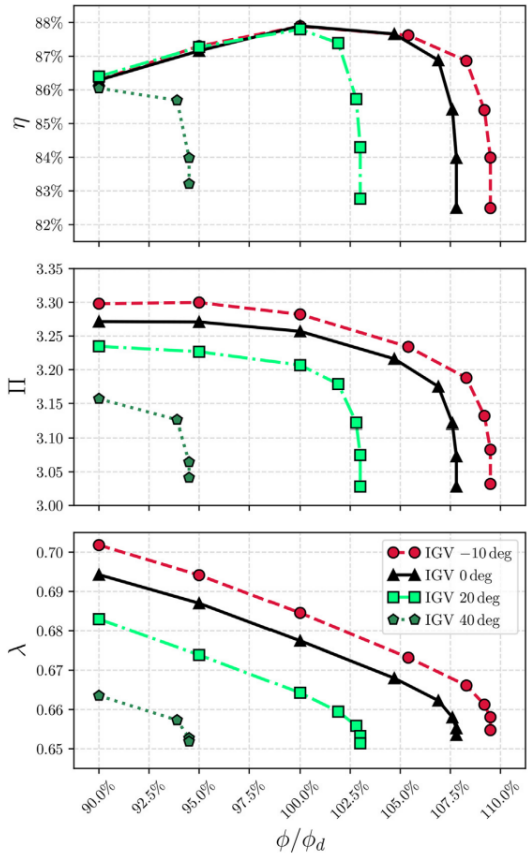

(b) Effect of prewhirl on compressor performance. η is defined as total-total efficiency, Π is defined as the total-total pressure ratio, and λ as the wor coefficienct. From [19]

Figure 10: Effect of prewhirl on compressor characteristics.

Figure 10 presents the impact of variations in the IGV angle on the performance of a centrifugal compressor, as explored through Reynolds-Averaged Navier-Stokes (RANS) simulations [19].

As Figure 10a shows, the relative mass flow rate is plotted against IGV angles ranging from -30°to 60°on the x-axis. Two critical performance indicators, the isentropic pressure, and isentropic efficiency ratios, are depicted on the upper and lower graphs, respectively.

A noticeable trend emerges in the context of the total pressure ratio. A negative IGV angle correlates with an augmented pressure ratio and maximum relative mass flow rate, presenting a flatter characteristic curve. Conversely, an escalation in the IGV angle tends to produce the inverse effect. This trend is further confirmed by the middle plot in Figure 10b, which illustrates a consistent decline in the total-total pressure ratio as the prewhirl intensifies.

2.4 Mass-flow Measurement

Directly measuring mass flow using sensors is not feasible; it is calculated indirectly. One such method involves utilizing the difference in static pressure over the flow element, as described in NS-EN ISO 5167-2:2022 [22].

This section describes the process of mass flow calculation using an orifice plate, the flow element used for measurements in the test rig. Figure 11 shows a standard orifice plate.

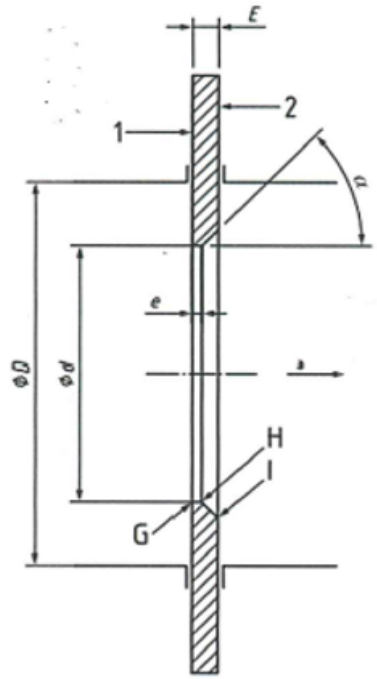

Key
1 upstream face A
2 downstream face B
a Direction of flow.

Figure 11: Standard orifice plate defined in ISO 5167-2 [22].

Orifice Meter

An orifice, utilized for flow measurement and pressure control, is a crucial component of the NTNU rig. The orifice plate at the rig is equipped with corner taps, as such the pressure is measured at the base of the flange.

The accurate calculation of the orifice meter is paramount for the compressor operation. Determining whether the compressor operates at the BEP and operates near the choke or surge area is integral. Consequently, various tools have been deployed for verification and included in the calculations.

The NS-EN ISO 5167-2:2022 standard [22] provides the following equation to determine the mass flow over an orifice:

$$\dot{m} = \frac{C}{1-\beta^4}\,\epsilon\,\frac{\pi}{4}\,d^2\,\sqrt{2\,\Delta p\,\rho_1} \tag{15}$$

In Equation 15, the parameters represent the discharge coefficient (C), the expansion factor (ϵ), β ($\beta = \frac{d}{D}$, where d is the smaller diameter, and D is the larger pipe diameter), $\Delta p = p_1 - p_2$ (the differential pressure across the plate), and ρ_1 (the upstream density).

The expansion factor, ϵ, is calculated as follows:

$$\epsilon = 1 - (0.351 + 0.256\beta^4 + 0.93\beta^8)\,\left[1 - \left(\frac{p_2}{p_1}\right)^{\left(\frac{1}{\kappa}\right)}\right] \tag{16}$$

The discharge coefficient, C, is derived from the equation:

$$\begin{aligned} C = {} & 0.5961 + 0.0261\beta^2 - 0.216\beta^8 + 0.000521\left(\frac{10^6\beta}{Re_D}\right)^{0.7} \\ & + (0.0188 + 0.0063A)\beta^{3.5}\left(\frac{10^6}{Re_D}\right)^{0.3} \\ & + (0.043 + 0.0080e^{-10\,L_1} - 0.123e^{-7\,L_1})(1 - 0.11A)\,\frac{\beta^4}{1-\beta^4} \\ & - 0.031(M_2^{'} - 0.8M_2^{'1.1})\beta^{1.3} \end{aligned} \tag{17}$$

In Equation 17, L_1 represents the distance to the upstream tap, and M_2' signifies the distance to the downstream tap. Further, Re_D is the Reynolds number calculated using the pipe diameter D, pipe flow velocity v, and the kinematic viscosity μ. The iterative calculation of Re_D is presented in section 5.

$$Re_D = \frac{D\,v}{\nu} = \frac{D\,v\rho}{\mu} \tag{18}$$

The factor A is derived from Equation 19.

$$A = \left(\frac{19000\beta}{Re_D}\right)^{0.8} \tag{19}$$

As the orifice plate in the NTNU testing facility features corner taps, $L_1 = M_2^{'} = 0$, which simplifies Equation 17 to the form below:

$$\begin{aligned} C = {} & 0.5961 + 0.0261\beta^2 - 0.216\beta^8 + 0.000521\left(\frac{10^6\beta}{R_{e_D}}\right)^{0.7} \\ & + (0.0188 + 0.0063A)\beta^{3.5}\left(\frac{10^6}{Re_D}\right)^{0.3} \end{aligned} \tag{20}$$

Thermal equilibrium

Thermal equilibrium is an essential concept in the operation and performance of compressor systems. It signifies a state where heat exchange between system components remains constant over time. This section will shed light on the impact of changing operating conditions on the system's thermal equilibrium.

A compressor system establishes thermal equilibrium under steady-state conditions, with constant heat generation and dissipation rates. However, adjustments in the system's operating conditions can disrupt this balance. Such modifications may include changes in the heat generated or dissipated, thus shifting the system away from its thermal equilibrium.

Regaining thermal equilibrium after such transitions involves maintaining the new operating conditions for a sufficient duration. The system naturally progresses towards a new state of equilibrium where heat exchange rates are again balanced. The time required to attain this state depends upon the magnitude of the changes in operating conditions. Minor adjustments might result in a quick return to equilibrium, while drastic modifications could necessitate an extended stabilization period.

2.5 Fast Fourier Transform Analysis

The FFT is a widely used algorithm for efficiently computing a finite sequence's Discrete Fourier Transform (DFT). In the context of a centrifugal compressor, FFT analysis can be used to analyze the frequency content of pressure and vibration signals to identify potential faults and performance issues and to conduct condition monitoring. The concepts discussed in this section are based on the work of Oppenheim and Schafer[15].

Discrete Fourier Transform

The DFT is a mathematical operation that takes a discrete-time signal, $x[n]$, and transforms it into a frequency domain representation, $X[k]$, a series of complex numbers representing the amplitudes and phases of the signal's frequency components.

The following equation gives the DFT:

$$X[k] = \sum_{n=0}^{N-1} x[n] e^{-j2\pi kn/N} \tag{21}$$

where $x[n]$ is the input signal, $X[k]$ is the output frequency spectrum, N is the number of points in the signal, j is the imaginary unit and k and n are the frequency and time indices, respectively.

Fast Fourier Transform

The FFT is an efficient algorithm for computing the DFT that takes advantage of the symmetries in the transform kernel, reducing the number of operations required from $O(N^2)$ for the direct DFT computation to $O(N \log_2 N)$ for the FFT. The most common FFT algorithm is the Cooley-Tukey algorithm, which recursively divides the input sequence into even and odd samples, reducing the computational complexity.

Application to Centrifugal Compressors

A centrifugal compressor accelerates fluid by a rotating impeller, increasing its kinetic energy and pressure. The compressor's performance can be affected by various factors, such as flow instabilities, rotating stall, and mechanical vibrations. As described by Oppenheim and Schafer [15], FFT analysis can be applied to the pressure and vibration signals to identify these issues and monitor the compressor's health.

Typically, the frequency components of interest are the blade passing frequency (BPF) and its harmonics. The BPF is given by:

$$f_{BPF} = \frac{N_{\text{blades}} \cdot \omega}{60} \tag{22}$$

Where f_{BPF} is the blade passing frequency, N_{blades} is the number of impeller blades, and ω is the rotational speed of the compressor in revolutions per minute. The presence of significant amplitude peaks at the BPF or its harmonics in the FFT spectrum may indicate potential issues with the compressor operation.

2.5.1 Window Functions and Overlap

Window functions and overlap in FFT analysis are crucial considerations in signal processing. They influence the resulting spectral estimate's resolution, leakage, and detectability of transient events. This section provides an overview of the Rectangular and Hanning windows and discusses the role of overlap. Figure 12 shows an overview of commonly used windows; Hann here replaces Hanning.

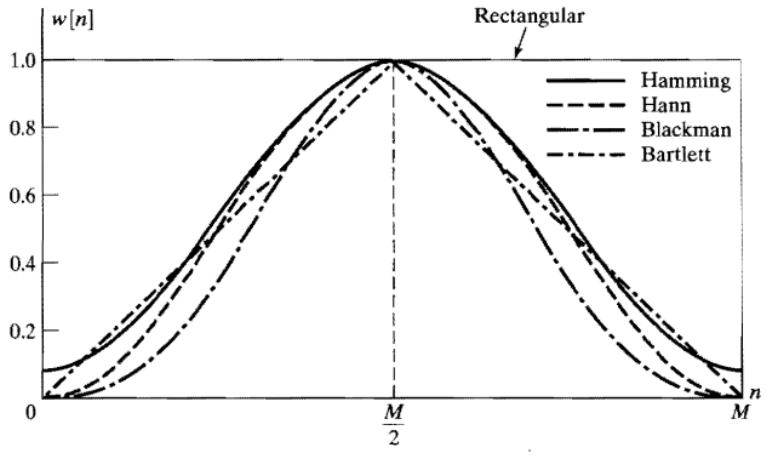

Figure 12: Overview of commonly used windows, Hann is here the Hanning window. Extracted from [15]

Rectangular Window

The simplest of all window functions is the Rectangular window. It equates to not applying any windowing at all. For a finite-length signal $x(n)$, where n denotes the discrete time index and the signal's length is N, the Rectangular window function, $w(n)$, is given by:

$$w(n) = \begin{cases} 1, & \text{for } 0 \leq n \leq N-1 \\ 0, & \text{otherwise} \end{cases} \tag{23}$$

Despite inducing substantial spectral leakage, the Rectangular window offers excellent frequency resolution due to the narrow width of its main lobe [15].

Hanning Window

The Hanning window is widely utilized because it balances spectral leakage against frequency resolution. It is mathematically defined as:

$$w(n) = 0.5\left(1 - \cos\left(\frac{2\pi n}{N-1}\right)\right), \text{ for } 0 \leq n \leq N-1 \tag{24}$$

Compared to the Rectangular window, the Hanning window mitigates spectral leakage at the expense of slightly reduced frequency resolution [15].

Overlap Percentage

The overlap percentage is a critical factor in FFT-based analyses that influences the Signal-to-Noise Ratio (SNR) and the ability to detect transient signal components. Overlapping

windows ensure minimal loss of information due to the windowing process. This is especially relevant for the Hanning window due to its inherent tapering. For example, a 50% overlap signifies that consecutive windows shift by half the window length, yielding a more evenly distributed signal energy in the frequency domain [15].

3 NTNU Testing Facility

This chapter presents a comprehensive overview of the compressor laboratory at the NTNU. It provides a detailed discussion of the post-processing techniques of the experimental data acquired from the experimental campaigns, as described in Chapter 4. Two Python scripts specifically designed for data processing are described. The Python scripts along with experimental data from all the campaigns were delivered to the supervisor of this thesis, Lars Eirik Bakken. Further elaboration is provided on the Equation of State (EOS) and the modules utilized in the Aspen HYSYS process simulation software, which play pivotal roles in the aforementioned Python scripts. The implementation of FFT calculations is also discussed, which is accomplished via the MATLAB-compiled package known as the VibrationData Toolbox. This toolbox is a resource in signal analysis and structural dynamics.

3.1 Test facility setup

The NTNU testing facility houses a full-scale, single-stage centrifugal compressor. The compressor operates under atmospheric conditions and, in this particular case, utilizes air intake as the operating fluid. The setup of the testing facility is ideally designed for experimental analysis, featuring a more comprehensive array of sensors and measuring devices than a typical industrial configuration. This enhancement facilitates an in-depth understanding, higher accuracy, and the potential for subsequent research based on the results obtained.

The compressor employed in this study is furnished with VIGVs utilized throughout the testing phase. In addition, the VIGVs were leveraged extensively during the tests to highlight the impact of variable steepness of characteristic curves across several scenarios.

Figure 13 illustrates the layout of the testing facility used across all experimental campaigns in this thesis. The schematic predominantly centers on the compressor and its associated components, underscoring the primary focus of the experiments.

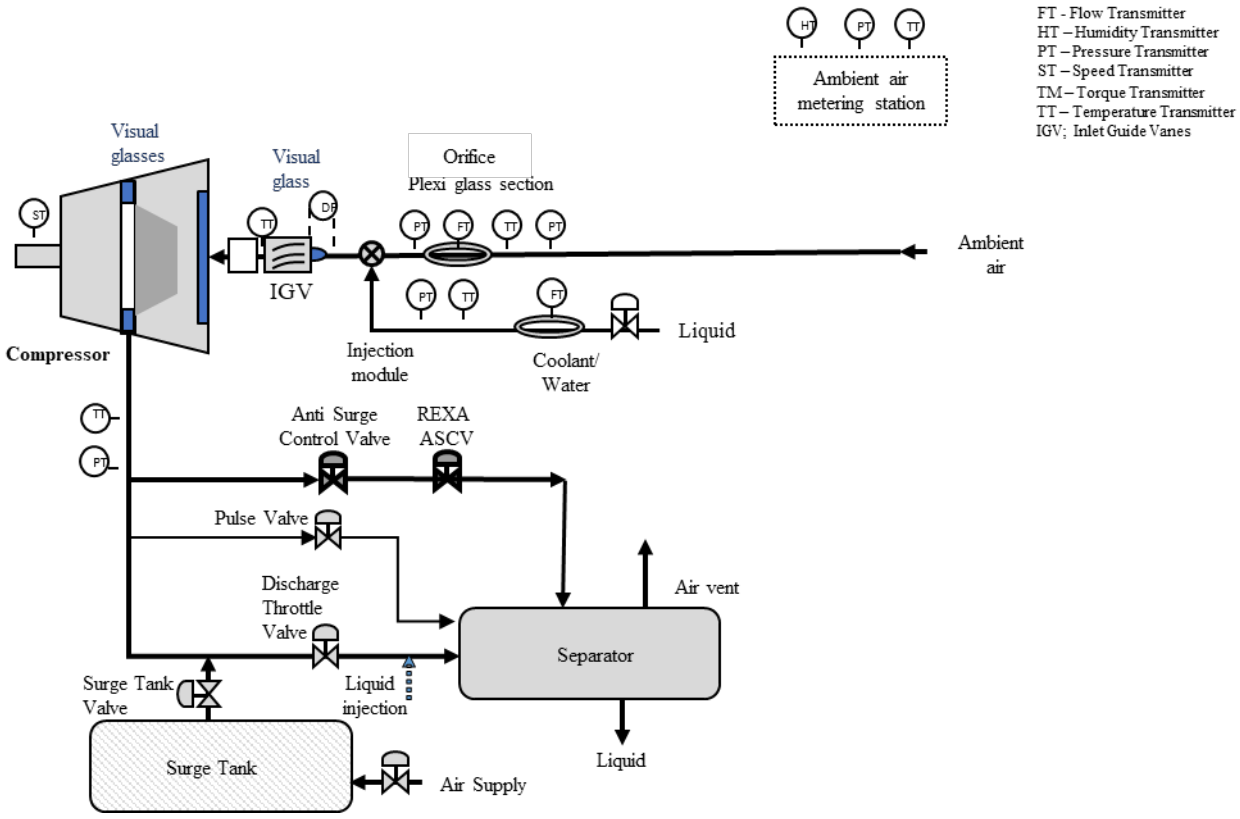

Figure 13: Full layout of NTNU testing facility

The Anti Surge Control Valve (ASCV), as shown in figure 13, is situated downstream of the compressor block. The ASCV is the valve used for all experiments in this thesis to manipulate flow magnitude. The valve features an electric actuator, controllable from the panel, and allows automatic adjustment. This blend of automatic and remote ASCV adjustability facilitates an optimal testing environment. In addition, the ASCV can be manipulated directly from the control panel in real-time operation. It can also be pre-configured before initiating tests, enabling the simulation of desired conditions in advance.

The REXA valve was repositioned several times during the testing phase. It was situated behind the ASCV for the initial testing stage. In subsequent testing periods, it was relocated and sat behind the Discharge Valve (DCV). Despite the REXA valve remaining open throughout the testing process, it may have introduced some extra flow restrictions when positioned downstream of the valve used for flow control.

Sets of four sensors, each consisting of pressure and temperature sensors, are strategically positioned at the inlet and outlet of the compressor. The sensors are shown in 3, TT denotes the temperature sensors, and PT denotes the pressure sensors. These sensors will be extensively leveraged in the post-processing stage of the experimental campaign. The calibration process for the pressure sensors is described in section 4.1. Meanwhile, specific temperature sensors are known to exhibit occasional spikes; the approach to managing this issue is outlined in section 3.3.2.

Table 1: DP sensors connected to the orifice.

Sensor "name"	**Range (mBar)**	**Type**
DP25	[-25, 25]	
DP50	[-50, 50]	Protran PR3202
DP250	[-250, 250]	
DP smar	[-50, 250]	PCE-28

The experiments conducted in this study involved an orifice equipped with four distinct Differential Pressure (DP) sensors. These DP sensors are tasked with measuring the DP across the orifice, a critical metric for calculating the volumetric flow within the system. Therefore, these sensors must demonstrate high accuracy and are not prone to significant deviations. The sensors vary in terms of range and response time. Notably, the DP250 sensor demonstrated a swifter response time than the DP smar and boasted a larger maximum range than the remaining Protran sensors. These traits effectively shielded it from premature saturation. Consequently, it was the consensus within the team to employ the DP250 sensor as the sole DP sensor at the orifice for the entirety of the experimental campaign. Positioned 1-2 meters ahead of the compressor block, the orifice has a diameter ratio (β) of 0.6957, a parameter employed in the calculations per Equation 17.

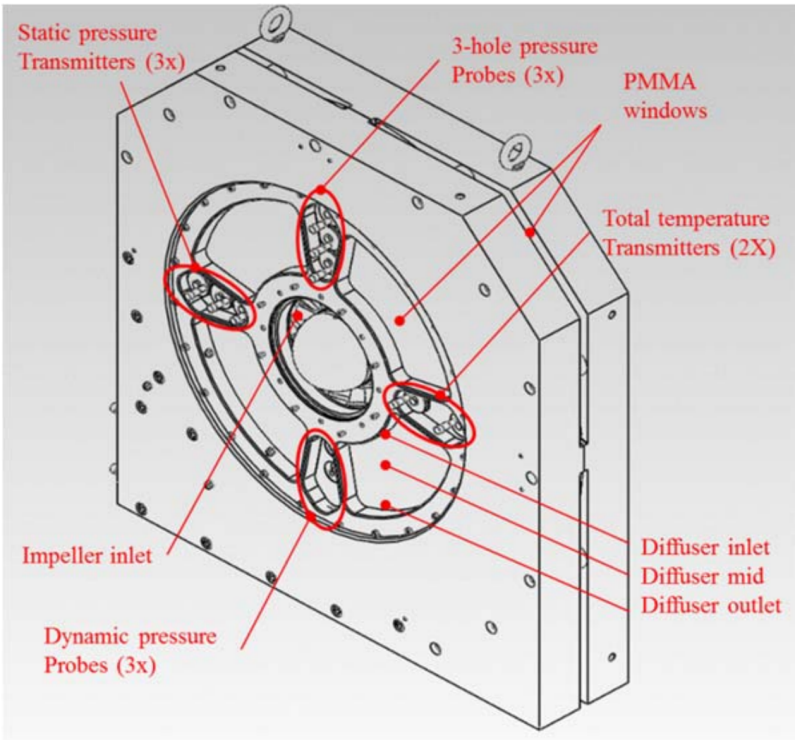

Figure 14: Compressor section with diffuser instrumentation. From [10]

The modular compression section can facilitate effortless transitions between impeller and diffuser designs. The impeller front was furnished with four sizeable PMMA windows, enabling a clear view of the impeller outlet, and diverse instrumentation was arranged radially. The diffuser could be visually inspected through the PMMA window located

in the section split. The comprehensive structure of the compressor section is depicted in Figure 14. It is worth drawing attention to the trio of dynamic pressure sensors, particularly the sensor situated in the topmost position, which has played an important role in this thesis. This upper sensor has been extensively employed during high-speed testing to compute the FFT of the pressure at the impeller outlet. The dynamic pressure sensors are furnished with PCB Piezotronics and have a resolution of 0.14 mBar [7]. The utilization and implications of this approach will be delved into in more detail in sections 3.3.4, 4, and 5.

Figure 15 shows an overview of a representative impeller 15a and the dynamic pressure sensor 15b used for the FFT analysis highlighted by a red circle. The impeller comprises 18 blades, half short and half long. The impact of the design of the impeller will be discussed later in the thesis in connection to the FFTs from the dynamic pressure sensor.

(a) Compressor impeller

(b) Dynamic pressure sensor at the impeller outlet.

Figure 15: Overview of the NTNU testing facility

The entire facility is focused around the compressor, displayed at the top-left of Figure 13. The dimensions of this compressor are provided in Table 2b. This compressor is coupled with an electric Variable Speed Drive (VSD) motor, the specifications of which can be viewed in Table 2a.

Table 2: Detailing the specifications of the electric motor and the compressor dimensions.

(a) Electric motor

Available power	450 kW
Maximum speed	11 000 RPM
Number of poles	3
Shaft coupling	Gearless
Control	Variable speed drive

(b) Compressor dimension

Inlet hub diameter	250 mm
Diffuser width	20 mm
Diffuser ratio	1.7
Impeller outlet diameter	400 mm
Outlet pipe diameter	200 mm

3.2 Variable inlet guide vanes assembly

The VIGV assembly comprised 14 contoured blades, maneuverable via an actuator. It was engineered to operate within an incidence angle of -25° to 42°. Positioned just before the impeller, the VIGV assembly was encased within transparent plexiglass to allow clear visualization. In Figure 16, the VIGV assembly is depicted.

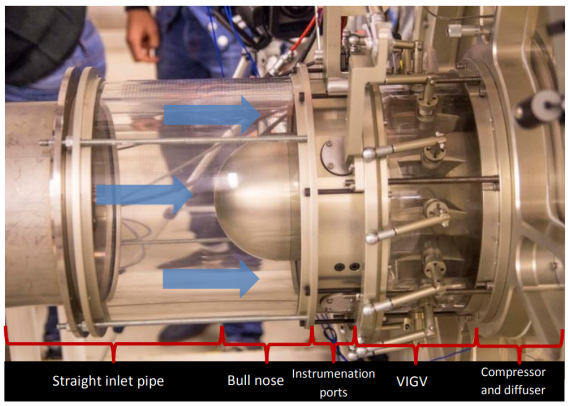

Figure 16: VIGV module configuration. Taken from [29].

Designed with a twisted structure, the vanes featured a 20° deflection angle at the Root Mean Square (RMS), which directed the prewhirl toward the compressor's inlet. The deflection angle varied across the radius, with the highest deflection observed at the tip and the lowest at the hub. The unique configuration of an individual guide vane is showcased in Figure 17

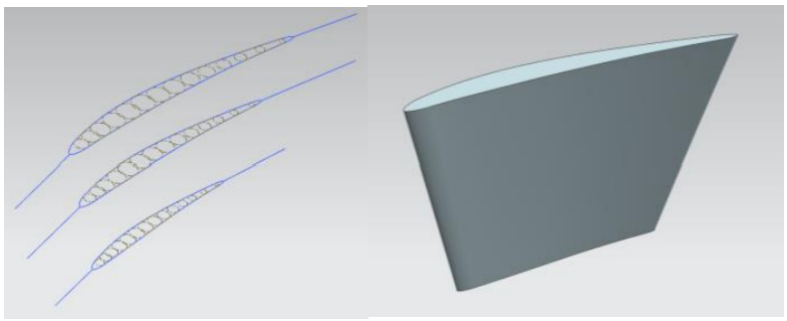

Figure 17: Airfoil geometry. From [10]

The blade chord elongates from the hub to the tip, a design choice influenced by the balance between the preferred VIGV angle variability and the aim for gradual turning and enhanced flow control. The specific airfoil parameters of the VIGV are detailed in Table 3.

Table 3: VIGV Airfoil parameters. From [29]

Name	Symbol	Value
Pitch-cord ratio	p/c	0.7
Chamber angle RMS	θ	20°
Maximum thickness RMS	t	5.3mm
Point of maximum thickness	Xc/c	0.45
Point of maximum chamber	a	0.40
Aspect ratio	h/c	0.68

3.3 Analysing Experimental Results

Ensuring precise post-processing of experimental results is crucial in the development of a data foundation for a digital twin. The subsequent sections detail the methodologies applied for post-processing these results, and highlight the specific EOS employed. In addition, two Python scripts were crafted, taking advantage of the capabilities of HYSYS. Meanwhile, the VibrationData Toolbox, compiled in MATLAB, was utilized for FFT analysis.

3.3.1 HYSYS and EOS

This section describes the different types of components used in calculations from HYSYS.

Before setting up the model, one must choose an EOS and which component list to utilize. HYSYS has inbuilt functions that include pre-defined models and equations that are used for the simulations. From these, one can choose between different packages used in different applications and industries [2]. For low-pressure and temperature operations, the deviation in each package is insufficient. This thesis utilizes the Peng-Robinson equation of state in the calculations as it delivers simple and accurate calculations of air and gases near atmospheric conditions [2].

When selecting a compressor block for the flowsheet, one must choose between centrifugal, reciprocating, screw-compressor, or pump unit [2]. This thesis utilizes HYSYS pre-defined model for a centrifugal compressor block. From there, specifying the operating conditions that can give a precise representation of the compressor system and get the desired performance characteristics of the compressor. Moving on, the material stream is connected to the compressor block. The material stream represents a flow that can be a solid, liquid, gas, or in this case, air in and out from the compressor. It has a start and end point and needs input parameters directly defined, such as; pressure, temperature, and composition, before the calculations can start [2].

3.3.2 Thermodynamical Properties Script

Accurately computing thermodynamic properties is pivotal in the interpretation of experimental results. Crucial parameters such as volumetric flow rate, power, polytropic efficiency, and polytropic head need to be precise when serving as the basis for a digital twin model. The most reliable and accurate method for calculating these necessary thermodynamic properties was determined to be via HYSYS. However, since the volumetric flow rate needed to be calculated from ISO 5167-2 [22], this would require double processing through HYSYS. The initial step involves employing HYSYS to compute thermodynamic properties before the compressor, then leveraging Python to calculate the volumetric flow under these conditions, and finally utilizing a compressor block in HYSYS for the concluding calculations.

This procedure, while comprehensive, could be time-consuming, potentially prone to errors due to manual data entry, and nearly unfeasible for transient tests. Therefore, efforts were invested in exploring the potential for process automation. With the help of the Python package "pywin32", it became possible to control software such as Excel and HYSYS through a Python script. This package was used to create a script that automates the aforementioned process, and several adjustments were made to mitigate uncertainties. The "Thermodynamical Properties Script" has been produced through a collaborative effort with fellow students at the compressor lab.

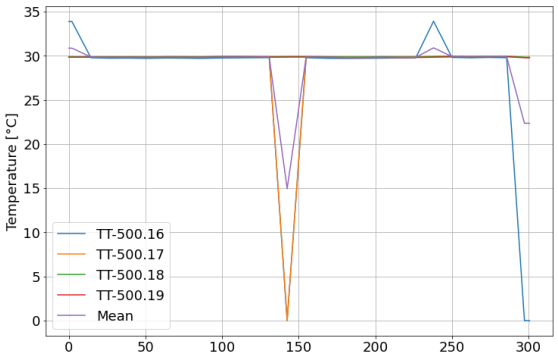

(a) Temperature at compressor inlet.

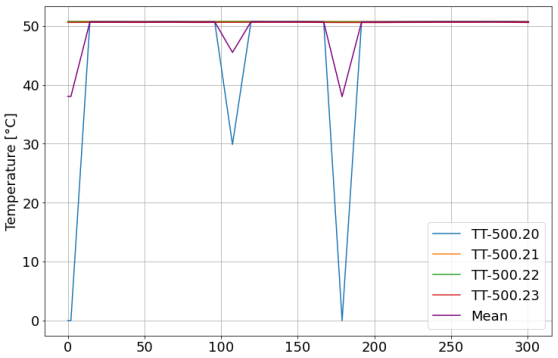

(b) Temperature at compressor outlet.

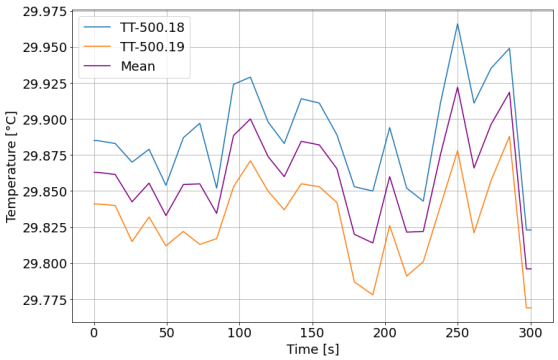

(c) Temperature at compressor inlet after filtering.

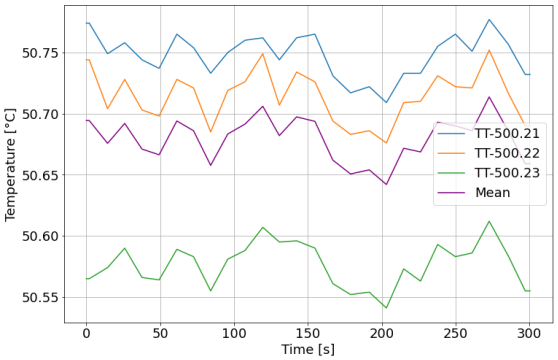

(d) Temperature at compressor outlet after filtering.

Figure 18: Temperature sensors at compressor inlet and outlet at 9000 RPM and ASCV opening of 80% before and after temperature filter.

For the thermally stable test campaign, 18 distinct measurements were carried out. Each of these measurements was stored in an individual Technical Data Management Streaming (TDMS) file. A for loop was programmed to process one file per iteration. A temperature filter was used to discard any sensors that deviated more than 3° from the mean at any point, thereby removing anomalous spikes. Figure 18 illustrates the elimination of these deviating temperature sensors.

The script further simplifies the data by averaging all time steps into a single value for all necessary sensors. It then runs the above-described method through HYSYS and performs volumetric flow calculations. Essential output values, such as power and polytropic efficiency, are collected. Since the polytropic head could not be directly extracted, it was computed according to Equation 11. This comprehensive process is replicated for all experimental data points, and the results are exported to an Excel spreadsheet.

3.3.3 Transient Script

This section outlines the transient iteration of the Python scripts employed in the project, with critical features described for clarity.

Each experimental run generates raw data from many sensors stored in TDMS file format. This raw data requires post-processing prior to any form of analysis. The sensors, diverse in nature, are organized into larger channels, each possessing unique logging frequencies. The frequency variation is dependant on the logging equipment, resulting in temperature sensors typically demonstrating a slower logging frequency compared to pressure sensors. As referenced in 3.3.2, the frequency matching of these sensors is manageable for the thermally stable script, given that all values are aggregated before being used in further computations.

However, frequency matching of these channels becomes critical when conducting transient experiments, due to potential quick changes in operating conditions that need to be accurately captured. A Python script is implemented to synchronize the timestep of each sensor, filling in missing values via linear interpolation when the modified logging frequency surpasses the original. Differences in logging frequencies might introduce a lag related to the start time, often seen with temperature data due to its slower logging frequency. Consequently, low-frequency data must be extrapolated to align with the start point of high-frequency data, using the initial value for all preceding timesteps. This process is repeated for any values beyond the final timestep. Synchronizing the values at each timestep enables calculations at each timestep. Following the findings documented in 3.3.2, temperature sensors that have exhibited significant error rates are removed from the analysis. Subsequently, the remaining temperature sensors are graphically represented for visual inspection. This inspection provides an opportunity to identify and potentially remove any sensors that exhibit anomalous or inconsistent readings, thereby ensuring the reliability and integrity of the data used in the analysis.

The script enabling the connection between Hysys and Python has been adapted for transient scenarios, continuing to utilize the Peng-Robinson EOS as its foundation. Values

are initially synchronized for each timestep in individual scripts for the different scenarios before extraction to a Microsoft Excel file. Subsequently, these values are employed in the Hysys script and, as outlined in section 3.3.2, processed through Hysys to compute thermodynamic properties, such as volumetric flow rate and polytropic head. A notable feature of the updated script is its ability to process real-time values at each timestep instead of aggregated values. Following this processing, the values are exported to an Excel spreadsheet, preparing them for subsequent analysis.

3.3.4 FFT calculation

The FFT of the time series from the piezoelectric sensor, located at the impeller outlet, was calculated utilizing the Vibrationdata toolbox ver 13.3 [11]. The toolbox, compiled in MATLAB, was developed by Tom Irvine for signal analysis and structural dynamics applications. The toolbox used the Cooley-Tukey algorithm for FFT calculations.

The time history of the pressure signals was transformed into an ASCII text file and subsequently input into the toolbox. The performed analyses incorporated FFT, Waterfall FFT, and Spectrograms.

Magnitude calculations were executed using a linear approach. A Rectangular window was predominantly employed for the generation of waterfall and spectrogram plots spanning the 10-6000 Hz frequency range. This choice of window provides optimal frequency resolution, ideal for distinguishing closely spaced frequency components across a broad frequency spectrum.

However, for the analysis focusing on the lead-up to surge, represented by waterfall plots in the 500-2000 Hz domain, a Hanning window with a 50% overlap was used. This approach aids in reducing spectral leakage and provides a smoother time-frequency representation, thus enhancing the visibility of evolving spectral characteristics crucial to surge identification. In addition, the 50% overlap ensures that the data loss inherent to the Hanning window's tapering is minimized, thereby maintaining a uniform contribution from all points in the signal to the final spectrum.

The underlying principles and rationale for these divergent windowing strategies are elaborated upon in section 2.5.

4 Experimental Campaign

This chapter provides an account of the experimental campaign carried out at the NTNU compressor test facility, highlights the concept of "profile test" within the context of this thesis, and presents various definitions.

4.1 Sensor Calibration

Achieving accurate and precise measurements during experimental campaigns is fundamental for developing a robust dynamic model. The absence of such measurements could lead to model formation based on the wrong premises, thereby diminishing its value. Hence, the calibration of pressure sensors was implemented as a critical preparatory step.

The calibrated pressure sensors include the DP sensors at the orifice, the four pressure sensors at the compressor inlet, another four at the compressor outlet, and the DP sensor across the ASCV. There were additional sensors subjected to calibration. However, these have not been elaborated upon since they were not used in this thesis.

4.2 List of Experiments

An experimental campaign has been designed and executed at the compressor facility as a part of this thesis work. The overarching objectives were to enhance the understanding of compressor behavior during transient operation, provide thermally stable performance characteristics as a data basis for a digital twin, and investigate time to surge at varying compressor curve characteristics to be used as training data for the digital twin model. The campaign was organized into four base cases, each tailored to fulfill specific purposes and goals.

To ensure the reliability and reproducibility of the data, maintaining consistent boundary conditions of the system was paramount. The rig was perpetually susceptible to alterations because multiple research projects were concurrently conducted in the laboratory. Consequently, it was determined that all transient experiments should be conducted within a single day to eliminate the possibility of boundary condition changes between tests, thereby minimizing the potential for skewed data.

In order to further guarantee reproducible results, certain rig specifications were established as fixed parameters and maintained consistently throughout the experimental campaign. This approach provided a controlled environment for the transient experiments, allowing for a more accurate assessment of compressor behavior under varying conditions.

All experiments were conducted in collaboration with the laboratory supervisor, Erik Langørgen. Close coordination with fellow students proved mutually beneficial as some experiments were conducted concurrently. This collaborative approach significantly enhanced the efficiency and effectiveness of the experimental campaign for all parties involved and an overall understanding for all involved. Notably, research on the throttle valve, leak-

age in and around the compressor, and flow measurement over the orifice in the NTNU gas Compressor rig was conducted concurrently with this thesis.

Table 4 provides a quick overview of the individual experiments conducted in the experimental campaign.

Table 4: Summary of Experiments

Date	**Case**	**Focus of experiment**	**Frequency**
28.02.2023	Case 1	Thermally stable compressor curves at 9000 RPM, 8 points for IGV0, 5 points for IGV-15 and IGV30. Two additional points at 11000 RPM.	2 Hz. 20 000 Hz at V43 to use for FFT analysis of the surge point.
02.05.2023	Case 2	TTS at the same operating point for all IGV angles.	10 Hz and 20 000 Hz.
02.05.2023	Case 3	TTS at the same rotational velocity and ASCV opening for all IGV angles.	10 Hz and 20 000 Hz.
02.05.2023	Case 4	TTS trip scenario at the same operating point for all IGV angles.	10 Hz and 20 000 Hz.

Profile test

The standardization of the experimental tests was imperative in order to minimize potential sources of error. Establishing a standardized dynamic test facilitated various aspects of the process: it enabled a more straightforward comparison of results, as only the variable under immediate investigation was altered between consecutive experiments; it simplified the execution of the experiments, owing to a consistent methodology; and lastly, it enhanced the practical reproducibility of the tests by providing clear procedural guidelines, thus ensuring the ease of replication.

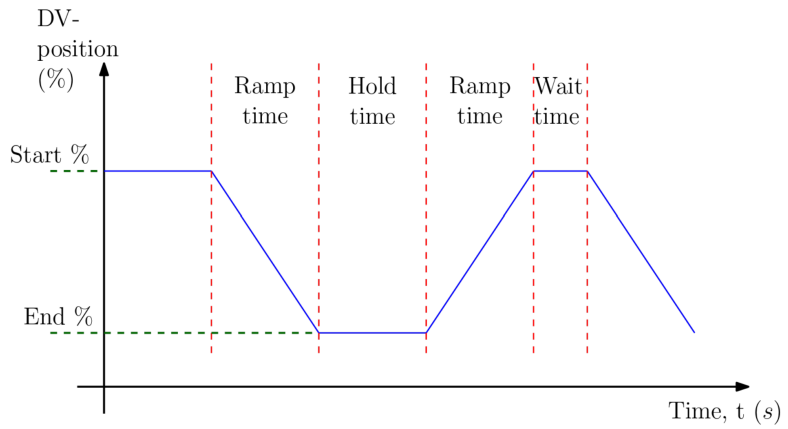

Figure 19: Some basic definitions and terminology for specifying profiles concerning the position of the ASCV.

The profile test was extensively used in the tests, which formed the basis for the TTS results in section 5.2. Figure 20 and table 5 show the profile test used in Cases 2 and 3. Figure 19 describes the terms used in the profile test; this was derived directly from the operating software.

Table 5: Showing the parameters of the tests done in Case 1

What	Value
Ramp Time	1s
Hold Time	5s
Wait Time	5s
Start position of ASCV	80-81%
The end position of ASCV	38%
Repeated	3

To minimize potential sources of error, the standardized profile test was uniformly applied for Case 2 and Case 3. Each profile test employed a gain of 0.5 on the ASCV, the implications of which are illustrated in Figure 20. In this figure, one can observe that the actual setpoint of the valve decelerates when approaching the smallest valve opening, effectively creating an extended ramp time. This precautionary measure was implemented to prevent the valve's actual position from surpassing the lowest setpoint opening.

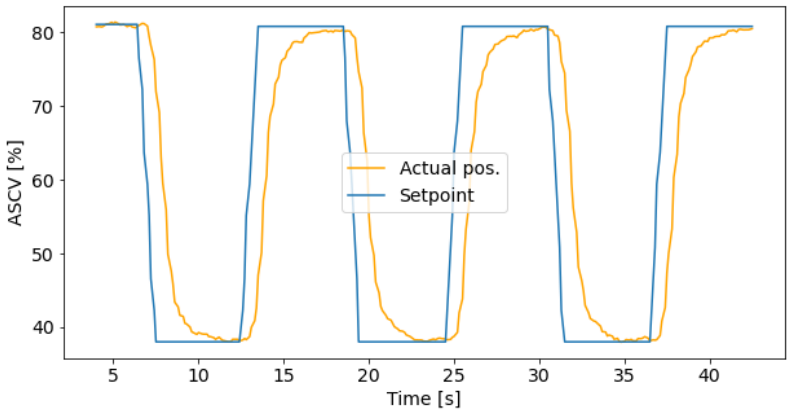

Figure 20: Showing the opening and closing of the ASCV during the profile test done for all transient tests.

Logging Frequency

The logging frequency spectra at the NTNU testing facility are categorized into two groups: normal logging frequency and high-speed logging frequency. The maximum logging frequency for the normal spectrum is 10 Hz, whereas the high-speed spectrum can reach up to 20,000 Hz. However, high-speed logging only includes other sensor groupings within the PXI logging equipment. Moreover, high-speed logging generates a considerable volume of measurement points, resulting in data-dense files that are computationally challenging to

manage effectively.

Normal frequency spectra were primarily employed for the experiments conducted in this thesis. Thermally stable tests under static operating conditions utilized a 2 Hz logging frequency, as higher frequencies merely produced larger datasets with negligible additional information. In addition, transient tests were performed at 10 Hz, the highest logging frequency within the normal spectrum, as TTS tests typically involve rapid changes in operating conditions.

In addition to normal-speed logging, all transient tests were logged at a high-speed frequency of 20,000 Hz. High-speed logging was also applied to the lowest volumetric flow points in the thermally stable test. The high-speed logging data was exclusively utilized to examine the pressure signals' frequency content at the impeller outlet. This analysis was conducted through FFT techniques, which will be elaborated upon in Section 5. FFT analysis on the same sensor has provided valuable insight previously as seen in [8].

4.2.1 Case 1 - Static conditions performance

Establishing an accurate and reliable database is paramount for developing a digital twin using machine learning techniques. Ensuring thermal equilibrium during testing facilitates the generation of consistent and repeatable data, which, in turn, supports the effective training and validation of the digital model. Consequently, significant effort was devoted to conducting the tests in this study under thermally stable conditions as much as possible.

To achieve this, baseline criteria were established and adhered to throughout the thermally stable testing phase. Thermal equilibrium was deemed achieved when none of the temperature sensors within the system exhibited a temperature change exceeding 0.5°C over 5 minutes. Once this condition was met, the sensor output was recorded for a subsequent 5-minute period. By following these criteria, the testing process aimed to ensure the highest possible data quality and reliability for developing the digital twin.

The tests were also done at static conditions, meaning that ASCV opening and rotational speed were held at constant conditions during the 5-minute testing periods. A total of 20 static tests were completed, most at 9000 RPM and some at 11000 RPM. As can be seen in Table 6 the actual rotational speed is not the same as the set speed. This is the case for all the tests done in the experimental campaign, but only the actual setpoint will be mentioned in most instances. The tests done at 11000 RPM were used to validate the use of affinity laws, which will be further described in 5.1. There were also, in total, ten static tests done at 30° prewhirl and at negative 15° prewhirl to acquire different curve characteristics.

After the test data was acquired, it was post-processed using the script described in section 3.3.2. This gathered important information about the compressor characteristics for all testing points. Notably, pressure ratio, polytropic head, polytropic efficiency, and power were calculated.

Table 6: Thermal stability test at all three IGV angles

Shaft speed (RPM)	**Valve opening [%]**	**Q [m³/s]**	**Hp [kJ/kg]**	η_p [%]	**Power [kW]**	**Pr [-]**
IGV0						
9021.1	43	0.684	19.03	71.21	21.70	1.233
9022.3	50	0.804	18.78	75.90	23.60	1.231
9021.8	57	0.927	18.45	78.80	25.69	1.227
9021.9	64	1.030	18.06	79.94	27.47	1.222
9021.9	72	1.129	17.35	80.82	28.59	1.213
9021.9	80	1.222	16.63	80.43	29.73	1.203
9021.8	90	1.297	15.99	80.61	30.24	1.195
9021.5	100	1.372	15.26	79.25	31.02	1.185
11024.2	50	1.015	28.17	78.61	42.72	1.356
11024.3	80	1.513	25.24	82.07	54.18	1.316
IGv-15						
9022.0	43	0.678	19.17	71.93	21.48	1.227
9022.3	50	0.810	19.02	73.88	24.71	1.222
9021.9	64	1.041	18.47	77.79	29.19	1.205
9021.7	80	1.249	17.38	78.20	32.66	1.181
9021.6	100	1.409	16.13	76.91	34.64	1.161
IGV30						
9022.2	43	0.670	18.54	72.73	20.30	1.236
9022.1	50	0.790	18.05	76.59	22.09	1.234
9021.8	64	0.992	16.77	79.21	24.83	1.227
9021.9	80	1.158	14.93	78.65	25.91	1.213
9021.5	100	1.285	13.38	76.63	26.41	1.196

4.2.2 Case 2 - Time to surge - given operating point

Table 7: Profile test for case 2

What	**Case 2**		
Ramp Time	1s		
Hold Time	5s		
Wait Time	5s		
	IGV 0°	**IGV 30°**	**IGV -15°**
Start position of ASCV	80%	81%	80%
RPM	9026	9728	8825
End position of ASCV	38%		
Repeated	3		
Logging Frequency	10 Hz and 20 000 Hz		

Case 2 was designed to investigate the TTS for distinct curve characteristics, with the operating point maintained at the same initial location for all characteristics. The standardized profile test, as delineated in Section 4.2, was employed for this examination. The ASCV and the rotational velocity were adjusted to achieve an operating point with a consistent volumetric flow and pressure ratio. The operating point was determined through a real-time visual assessment of the compressor map displayed in the software utilized at the NTNU compressor rig. Table 7 provides an overview of the three ramp tests conducted for Case 2.

Various IGV angles were implemented to generate the different curve characteristics: 0°, 30°, and -15°. To attain a comparable operating point, the rotational velocity was modified from 9,000 RPM to 9,700 RPM for the 30° prewhirl and from 9,000 RPM to 8,800 RPM for the -15° prewhirl. The ASCV opening was adjusted from 80% to 81% for the 30° prewhirl, remaining constant for the 0° prewhirl.

4.2.3 Case 3 - Time to surge - given RPM

Table 8: Profile test for Case 3

What	**Case 3**		
Ramp Time	1s		
Hold Time	5s		
Wait Time	5s		
	IGV 0°	**IGV 30°**	**IGV -15°**
Start position of ASCV	80%	80%	80%
RPM	9026	9728	8825
End position of ASCV	38%		
Repeated	3		
Logging Frequency	10 Hz and 20 000 Hz		

Case 3 was conducted to analyze the TTS for varying characteristics operating at a consistent rotational velocity. The objective was to investigate TTS at the same ASCV opening and the same rotational velocity of the impeller. The standardized profile test, as detailed in Section 4.2, was employed for this examination. The profile test remained consistent for all tests in Case 3, with the sole distinction being the angle of the IGV. IGV angles of 0°, 30°, and -15° were again utilized to generate the different curve characteristics. Table 8 shows the profile test applied in Case 3.

4.2.4 Case 4 - Trip scenario

Table 9: Profile test for Case 4

What	**Case 4**		
Ramp Time	1s		
Hold Time	2s		
Wait Time	0s		
	IGV 0°	**IGV 30°**	**IGV -15°**
Start position of ASCV	80%	81%	80%
RPM	9026	9728	8825
End position of ASCV	38%		
Repeated	1		
Logging Frequency	10 Hz and 20 000 Hz		

Case 4 was carried out to investigate the behavior of the compressor during a trip scenario across various HRTS, with the starting point consistent with that used in Case 2. The conventional profile test was adjusted, shortening the hold time from 5 seconds to 2, eliminating the wait time, and carrying out only a single cycle instead of three. Hence, the profile was enacted only once per experiment. The trip scenario shows a notable contrast between Case 4 and Cases 1 and 2. The compressor trip was triggered by switching off the "run impeller" option, which cut power to the impeller from the motor, leading to an impeller trip. The ramp test was launched concurrently with the power interruption to the impeller. However, some uncertainty may exist due to the manual process of activating the options simultaneously. The experiment was deemed complete when the rotational velocity had reduced to roughly 4000 RPM. Table 9 shows the profile test applied in Case 4.

4.3 Changing Curve Characteristics

As described in Section 2.2.3, HRTS exhibits considerable potential to influence the TTS at a specified operating point within the compressor map. Accurate determination of TTS is crucial for establishing the control line on a compressor map. As such, precise measurement is essential for defining a given compressor's feasible operating region on the compressor map. As a vital objective of this study is to demonstrate these effects through real-world experimental investigations, it is imperative to establish a methodology for replicating diverse curve steepness characteristics.

The NTNU testing facility, as referenced in Section 3, is outfitted with VIGV. These vanes permit adjustments to their angle of attack. As discussed in Section 2.3, altering the angle of attack from the IGV can significantly impact the characteristic curves for a specific compressor. The experimental campaign incorporated three distinct IGV openings, which will be subsequently referred to as normal, steep, and flat. For the normal characteristic, the opening was maintained at a zero-degree angle. A positive prewhirl angle of 30° was

employed for the steep characteristic, and a negative prewhirl angle of 15° was utilized for the flat characteristic.

4.4 Defining Boundary Conditions

Conducting dynamic tests necessitates clear procedural guidelines not only for the execution of these tests but also for the subsequent data post-processing. As such, precise definitions will be established that underpin the results in sections 5.3, 5.4, and 5.5.

Three critical parameters in the graphical representations within these sections require explicit definition: the initiation of the surge trajectory, the point at which surge transpires, and the point when the operating point transitions out of the surge state.

Establishing the Start Time for TTS Analysis

The initiation of the surge trajectory is defined as the timestep immediately before the ASCV setpoint begins its descent toward a lower opening. This definition guarantees correlation in the starting conditions across all tests, thereby preventing discrepancies that might be introduced due to variations in response times. Differing curve characteristics or other factors could influence such variations.

Defining the Onset of Surge

Surge is a complex phenomenon, and defining the onset of surge can be difficult. Three different methods have been used to determine when the onset of surge is initialized. Each method has its restrictions, but together they are considered sufficiently accurate to determine the onset of surge in this thesis. The three methods used are:

- Utilizing a SL defined in the thermally stable tests.
- Looking at the gradient of the characteristic curves.
- FFT analysis of pressure at the impeller outlet.

Firstly, a specific SL derived from thermally stable tests determines the surge criterion. A detailed account of the method used to define this line is provided in section 5.1. This method sets a clear line for the onset of surge and makes it easy to define when the operating point has moved into the surge region. The method, however, has its drawbacks. These are threefold: uncertainty of the correct placement of the SL, uncertainty in volumetric flow calculation at low flow rates, and thermally stable as opposed to unstable conditions.

Firstly there was some uncertainty in the placement of the SL, as it was decided from a visual and audio test during the experimental campaign. The SL was also placed at an operating point where the compressor could operate for an extended period without

causing damage to the compressor. As such, there is a high likelihood that the compressor line is placed right before the onset of surge rather than in the surge area. Secondly, there is a more considerable expanded uncertainty in the lower flow region, as shown in Appendix D. This uncertainty casts some doubts as to whether one can trust only a volumetric flow analysis when deciding when surge has been initiated, and it necessitates the use of other analytical methods. Lastly, the volumetric flow in the thermally stable test may be removed from the volumetric flow found in transient testing, where operating conditions change very fast. This may have some impact and will be further described in section 5.2.

The second method used in this thesis is conducted by looking at the gradient of the characteristic curves. A positive continuous head rise to the compressor surge point at constant speed is crucial to stable compressor operation and reliable, responsive process control [14]. Using this method is a good way to gauge the onset of surge but may only be sufficient with utilizing other methods in the cases conducted in this thesis. As transient tests are volatile, there may be some oscillations in the polytropic head from measurement point to measurement point; therefore, changes in the polytropic head from one timestep to another may not be an entirely usable metric. Therefore, The decision was to look at the total curvature of the transient characteristic towards surge. This results in being unable to look at the exact operating point and necessitates the use of other methods.

The third and final method used is the FFT analysis of a piezoelectric pressure sensor placed at the impeller outlet, as highlighted in section 3. Results obtained using high-speed logging frequency at the thermally stable surge point indicate the magnitude expected when surge is reached for the transient tests. The transient high-speed datasets are matched with the 10 Hz datasets to show the changes in magnitude in a waterfall FFT as the operating point moves toward surge. These figures contribute significantly to understanding the oscillations in pressure during TTS and further validate the findings from the two previously mentioned methods.

The onset of surge is marked by the operating point moving to the left of the SL. In contrast, the transition out of surge is defined as the moment when the operating point repositions itself to the right of the SL. These definitions provide a framework for understanding the results and patterns observed during the dynamic testing shown in sections 5.3, 5.4 and 5.5, and increase the repeatability of these tests.

5 Results and Discussion

This chapter presents the outcomes and the accompanying discussions derived from the conducted experiments. Experimental results and corresponding discussions have been divided into two key categories: static and transient experiments.

Case 1 focuses on experiments executed under static conditions, providing a thermally stable data foundation for the digital model.

On the other hand, Cases 2 through 4 pertain to experiments carried out under transient conditions, primarily investigating the impact of HRTS on TTS and, in the context of Case 4, TIS. The data compiled from these transient cases will form a valuable database in future machine-learning applications for developing a digital twin of the compressor lab.

5.1 Case 1 - Static conditions performance

Table 6 in section 4.2.1 shows an overview of the tests done at thermally stable conditions. Notably, pressure ratio, polytropic head, polytropic efficiency, and power have been calculated as shown in Figure 21. A second-degree regression curve is fitted to all the data points to illustrate the complete curve characteristics. Apparent differences can be seen between the three different curves in all plots.

The green curve describes the normal steepness and would constitute original operating conditions. The blue curve describes a flatter characteristic, and the red curve shows a steeper characteristic. The red and blue curves can be assimilated to different compressor degradation in real-life operating conditions.

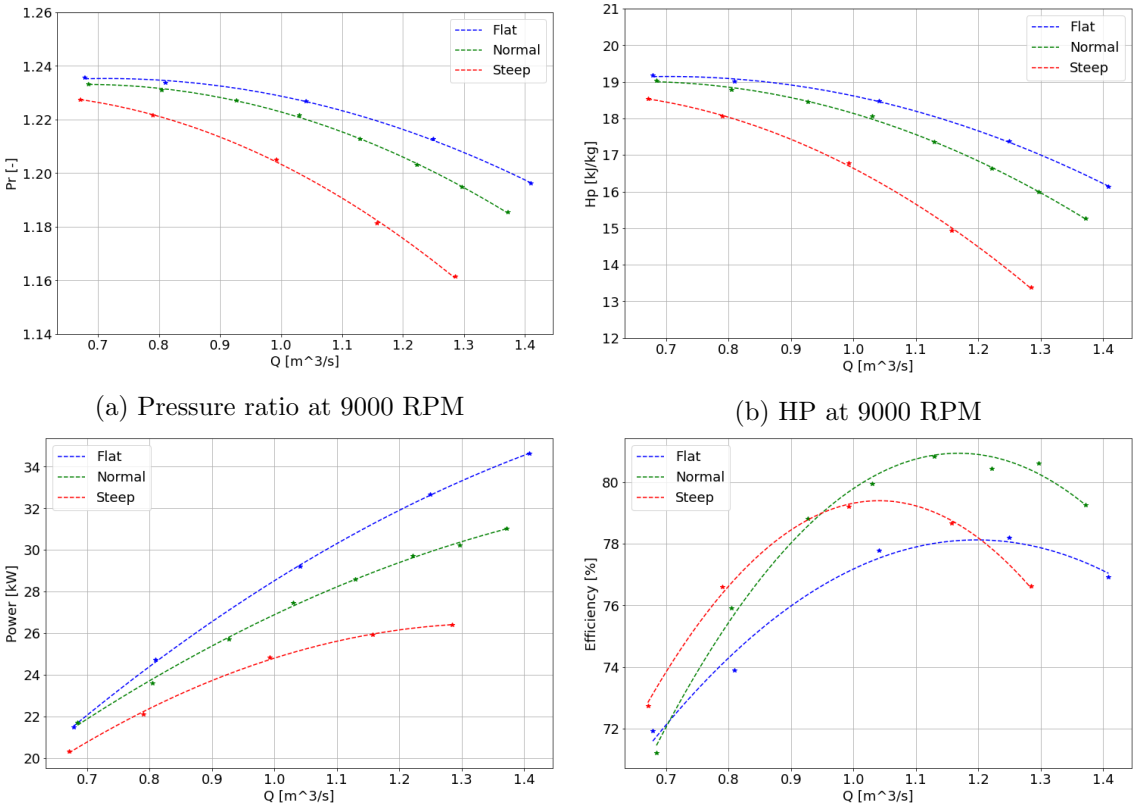

(a) Pressure ratio at 9000 RPM

(b) HP at 9000 RPM

(c) Power at 9000 RPM

(d) Polytropic efficiency at 9000 RPM

Figure 21: Compressor characteristic curves at 9000 RPM for flat, normal and steep characteristics.

The steeper curve generally shows significantly lower values in pressure ratio, polytropic head, and power. It also has a lower polytropic efficiency than the normal curve but higher than the flat curve. Although the flat curve has the lower polytropic efficiency of the three curves, it also has the highest pressure ratio, polytropic head, and power values. It should be noted that the steep curve has been made using double the offset in degrees of rotation compared to the flat curve, which may cause it to exhibit more significant discrepancies to the normal curve than that of the flat curve.

The placement of the SL is an important consideration when looking at compressor characteristics and creating the compressor map. There are different ways to determine the SL experimentally. The two ways used during the experimental campaign were looking at the compressor's acoustic signature and the slope of the characteristic curve of the compressor. For the acoustic signature, the test was listening to the sound of the compressor and mapping the point at which the noise from the compressor became more pronounced. For the characteristic curve, there was a possibility in the software connected to the compressor to map the history of the operating point. Using this mapping, it was possible to find the point at which the rate of increase of the slope became negative. Combining these two methods was considered accurate enough to determine the surge's point. At this point, the rotational speed was set as 9000 RPM, and the ASCV opening was set to 43% opening; these conditions were chosen for all three curve steepnesses.

Differing flow rate at the same operating conditions is expected and can be seen in Figure 21. An interesting condition to look at is the degree of surge the different curve characteristics experience at the SL with the given conditions. A way to analyze this is using FFT analysis, which is described in section 2.5. The process of FFT calculation and the sensor used for the calculations is described in section 3.3.4. This method will be the basis for all FFT analysis results, both for thermally stable and transient tests. On the y-axis of the plots in Figure 22, a value denoted magnitude can be seen, which is the amplitude of the frequency components in the signal.

The magnitude calculation has been performed using a linear approach. The high-speed datasets from the dynamic pressure sensors are presented in mBar. The magnitude component of the FFT plots are presented in mBar on a linear scale, showing the strength of the pressure variation at each frequency. Throughout this thesis, this measure will predominantly be referred to as the 'magnitude'.

Figure 22 shows the FFT for all curve characteristics at the defined surge point - 9000 RPM and ASCV opening of 43%. They are all shown in the specter of 0-6000 Hz, although the frequencies below 0.3 Hz are cut out due to unwanted noise. All three characteristics show a significant amplitude at 1353 and 2706 Hz. Using the BPF equation 22 to calculate the number of blades in the impeller, the number of blades is found to be 9 and 18. This is natural, as the impeller consists of 18 blades - 9 long and 9 short; a representative impeller can be seen in figure 15a. There are also peaks at 4059 and 5412 Hz; these peaks can be described as double the blade passing frequencies.

The magnitude is most prominent for the flatter curve at half the BPF, second most prominent for the normal curve, and smallest for the steepest curve. The normal and steeper curve also shows a better correlation between the 0.5BPF and BPF points, whereas there is a large discrepancy between the two for the flat curve. The stronger correlation between all the peaks shown in the steeper characteristic FFT can indicate a more stable operating condition and, therefore, a less pronounced surge. The prominent peak at 0.5BPF, shown in the flatter curve, could indicate a more pronounced surge operation. Looking at Figure 21, the point at lower volumetric flow in the compressor map for the flatter curve is clearly to the left of the expected point, which could mean that it is in more pronounced surge than the other operating points. This becomes clearer in Figure 26, where the flat curve starts slightly to the left of the SL created from the normal operating points.

Figure 23 illustrates the optimal polytropic efficiency points for each curve characteristic and their corresponding positions on the polytropic head curves. A notable disparity in the maximum polytropic efficiency is observed among the three distinct curves. The highest polytropic efficiency is attained at 80.93% for the normal curve, followed by 79.39% for the steep curve, and finally, 78.12% for the flat curve.

While the difference in polytropic efficiency between the normal and steep curves is relatively small, a substantial contrast exists in the polytropic head and volumetric flow. Specifically, the polytropic head measures 17.08 kJ/kg for the normal curve, 16.26 kJ/kg for the steep curve, and 17.67 kJ/kg for the flat curve. Regarding volumetric flow, the

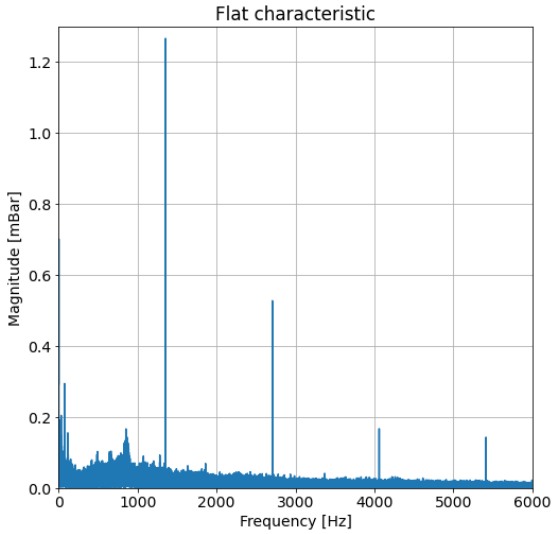

(a) FFT from 0-6000 Hz at flat characteristic.

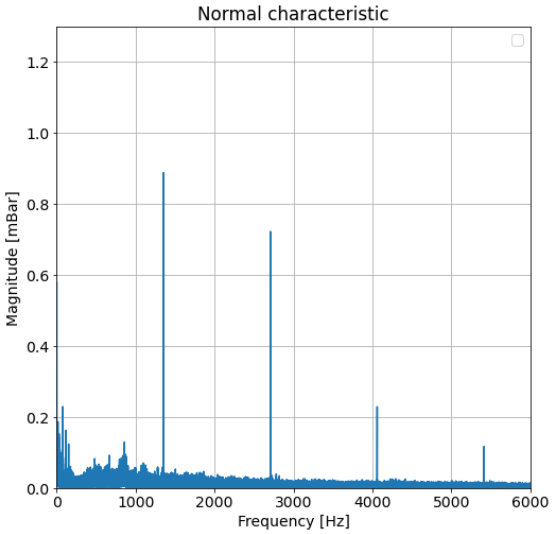

(b) FFT from 0-6000 Hz at normal characteristic.

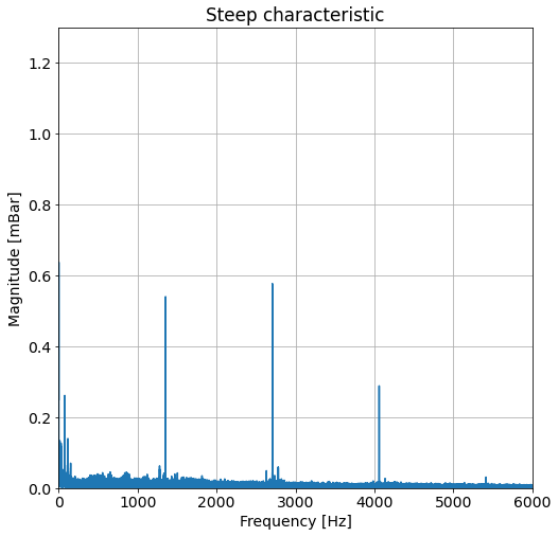

(c) FFT from 0-6000 Hz at steep characteristic.

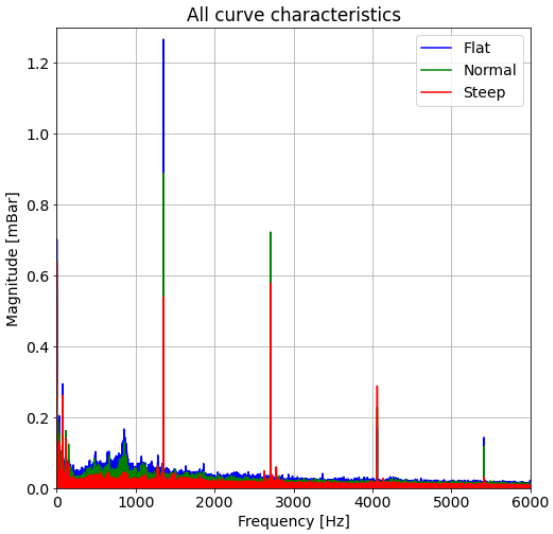

(d) FFT from 0-6000 Hz for all characteristics.

Figure 22: FFT from 0-6000 Hz at three curve characteristics.

values are 1.17 m^3/s for the normal curve, 1.04 m^3/s for the steep curve, and 1.2 m^3/s for the flat curve.

The optimal operating point for the flat curve is characterized by both a higher polytropic head and a greater distance from the SL in the x-axis dimension, albeit with a reduced HRTS. Conversely, the steep characteristic exhibits a lower polytropic head and volumetric flow but benefits from increased HRTS.

In a centrifugal compressor, the power can be calculated using two distinct methods: fluid power and mechanical power. The fluid power method employs fluid properties to compute the power required to compress the fluid, as demonstrated in Equation 11. Conversely, the mechanical power method relies on the torque applied to the impeller and the rotational speed to determine the mechanical power input to the compressor, as

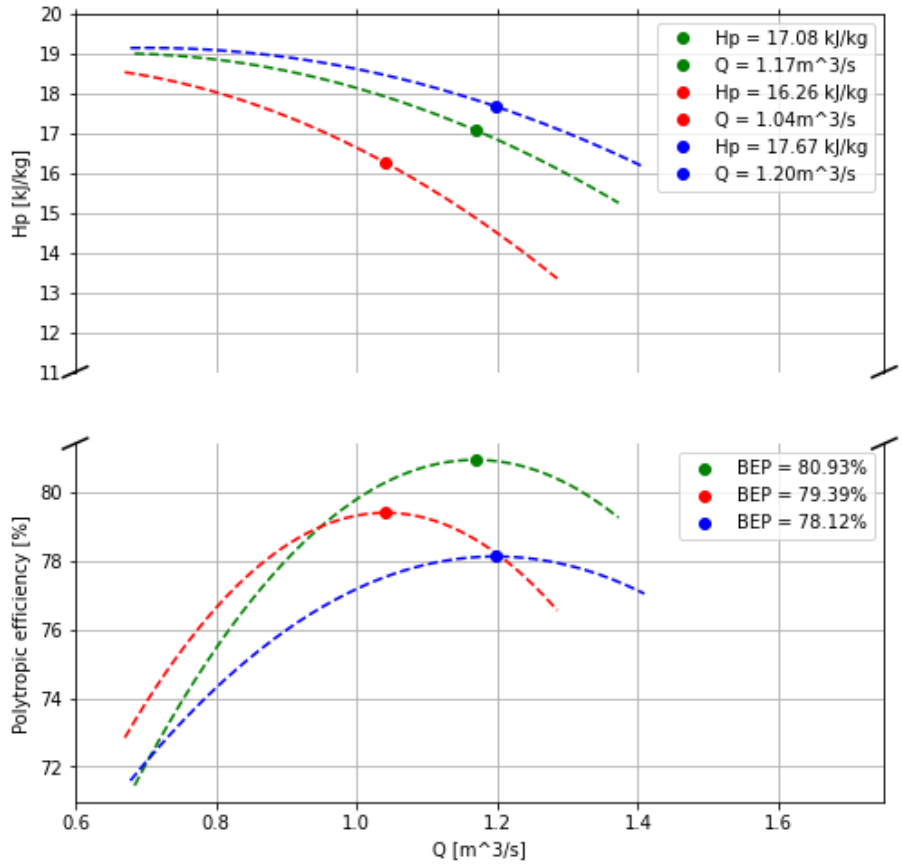

Figure 23: Polytropic head and polytropic efficiency plots at BEP for all IGV angles. The points represent the best efficiency points.

illustrated in Equation 1.

During a thermally stable test, the system's temperature remains constant, which should ensure the consistent performance of the compressor. Assuming this condition is met, the two power calculation methods should correspond closely. Figure 24 presents a QQ-plot of the two power values, with mechanical power on the x-axis and fluid power on the y-axis. The measured values exhibit minimal deviation from the 45°line, suggesting little deviation and a strong correlation between the two datasets.

Affinity laws

For a DT of a compressor, a complete compressor map is essential when doing simulations at different rotational speeds or transient tests where the operating conditions change quickly, and one may end up with operating conditions outside of the characteristic line. The affinity laws have been used extensively by the industry and within process simulation tools (e.g., Hysys Dynamics) for performance scaling and estimation [6]. As thermally stable tests are very time and energy-consuming, two characteristic curves were chosen to be calculated using the affinity laws 2.2.2. These curves were decided to be calculated for 7000 RPM and 11000 RPM. They would be used as endpoints in the digital twins, where

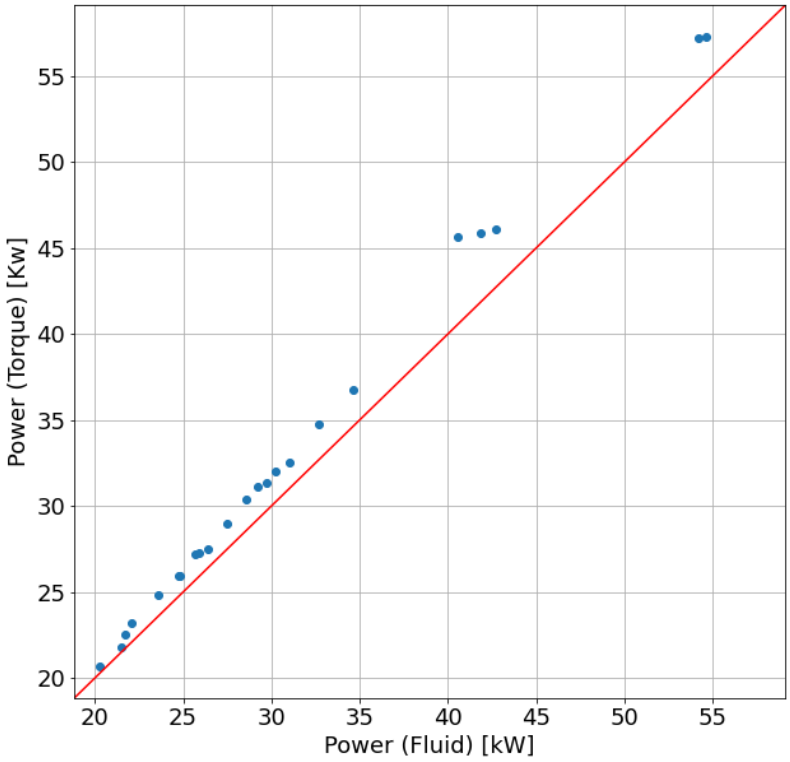

Figure 24: QQ plot showing the difference between torque power and fluid power.

conditions could be simulated between the characteristic lines.

In order to assess the accuracy of the characteristic lines derived from the affinity laws, experimental points were needed at the new characteristic line. It was decided that these points would be placed at 11000 RPM with an ASCV opening of 50% and 80%. As mentioned in section 4.2.1, there is a discrepancy between the actual and set rotational speeds. While the affinity curves to be used as the foundation for the DT were calculated at 7000 and 11000 RPM, the calculation had to be done at about 11024 RPM when assessing accuracy compared to the experimental points to match the actual rotational speed of the compressor. The accuracy of the polytropic efficiency curves will not be validated since a prerequisite for the affinity laws is that the polytropic efficiency is kept constant.

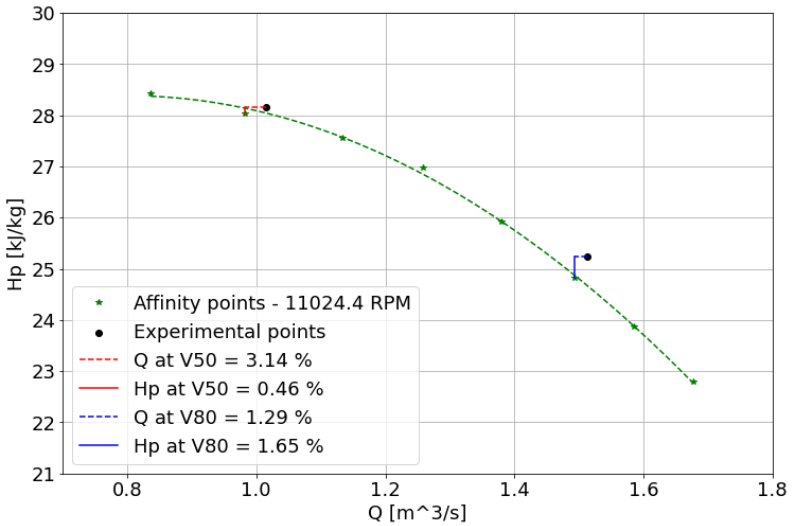

(a) Hp difference between experimental points and affinity law at 11024 RPM

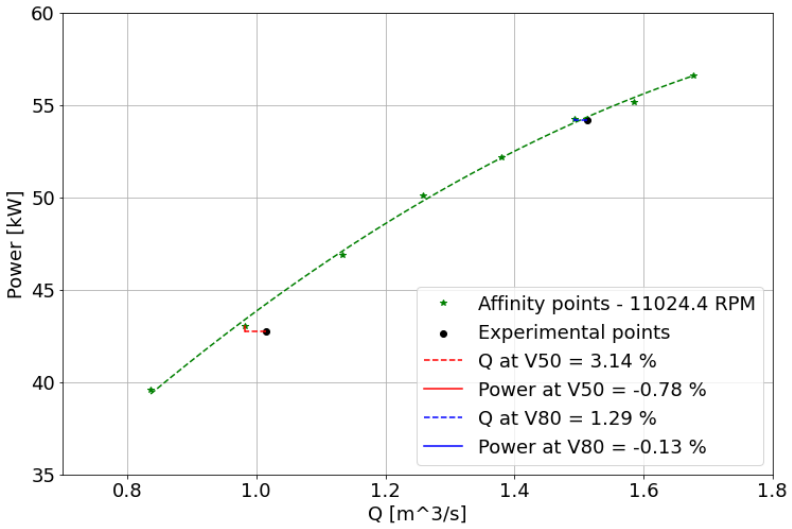

(b) Power difference between experimental points and affinity law at 11024 RPM

Figure 25: Difference in experimental points at 11024.4 RPM and the affinity points at the same RPM.

Figure 25 shows the difference between the polytropic head, power, and volumetric flow between the curves calculated from the affinity laws and the experimental points. The percentage difference has been calculated using the relative change formula. The difference in volumetric flow is 3.14% at 50% opening and 1.29% at 80% opening. The difference in the head is 0.46% at 50% opening and 1.65% at 80% opening. Finally, the difference in power is -0.78% at 50% opening and -0.13% at 80% opening. These results show some discrepancy between the affinity laws and experimental conditions but are seen as accurate enough at this time. When a real-life DT is to be created, it could be essential to gather the 11000 and 7000 RPM curves via thermally stable experiments.

In Figure 26, the compressor map for all three curve characteristics and the surge and

Choke Line (CL) are shown. The SL and CL are set based on the beginning and end points of the normal characteristic lines at the three different RPMs. As mentioned previously, it is clear that the starting point of the flatter curve is positioned to the left of the SL.

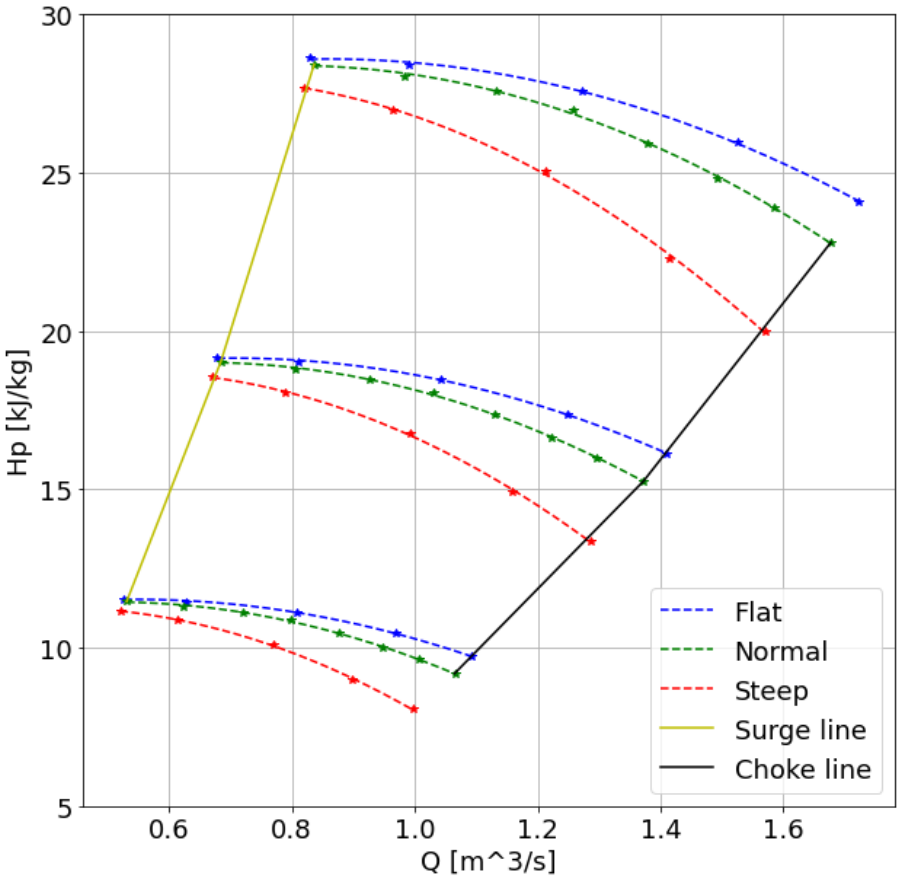

Figure 26: Hp curves at every IGV angle for 7000 RPM, 9000 RPM and 11000 RPM using the affinity laws for the 7000 RPM and 11000 RPM curves. Surge and Choke line are both set on the boundary of the normal curves.

5.2 Transient Tests

There are significant differences between static and transient tests. This section introduces the result section of the three transient cases done in the experimental campaign. Transient results will be compared to thermally stable static results. Furthermore, this section will also provide a preliminary overview of the transient cases examined. Scatter plots of the time-series from the experimental campaigns used for Cases 2-4 are provided in Appendix A.

Transient vs Thermally Stable

Case 3 employed the profile test, as described in Section 4.2, with a specified rotational velocity and ASCV opening for all three curve characteristics. A detailed description of these tests can be found in Section 5.4. However, utilizing the information obtained from these tests to highlight the differences between transient and thermally stable tests is helpful. Ideally, the transient curves should commence at the point corresponding to the 80% ASCV opening for all the thermally stable curves and proceed along the path toward the SL.

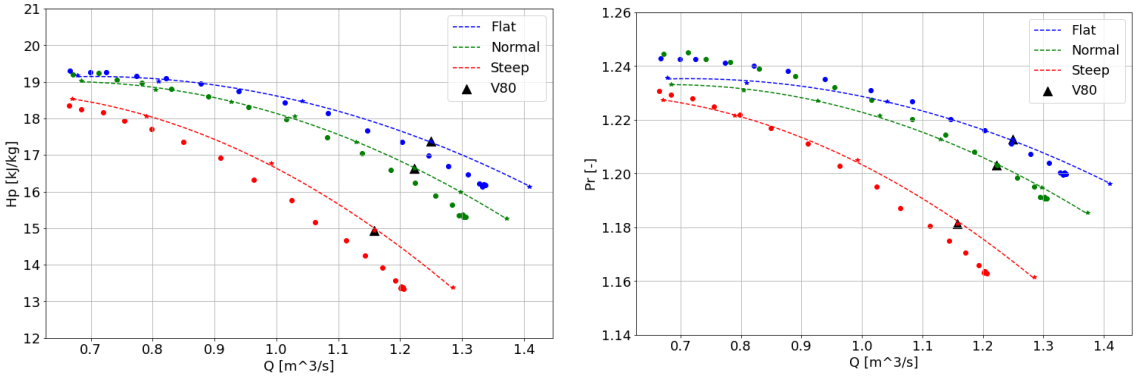

(a) (b)

Figure 27: Difference in the polytropic head (27a) and the pressure ratio (27b) between thermally stable and transient tests.

Upon examining Figure 27, it is evident that the volumetric flow for both plots at the initial condition of the transient test is significantly larger than the 80% ASCV opening point observed in the thermally stable curves. This discrepancy may be attributed to different factors, such as the influence of the ambient air inlet temperature in the testing lab on the inlet pressure, affecting the DP across the orifice. However, the primary factor is believed to stem from variations in the rig's setup, particularly concerning the positioning of the outlet valves.

As described in Section 3, the REXA valve was situated behind both the ASCV and DCV at different instances. During the thermally stable test, the valve was positioned behind the ASCV, which was utilized for flow control. Conversely, in the transient tests outlined in this section, the valve was placed behind the DCV while the ASCV managed

the flow. Consequently, the additional restriction imposed by the REXA valve is deemed a significant contributor to the increased volumetric flow observed at the same ASCV opening.

The pressure ratio for all transient curve characteristics demonstrates a consistent trend of gradual increase compared to the thermally stable characteristics when moving toward a lower volumetric flow. This outcome is anticipated due to the disparities between thermally stable and unstable tests. Although variations in inlet temperature exist between the two tests, these differences remain constant from high to low. Conversely, the outlet temperature discrepancies become increasingly pronounced as the operating point shifts toward lower flow. In thermally stable testing conditions, the compressor exhibits a considerably higher temperature at lower flow rates, whereas during transient tests, it lacks sufficient time to warm up. Consequently, the compressor imparts a cooling effect on the inlet air, leading to a reduced outlet temperature for transient tests as opposed to thermally stable ones. A lower outlet temperature relative to the inlet temperature signifies a higher outlet pressure than the inlet pressure, ultimately resulting in an elevated pressure ratio.

Time To Surge

Many methodologies were employed to investigate the phenomenon of time to surge, encompassing the testing conditions and the criteria for determining the onset of surge. These diverse approaches facilitated a comprehensive understanding of the intricacies of surge development and the factors that influence its occurrence.

Three different testing conditions were investigated. Two were tested using the ramp test outlined in section 4.2, where the different curve characteristics were placed on the same operating point using differing ASCV openings and different rotational velocities of the compressor. The second was conducted with the same ASCV opening and rotational speed, resulting in a varying starting operational point for the different characteristics. Finally, a third test was conducted to look at TTS and TIS for different compressor characteristics during a trip scenario.

From section 5.2, the polytropic head was found to garner the values closest resembling the characteristic curves from the thermally stable tests. The values plotted against each other in the following sections will be polytropic head plotted against the volumetric flow. This also gives the best possibilities for comparison with the whole compressor map, as the values from the affinity laws have not been calculated in pressure ratio.

As shown in section 4.4, different methodologies have been used to define when the onset of surge occurs. The following sections will describe the results found from each case and further analyze TTS using the different surge conditions.

5.3 Case 2: TTS - Same Operating Point

Case 2 involved analyzing TTS for varying curve characteristics using the same starting operating point in the compressor map. The method used has been outlined in section 4.2.2. The boundary conditions have been defined in section 4.4, where the onset of surge will be further looked into in sections 5.3, 5.4 and 5.5. The purpose of Case 2 is to asses how TTS is impacted by the different curve characteristics and their HRTS at the same starting operating point.

Figure 28 shows the TTS data points from all ramp test repetitions plotted against the static compressor map found in Case 1. The transient data points show a good correlation with each other, implying relatively small changes between the three repetitions of the ramp. The transient point for normal curve steepness also shows good agreement with the equivalent thermally stable curve, as discussed in section 5.2. The Figure also shows the SL and CL extracted from Case 1. The SL has an inclined degree of ascent, which could potentially affect the TTS for the transient tests instead of using a set volumetric flow value. As there is some uncertainty in the way the SL has been found and the findings from the FFT plots - a decision was made to use a fixed volumetric flow rate as the standard SL for the TTS experiments. The value was set to be the same for all cases.

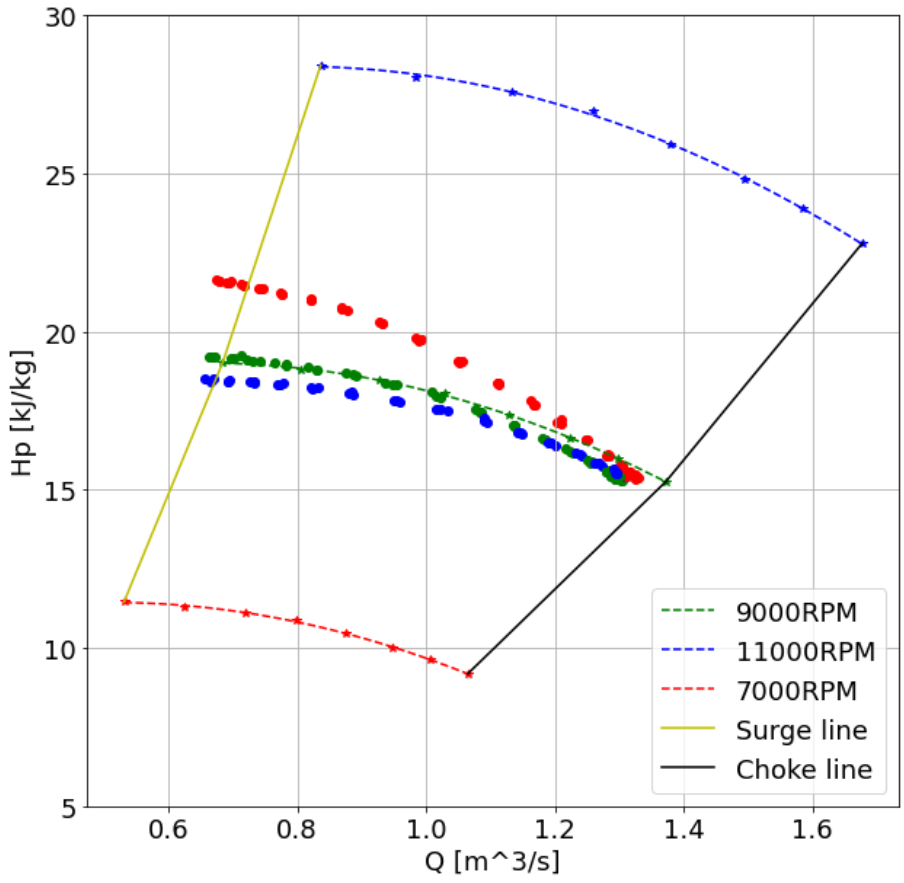

Figure 28: TTS points at the same starting operating point plotted in the compressor map. All repetitions of the profile test are included.

The first method used to define the surge point was utilizing a SL defined in the thermally stable tests. Figure 29 shows the trajectory to surge for each test repetition, with a fixed black vertical line at the volumetric flow rate value extracted from the normal curve characteristic extracted from Case 1. The TTS value is also shown for each of these trajectories. From these plots, a clear trend appears - the steeper curve with the larger HRTS consistently shows a higher TTS value when compared to the other curves. There is a less notable difference between the normal and steep curve characteristics, but the trend also continues here. The two curve steepnesses in round two have the same TTS, but for round 3, the normal curve has a longer TTS.

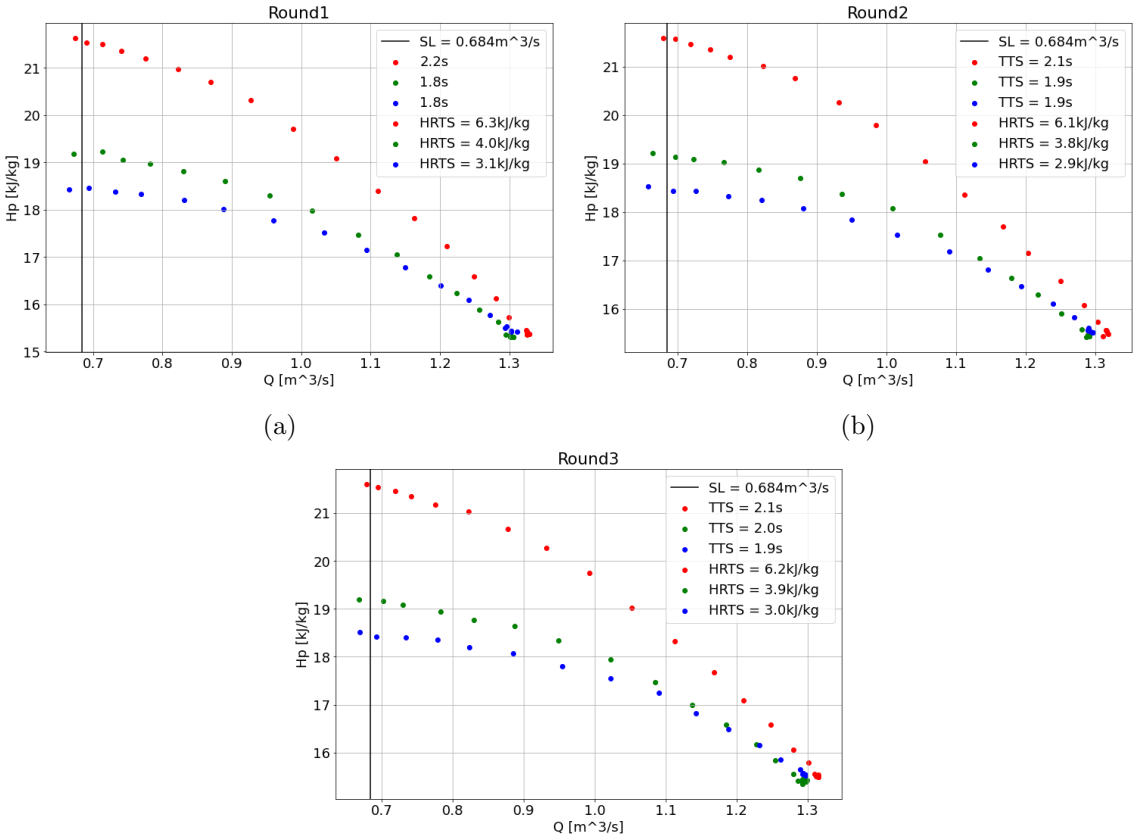

Figure 29: TTS at the same starting operating point, using a SL of 0.684 m3/s.

HRTS is, in this case, defined as the difference in polytropic head between the TTS initiation point and the polytropic head when the operating point has crossed the SL. The difference in HRTS is consistent between all three curves for the different test rounds, where the distance between normal and steep curves are at 2.3 kJ/kg and 0.9 kJ/kg between the flat curve and the normal curve. The large discrepancy in difference in HRTS to the normal curve, for the steep curve and the flat curve, can, to some extent, be described by the prewhirl angle of the steep curve having double the offset compared to the flat curve. The curves show a clear correlation between HRTS and TTS - where a higher HRTS results in a slower TTS.

The second method in defining the onset of surge for the transient tests was done by

looking at the gradient of the characteristic curves and setting a SL where the curve gradient started to either flatten or move towards a negative value when moving left in the compressor map. This definition was difficult to decide, as there may be minor individual fluctuations in polytropic heads, which may be caused by uncertainties due to the transient nature of the testing conditions rather than the actual onset of surge. As such, a volumetric flow value was chosen in an area where the gradient of the trajectories seemed to shift for several rounds and curves. This value was chosen as 0.65 m^3/s, and a new SL was placed at this position.

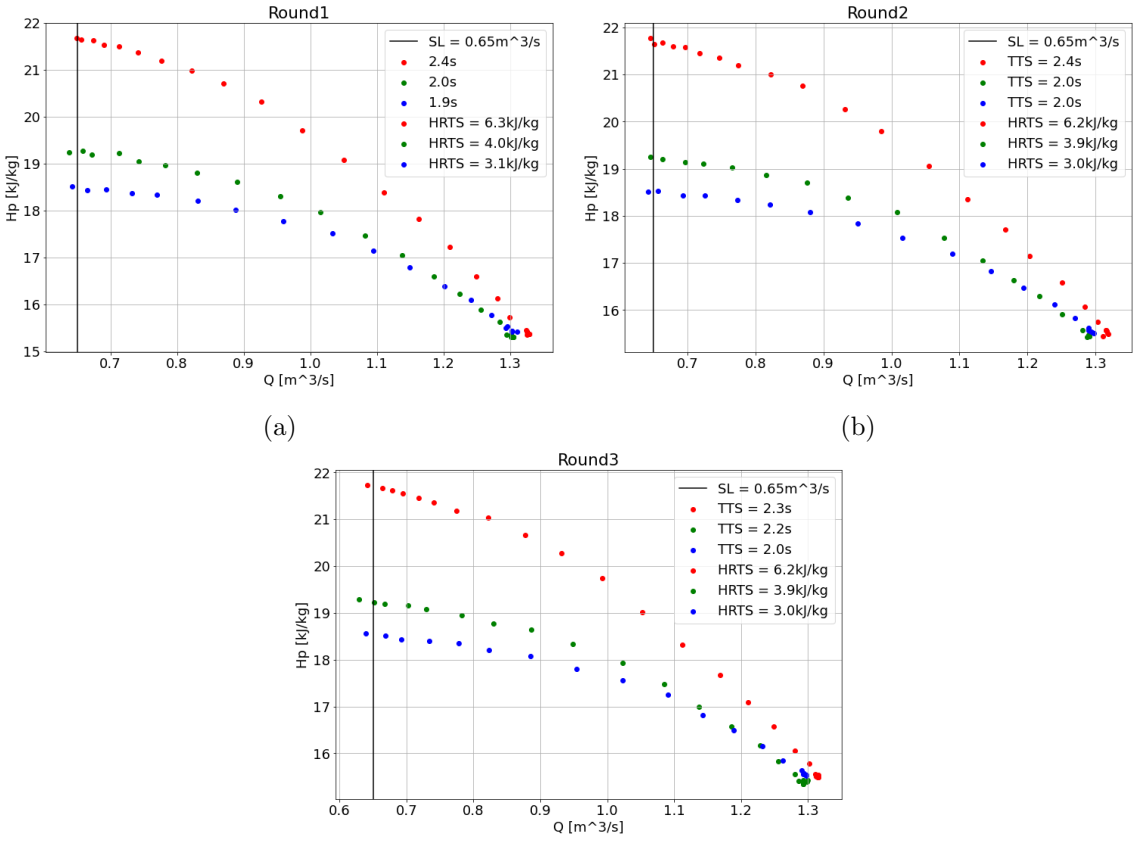

Figure 30: TTS at the same starting operating point, using a SL of 0.65 m^3/s.

Figure 30 shows the new trajectories to surge when using an updated SL value. One notable observation from these plots is that the difference in HRTS between the different curve steepness remains unchanged from the ones with the original SL. Naturally, the TTS has increased for all trajectories in all cases. The difference in TTS between the cases is also notably changed, where the steep trajectories see a more considerable difference than the others for most rounds. The most notable difference, however, is between the normal and flat trajectories. The difference in TTS is now 0.1 seconds slower for round 1 and round 3 but remains the same for round 2. There is now an apparent discrepancy between the flat and normal characteristics, where the average difference of all rounds is 0.1 seconds. This highlights HRTS's impact on TTS, where the higher the HRTS - the longer the TTS is.

As described in section 4.4, some uncertainty is connected to the volumetric flow calculations at lower flow conditions. Due to this uncertainty of flow calculation around the SL, a third method has been utilized: FFT analysis of pressure at the impeller outlet. Figure 31 shows FFT plots in the time, frequency, and magnitude specter. The frequency is shown in 10-6000 Hz; the minimum frequency of 10 Hz is set to remove unwanted noise in the low-frequency specter. These plots are defined as waterfall plots and will be referred to as such going forward. The figures show the whole testing period done in Case 2, showing clear progression towards surge before rapidly reducing towards zero. As the sensor used is a piezoelectric sensor, it is assumed that the zero-value areas occur when the pressure oscillations from the onset of surge are no longer sufficient to counteract the loss of pressure from the volumetric flow.

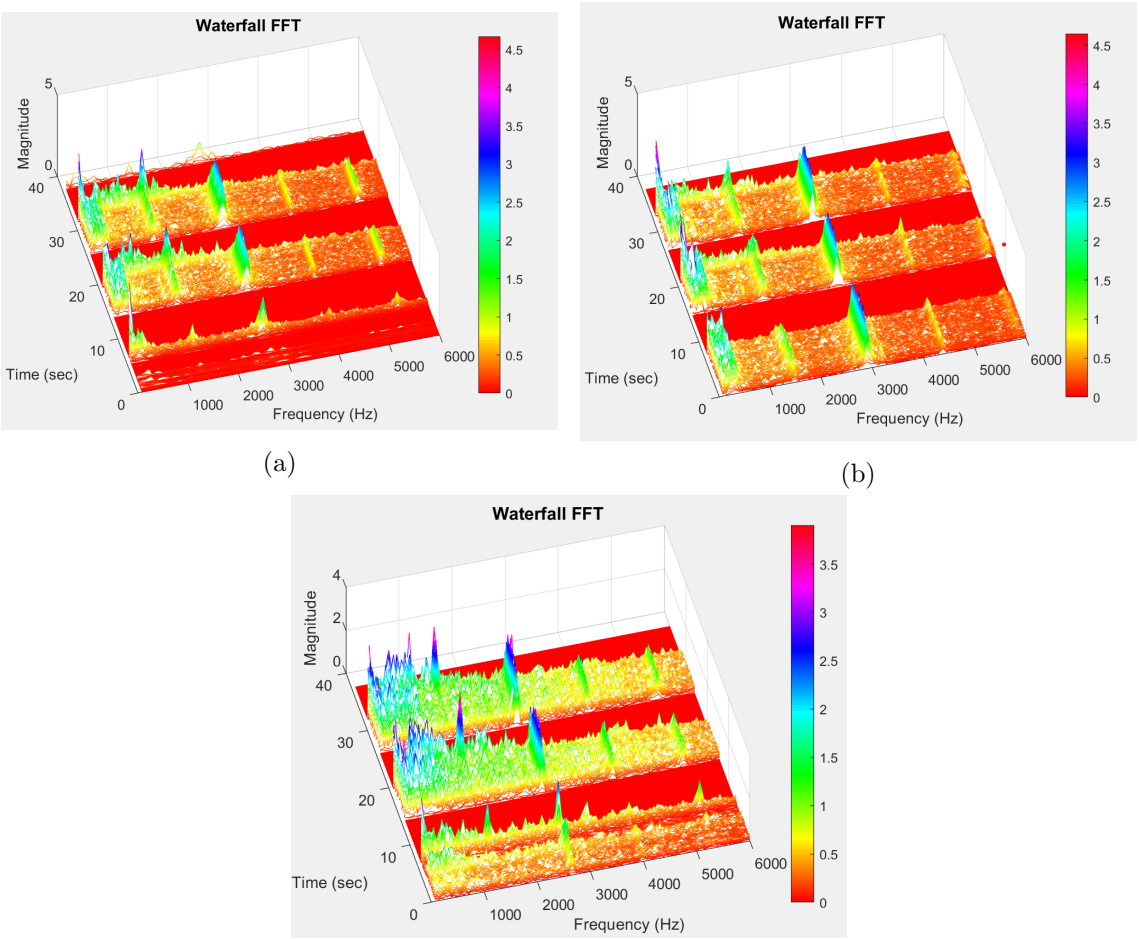

(a) (b)

(c)

Figure 31: Waterfall from 10-6000 Hz for all curve characteristics in Case 2 in the whole time domain.

From Figure 31a, it is clear to see that there is some uncertainty in the pressure measurements of the first rounds; this is also evident in 31c. As such, a decision has been made to only use waterfall values from round 2 and round 3 for all TTS cases. See Appendix B for the additional figures from the first rounds. However, an apparent increase in magnitude when moving toward surge can be seen around the area from 500-2000 Hz. It was there-

fore decided that this area was to be looked at more closely when looking at the waterfall diagrams in the TTS time domain defined in the volumetric flow methods.

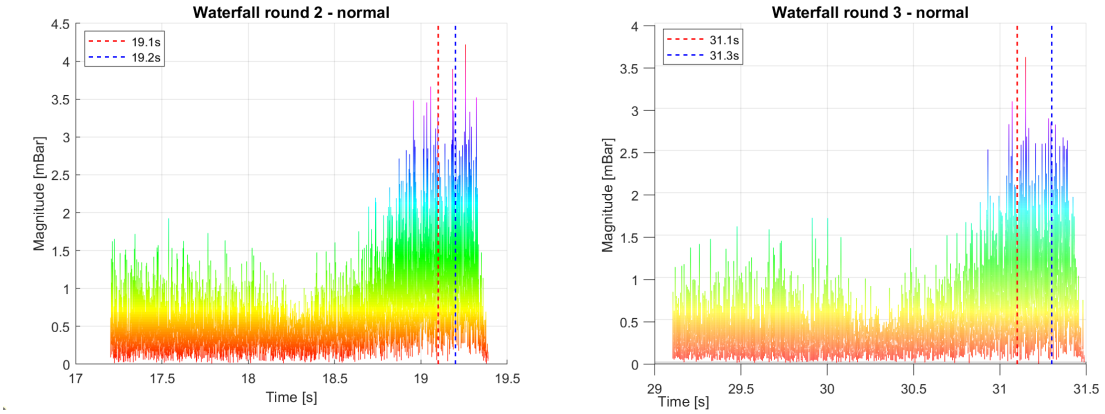

(a) (b)

Figure 32: Waterfall of the path to surge in the time and frequency domain for normal curve characteristics, in round 2 and 3.

Figure 32 shows the FFT in the time and magnitude regions in the path towards surge for the normal curve. The starting time is 17.2 s for round 2 and 29.1 s for round 3. The point at which surge occurs should be at either 19.1 s or 19.2 s for round 2 and 31.1 s or 31.3 s for round 3, depending on which SL is used. Both plots show a somewhat constant magnitude value, moving towards the right in the graph, before a sudden slight decrease, leading to a sharp increase in magnitude as the operating point moves toward surge. Both SL methods seem to match well with the increase in magnitude.

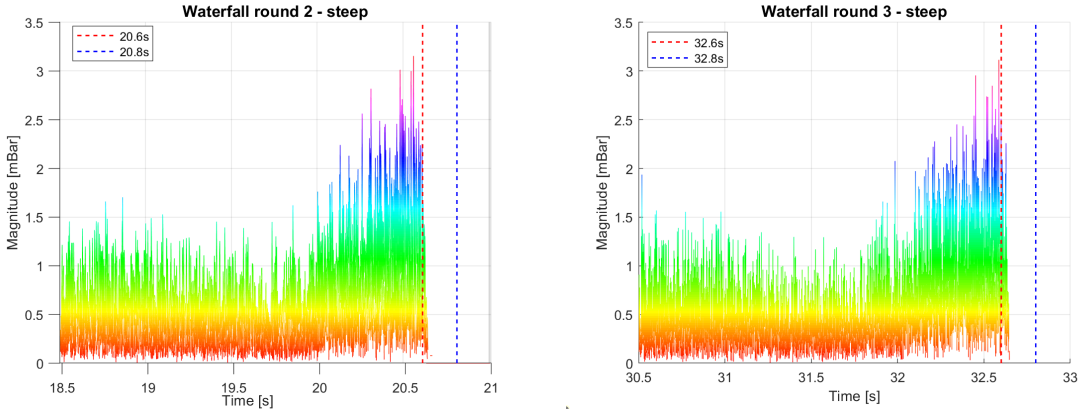

(a) (b)

Figure 33: Waterfall in the time and frequency domain of the path to surge for steep curve characteristics, in round 2 and 3.

Assessing SL through FFT plots becomes more challenging with a steep curve due to its early cutoff and lower magnitude than other curve characteristics. For example, as section 2.3 states, enhancing flow stability into the compressor via a positive prewhirl angle can

delay surge onset and mitigate its severity.

It is unknown why the magnitude cuts to zero before the onset of surge, as there may be several reasons. When the volumetric flow decreases significantly, it escalates pressure fluctuations, potentially triggering system instability if the oscillation amplitude is not large enough to counterbalance the pressure loss. Tests with smaller oscillation magnitudes may reach their limits earlier because of these dynamics. When there is a higher headrise to surge, the system is more resistant to flow reversal and pressure fluctuations, which could result in lower frequency oscillations predominating. This could lead to a more limited frequency content in the FFT, causing an earlier cutoff than other tests. There may also be a connection between the increase in rotational velocity and the early cut-off.

Although these premature cutoffs affect the measurement of surge onset in steep characteristic test for Case 2, specific observations emerge. In both plots 33a and 33b, there is a distinct magnitude increase as the time progresses towards the cutoff point. This trend suggests possible surge onset or the operating point nearing the surge point. The cutoff point aligns well with the original SL's surge point. However, it remains unclear from these results whether surge has occurred at this point or if one should anticipate more significant pressure fluctuations at the SL point based on the curves' gradient. As seen in section 3.1, the sensor's sensitivity is 0.14 mBar. To refine this analysis, employing a sensor more sensitive to minute pressure fluctuations could be advisable, enabling precise capture of these low-flow fluctuations.

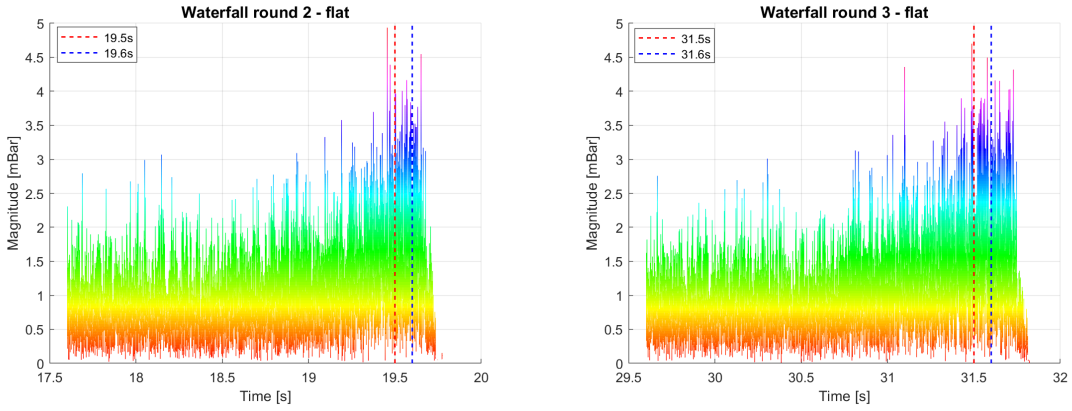

(a) (b)

Figure 34: Waterfall of the path to surge in the time and frequency domain for flat curve characteristics, in round 2 and 3.

Figure 34 shows the FFT of the path towards the two SLs for the flat characteristic. As seen from the figure, the magnitude does not cut to zero, as happens for the steep characteristic. Another notable difference is the significant increase in magnitude compared to the two other curve characteristics. The flat characteristic plots reach a maximum magnitude of 4.5 mBar and 5 mBar, compared to a maximum of a little over 3 mBar and almost 4 mBar for the normal characteristic and 3 mBar for both time intervals of the steep characteristic. This significant increase in magnitude may indicate a more profound surge than the two

others, where the steep curve experiences the least severe surge conditions in the measured period.

The plots in Figure 34a and 34b show a good correlation with the expected timeframe from the SL plots. There is a significant magnitude of oscillation at both 19.5-19.6s and at 31.5-31.6s. This further backs up the SL's set from Case 1 and the one set from the change in curve gradient.

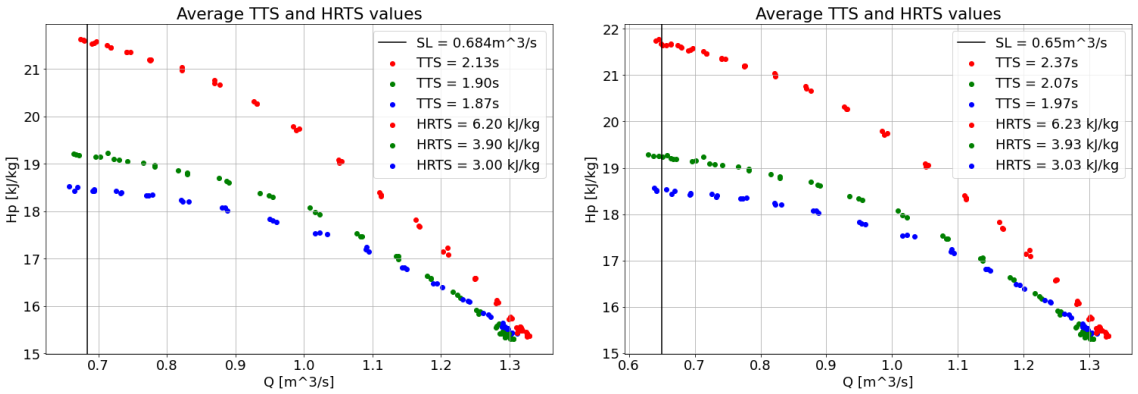

(a) (b)

Figure 35: Average TTS at the same starting operating point, using a SL value of 0.684 m^3/s (35a), and 0.65 m^3/s (35b).

Figure 35 displays the mean values of TTS and HRTS at two SL measures of 0.684 m^3/s and 0.65 m^3/s. Both plots reveal an apparent trend in which the steep characteristic demonstrates a markedly slower TTS compared to the normal and flat characteristics. Nonetheless, there is no apparent disparity between the normal and flat curves at a SL of $0.684m^3/s$.

Upon moving the SL to $0.65m^3/s$, the variation in TTS becomes more distinct, with the normal curve exhibiting a TTS slower by 0.1 seconds than that of the flat curve. This variation among the curves is also mirrored in the HRTS values, whereby a higher HRTS typically correlates with a slower TTS.

5.4 Case 3: TTS - Same Rotational Velocity

TTS has been tested using a constant rotational velocity of 9000 RPM for all curve characteristics, as outlined in 4.2.3. TTS has been tested three times from a starting condition of 80% opening of the ASCV. The case aims to assess how the different curve characteristics impact TTS at the same rotational velocity and ASCV opening but at different starting operating points.

Figure 36 shows the three surge paths plotted against the compressor map found in section 5.1. The different surge paths follow each other closely within each curve characteristic, implying a good correlation.

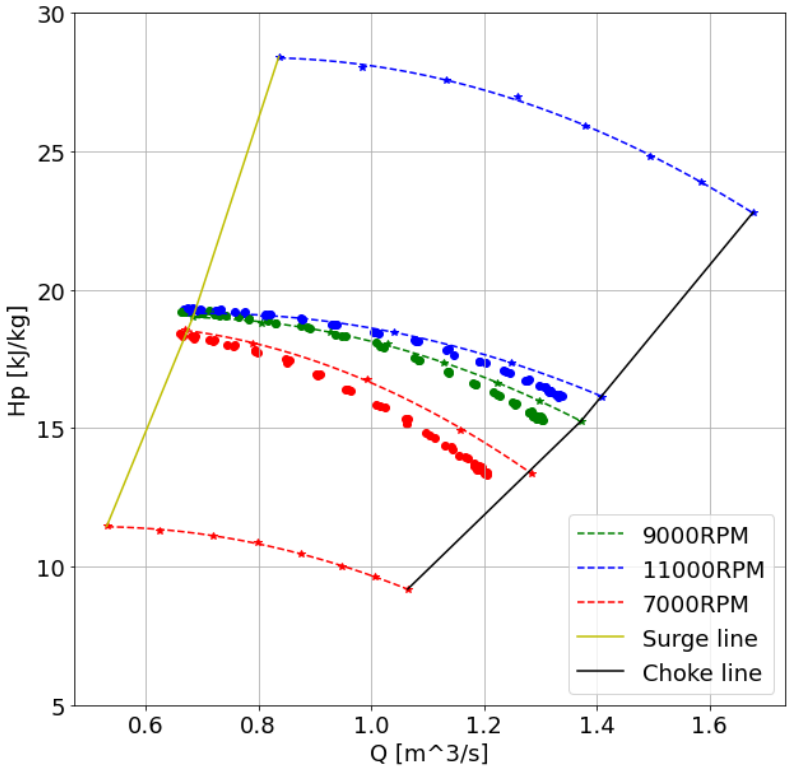

Figure 36: TTS points at the same rotational velocity plotted in the compressor map. All repetitions of the profile test are included.

Figure 37 shows the TTS plots for Case 3, using the SL defined in Case 1. While the operating conditions for the different characteristics are equal in terms of rotational velocity and ASCV opening, there is a drastic change in the position of the initial operating point - both in volumetric flow and polytropic head. The steeper curve is now considerably closer to the SL, while the flatter curve is further from the SL. A clear shift in HRTS has also emerged for the different curves. The HRTS of the steeper curve has shifted from 6.2-6.3 for Case 1 to 4.8-5.1, while the normal and flatter curves remain at similar values.

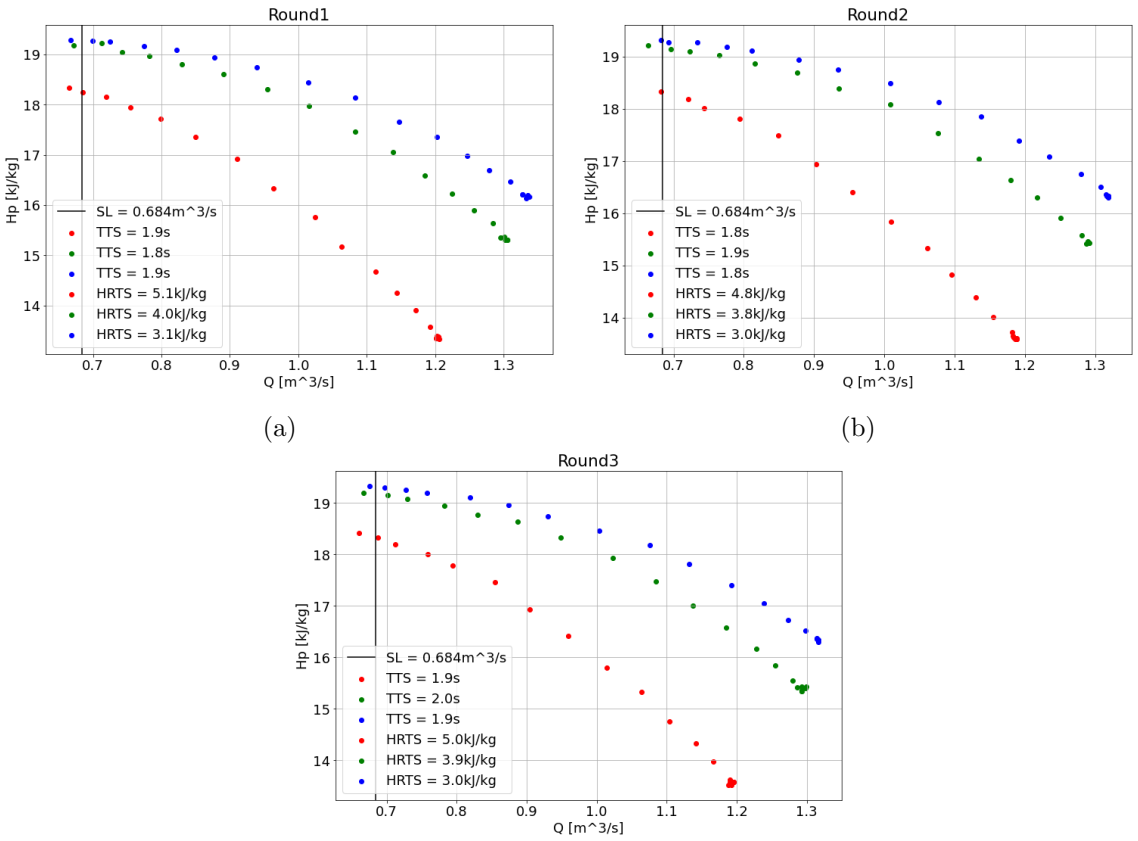

Figure 37: TTS at the same rotational velocity, using a SL of 0.684 m^3/s.

The shift towards lower values in both volumetric flow, polytropic head, and HRTS for the steeper curve would suggest some noticeable changes in TTS. TTS for the steep curve in Figure 29 is between 2.1-2.2s, while for Case 3, the values lie between 1.8-1.9s - a significant shift towards faster TTS. There is no noticeable fundamental shift for the normal and flatter curves, as they lie in the same TTS timeframes. Comparing the different TTS values in Figure 37 to each other, there is no noticeable difference between the different characteristics. There is a maximum of 0.1 seconds between the fastest and slowest TTS values, and it shifts which of the characteristics is fastest and slowest.

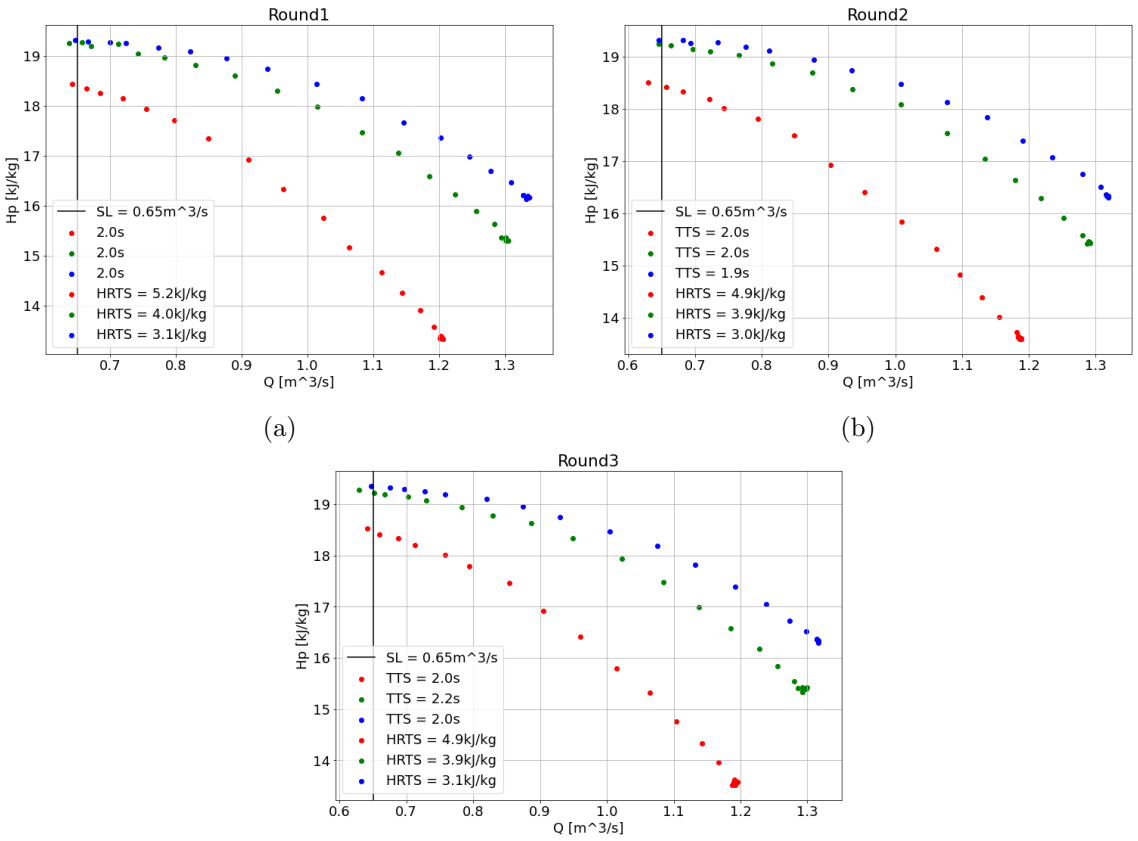

Figure 38: TTS at the same rotational velocity, using a SL of 0.65 m^3/s.

Figure 38 shows the TTS plots for Case 3, this time using the SL defined from the curve gradient in Case 2. However, there are still no noticeable differences in TTS between the different curve characteristics in rounds 1 and 2. For these rounds, the TTS is almost identical for all characteristics, bar a 0.1 second quicker time for the flatter curve in round 2. In round 3, the TTS for the normal curve increases by 0.1 seconds compared to the other two, giving it a 0.2 seconds slower TTS than both curves. Here is, however, no overall noticeable trend differentiating the varying curves, as they consistently fall within the identical TTS time spectra.

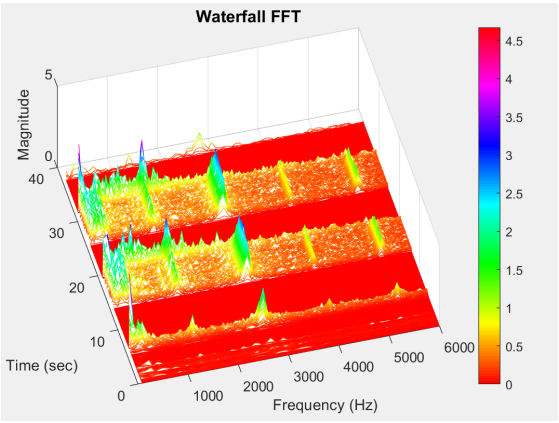

(a)

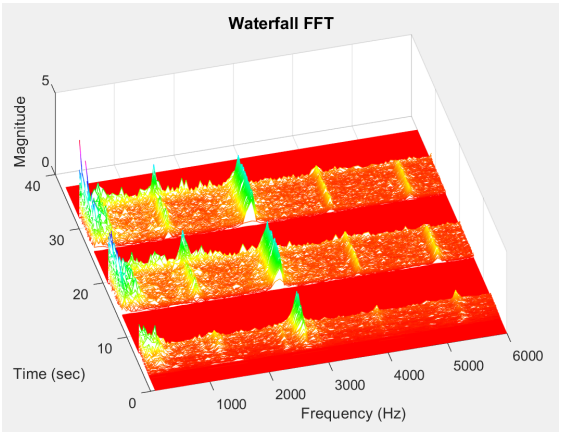

(b)

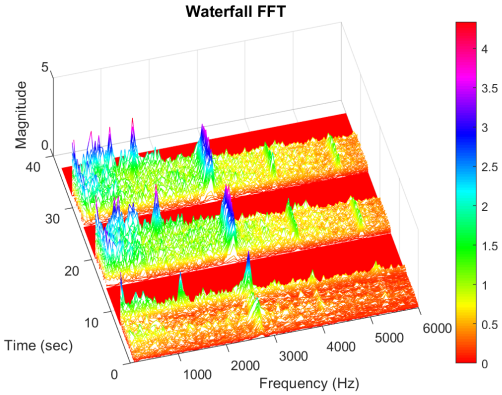

(c)

Figure 39: Waterfall from 10-6000 Hz for all curve characteristics in Case 3 in the whole time domain.

Figure 39 shows the waterfall plots of the three curve characteristics in the whole time domain at a frequency of 10-6000 Hz. The same effects as in Figure 31 are seen, with a clear progression in magnitude towards surge before it rapidly reduces towards zero.

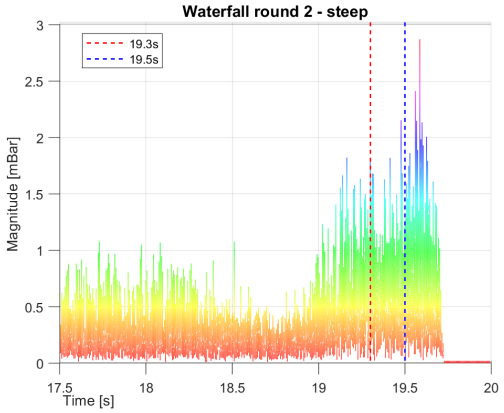

(a)

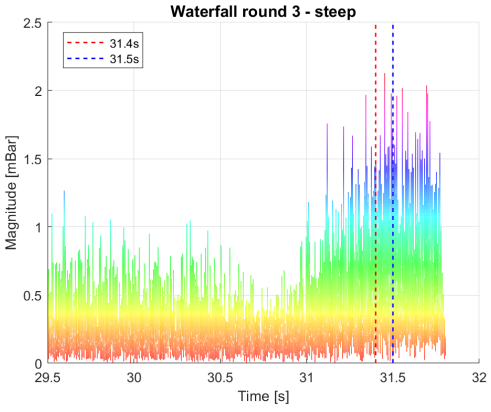

(b)

Figure 40: Waterfall in the time and frequency domain of the path to surge for steep curve characteristics.

Figure 40 displays the FFT progression towards the two SLs for the steep characteristic in Case 3. Interestingly, unlike the steep characteristic in Case 2, the magnitude does not drop to zero earlier than expected. The cause for this difference, particularly the absence of an early cut-off for the steep characteristic at 9000 RPM compared to 9700 RPM, is currently unclear. Further investigation into the role of FFT in surge detection in future research with the existing sensor setup may be needed. Both plots show a clear increase in magnitude as surge approaches and achieve similar levels of magnitude to the steep characteristics from Case 2. For figure 40a there is a clear magnitude top to the right of the onset of surge for the SL at 0.65 m^3/s. This may suggest that the onset of surge is yet to happen.

The FFT path to surge for the regular characteristic is not presented since it uses the same dataset as Case 2. Likewise, the flat characteristic will not be emphasized but included in Appendix B because it closely resembles the data from Case 2. This is due to the similar initial operating conditions of the flat characteristics across the two cases, unlike the steep ones.

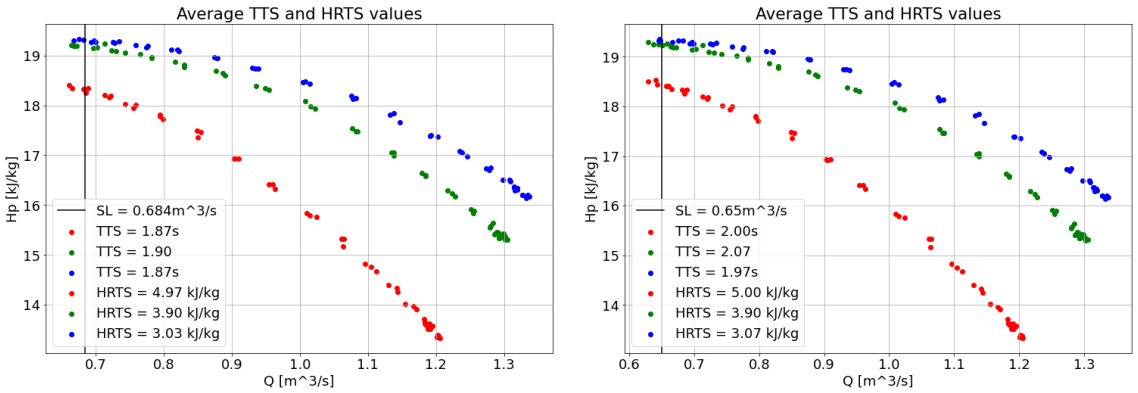

(a) (b)

Figure 41: Average TTS at the same rotational velocity and ASCV opening, using a SL value of 0.684 m^3/s (41a), and 0.65 m^3/s (41b).

Figure 41 displays the mean values of TTS and HRTS at two SLs, 0.684 m^3/s and 0.65 m^3/s. The normal characteristic has the longest TTS, but the variation among characteristics is slight. Therefore, no solid trend suggesting a longer TTS for the normal characteristic is discernible. An evident pattern can be observed: a specific rotational speed and ASCV opening, across the different curve characteristics, yield equivalent TTS values. It is deduced that this is due to the HRTS differences balancing out the volumetric flow rate differences in relation to the distance to the SL.

5.5 Case 4: Trip Scenario

Case 4 involved analyzing TTS and TIS for a trip scenario for varying curve characteristics using the same starting operating point in the compressor map. The method used has been outlined in section 4.2.4. The case aims to asses how the different curve characteristics

impact TTS and TIS during a trip scenario.

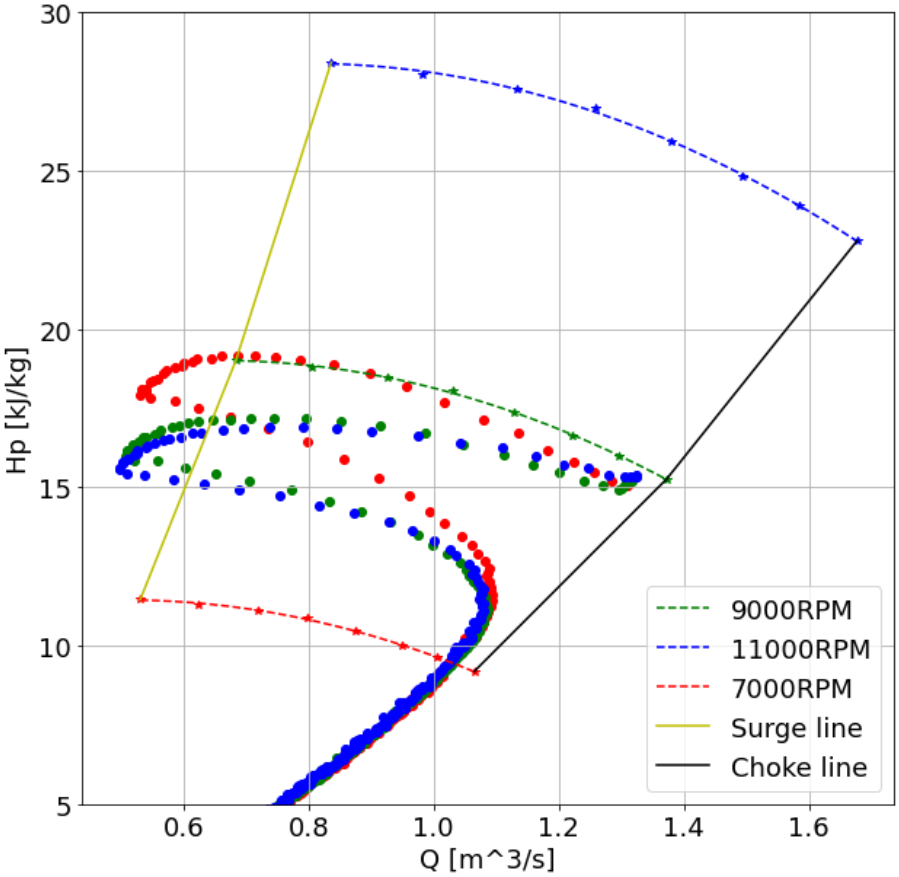

Figure 42: Trip scenario plotted in the compressor map.

Figure 42 shows the trip scenario for all the different curve characteristics. The curves follow the results obtained in Case 2: the steep curve has the highest HRTS, and the flat has the lowest HRTS. There are, however, some apparent differences in their paths toward surge, where all curves in the trip case fall below the initial operating point. After the initial drop in the polytropic head, there is a recovery phase, where all curves recover to a point above the initial operating point. The recovery is most significant in the steep curve, which has a headrise above the static compressor line at 9000 RPM found in Case 1.

After the onset of the surge, the operating point moves deeper into surge while dropping in polytropic head. Here the flat and normal curves achieve a relatively similar degree of surge, with the flat one moving the furthest into surge. The steep curve has a noticeably higher minimum volumetric flow rate, thus never achieving as high a degree of surge as the other two curves. After moving to the right of the SL, the operating point moves toward higher flow until it achieves the initial ASCV opening. Finally, the operating point follows the trip line toward lower polytropic head and volumetric flow.

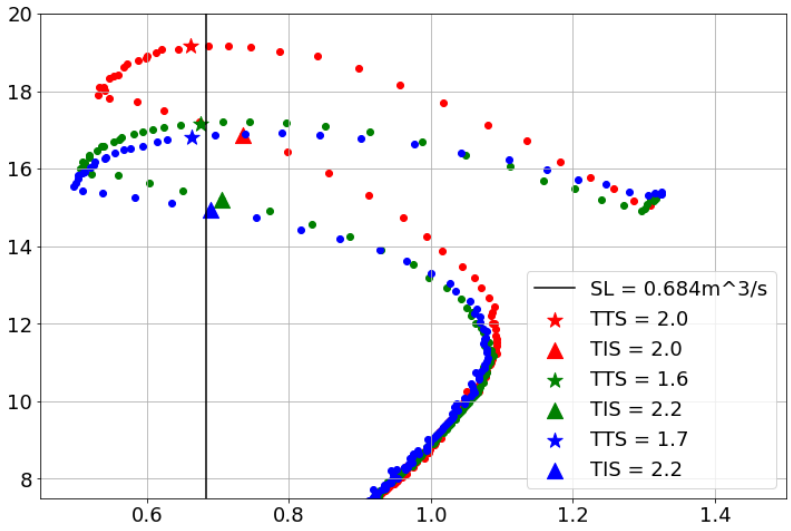

Figure 43: TTS and TIS for trip scenario, using a SL of $0.684 m^3/s$

Figure 43 shows the trip scenario and the points at which the compressor reaches surge and exits surge. The SL is gathered from the static condition experiments outlined in Case 1. A star point defines the points describing the onset of surge, while the exit from surge is shown as triangles. Looking at the TTS values for the different curves, one can observe similar tendencies as in Case 2, in that the steeper curve has the slower TTS of the three. There is less difference in the maximum polytropic head for the normal and the flat curve than in Figure 29. To some degree, this effect may be described by the more considerable drop in polytropic head the normal curve experiences right after the initial operating point. This may be caused by a less synchronized activation of the impeller trip and the ramp, outlined in section 4.2.4. This may be why the TTS is 0.1 seconds slower for the normal curve than the flat one, although the normal curve should have a higher HRTS than the flat curve.

TIS has also been outlined in Figure 43. TIS is an important parameter to evaluate for compressor systems, as a longer time in surge conditions may cause further damage to the compressor. Here the steeper curve is shown to operate for a shorter time in surge conditions than the others. The normal and flat curves have the same TIS values.

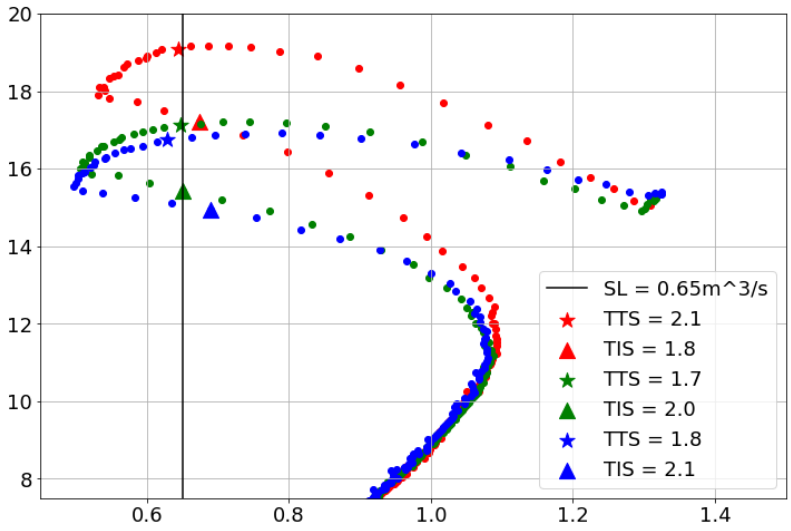

Figure 44: TTS and TIS for trip scenario, using a SL of $0.65m^3/s$

Figure 44 shows the trip scenario with a SL placed at $0.65m^3/s$, as described in section 5.3. Here the TTS increases with 0.1 seconds for all curves, resulting in no change in TTS between the curves. TIS decreases by 0.2 seconds for the steeper and normal curves and increases by 0.1 seconds for the flatter curve. For these conditions, there is a clear trend: the TIS decreases with an increasing HRTS or steepness of the characteristic curve. While the TTS remains slowest for the steepest curve characteristic, underlining the connection between HRTS, TTS, and TIS.

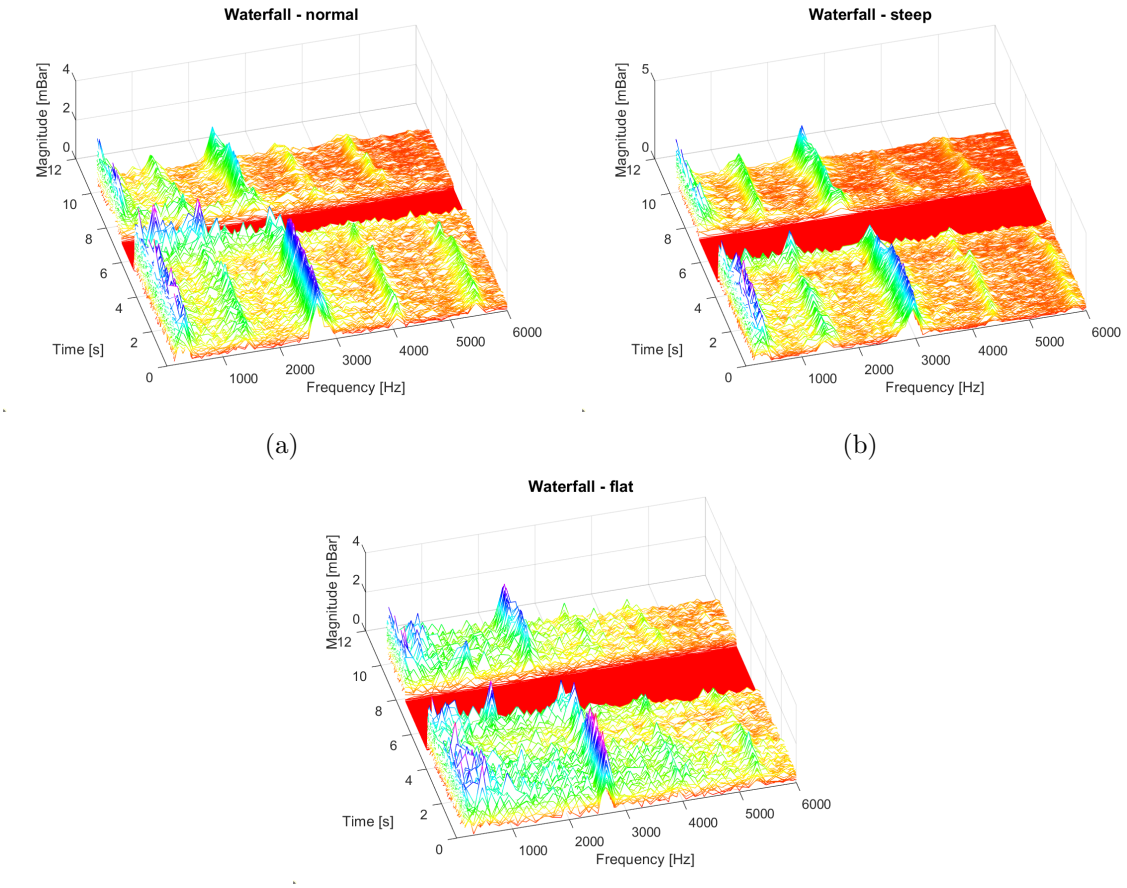

(a) (b)

(c)

Figure 45: Waterfall of all trip scenarios, in frequency spectre of 10-6000 Hz

Figure 45 shows the waterfall of the three trip scenarios in the time, frequency, and magnitude domain. The frequency is set from 10-6000 Hz, and the time domain is set as the whole time domain of the trip scenario. There is a distinct increase in magnitude when the flow moves toward surge. There is also a clear trend for all three plots: the blade passing frequencies move toward lower frequencies as time increases. This is due to the rotational velocity of the impeller decreasing more as the trip scenario continues.

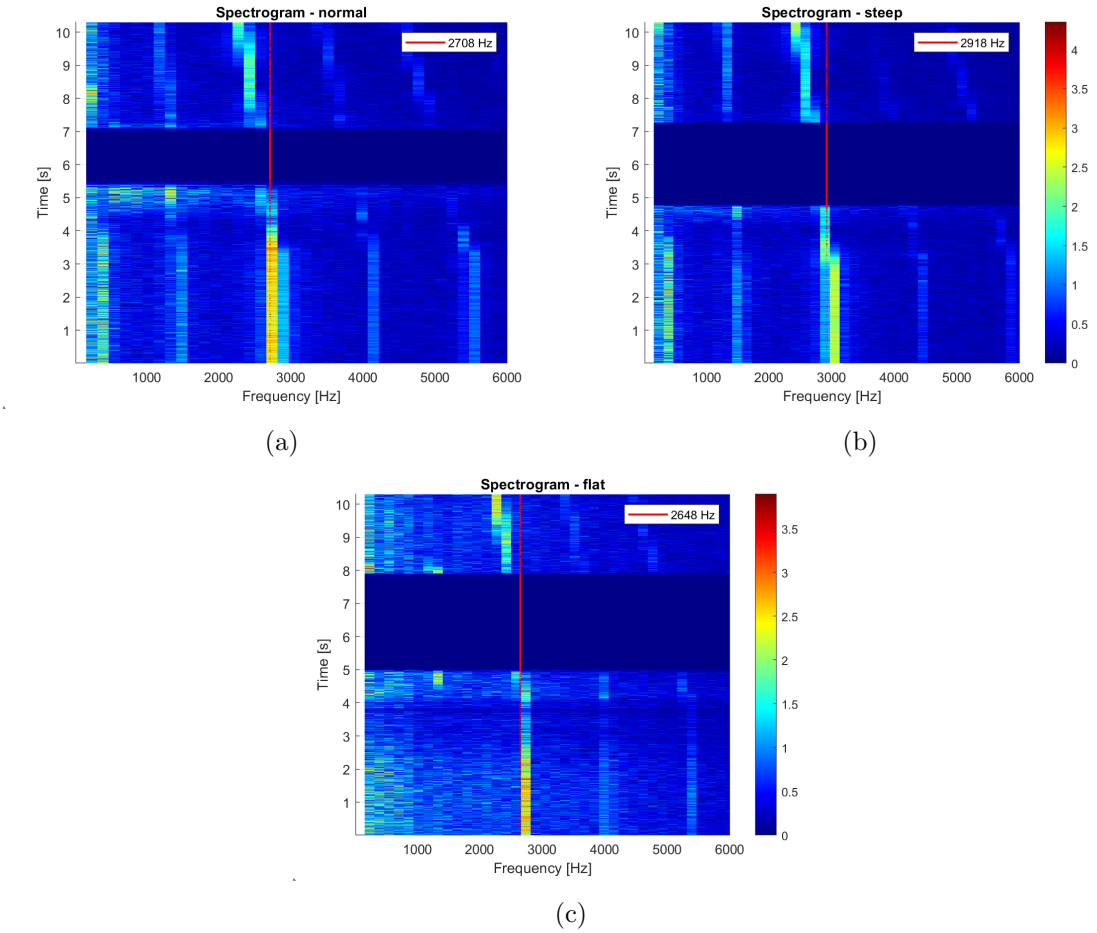

Figure 46: Spectogram of all trip scenarios, in frequency spectre of 10-6000 Hz

Figure 46 shows the spectrograms of the different curve characteristics during the trip scenarios. BPF for the different characteristics is calculated using equation 22, calculating for 18 blades, and the rotational velocity given in section 4.2.4. The red vertical line in the plots signifies the BPF at the starting conditions for each characteristic. As the operating point moves further into the trip scenario, the amplitude signifying the BPF moves toward a lower frequency. The plots show that the BPF moves furthest to the left of the vertical line for the steep, second furthest for the normal line, and least to the left for the flat characteristic. This is likely because of the initial higher rotational velocity for the steeper and normal curve characteristic.

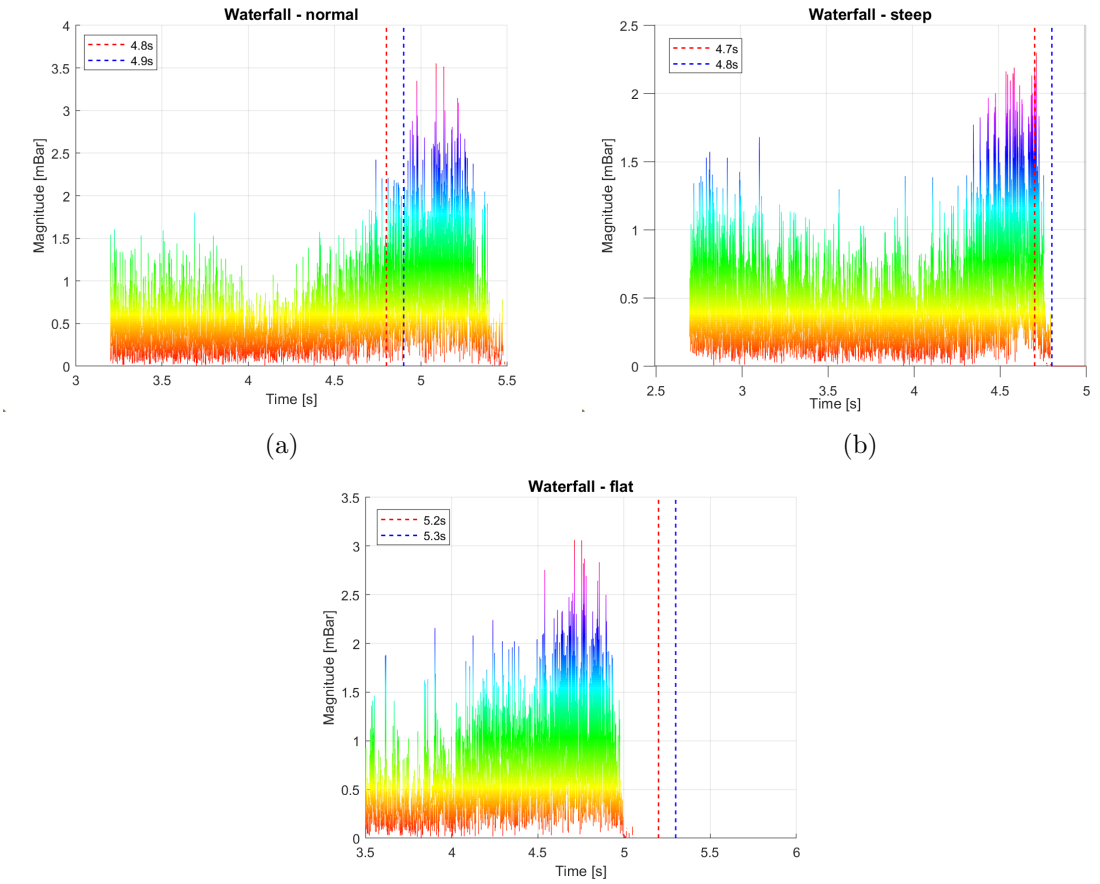

(a) (b)

(c)

Figure 47: Waterfall of all trip scenarios, in the time and magnitude domain. Frequency spectre of 500-2000 Hz.

Figure 47 shows the waterfall plots of the trip scenario from the initiation of the TTS scenario in the time and magnitude specters. There are some significant changes from the equivalent figures in Case 2. The maximum magnitude has changed for all three characteristics, from around 4 mBar to 3.5 mBar for the normal, around 3 mBar to 2 mBar for the steep, and from almost 5 mBar to 3 mBar for the flat curve. There is also a change in the cut-off point for the different plots compared to where the operating point crosses the SLs. For the normal curve, the cut-off line has now shifted further to the right of the surge points; for the steep curve, it remains relatively close to the same, while for the flat curve, the cut-off point has moved far to the left. The earlier cut-off for the flat characteristic leaves little possibility for interpretation of the path toward surge in the frequency analysis.

6 Conclusion and Further Work

This research focused on generating experimental data that would support the development of a DT model for the gas compression testing facility at NTNU. A diverse dataset was created by conducting both static and transient tests.

Under thermally stable conditions, a detailed compressor map was developed. This tool is fundamental for creating accurate and reliable DT models, as it establishes a connection between the physical system and its digital counterpart. Deviations were observed between transient and thermally stable curves. This highlighted the inherent complexity and dynamic nature of centrifugal compressors and underlined the value of a dual-testing approach in capturing a fuller picture of compressor behavior. The transient tests provided valuable data, facilitating an investigation into the TTS and HRTS under different operational scenarios. It is clear from the results that further use of dynamic tests in this research area can contribute to our understanding of the real-world operational mechanics of compressors.

DT technology, thanks to its ability to offer detailed machine monitoring and predictive maintenance, has become an industry staple. The unique set of results derived from the transient tests in this study represents a resource for machine learning algorithms. This data is anticipated to enhance the accuracy of the future DT model at the NTNU compressor test lab, which aims to fortify DT's integral role within the industry.

One of the key findings from the transient tests was the relationship between HRTS and TTS. A longer TTS provides a more considerable safety margin before the onset of potentially damaging surge conditions, a critical consideration for operational safety. In situations where operational conditions were identical, other than the curve steepness, there were notable differences in the initial operating points across the curve characteristics. Despite these differences, TTS was similar across the curve characteristics. This indicates that a higher HRTS can help maintain a similar TTS, even when the operating point is closer to the surge line, effectively broadening the safety margin. Contrastingly, when the initial operating point was constant, TTS had substantial differences, where a higher HRTS implied a slower TTS. This highlights the importance of the initial operating point and HRTS in defining TTS.

Frequency analysis of the data from the transient tests yielded further insights. For example, waterfall plots showed a significant increase in magnitude as the system approached the surge point, serving as a potential early warning sign of surge onset. Finally, the research found that a higher HRTS led to a shorter TIS. This suggests that a higher HRTS could reduce the risk of damage to the compressor under surge conditions.

6.1 Further work

While this research has provided meaningful strides toward creating a reliable DT model, there is still a considerable journey before achieving the final goal. To make further

progress in refining the digital model towards a more representative DT, the following suggestions are proposed for future development:

- Use the data provided in this thesis to further develop the DT model.
- Use the DT model and the deterioration scenarios from this thesis to predict deteriorated equipment performance impact on capacity and energy efficiency.
- Further investigations into the role of FFT in surge detection, one way could be exploring the implementation of more sensitive dynamic pressure sensors at the impeller outlet for more precise detection of surge onset.
- Further testing of TTS and TIS under varying operating conditions.
- Establishing direct two-way communication between the digital model and the experimental laboratory.
- Establish thermally stable curves at 7000 and 11000 RPM to more accurately represent the total compressor map.

Bibliography

[1] Sander Kynell Arstad. 'Digital Twin - Transient Flow Conditions'. Accepted: 2022-09-13T17:20:01Z. Master thesis. NTNU, 2022.

[2] *AspenTech — Asset Optimization Software - Asset Performance Management, Process Engineering for Chemicals, Energy and Engineering & Construction.* URL: https://www.aspentech.com/en/ (visited on 8th June 2023).

[3] Ronald H. Aungier. *Centrifugal Compressors: A Strategy for Aerodynamic Design and Analysis*. 1st Jan. 2000. DOI: 10.1115/1.800938.

[4] Lars Eirik Bakken. *Thermodynamics, compression and expansion processes, TEP04*. 2022.

[5] Lars Eirik Bakken. *Turbomachinery - Transient Performance and System Response, TEP05*. 2022.

[6] Martin Bakken et al. 'Wet Gas Compressor Modeling and Performance Scaling'. In: ASME Turbo Expo 2019: Turbomachinery Technical Conference and Exposition. American Society of Mechanical Engineers Digital Collection, 5th Nov. 2019. DOI: 10.1115/GT2019-90353.

[7] Veronica Ferrara. 'Wet Gas Compressors - Stability and Range'. Doctoral thesis. NTNU, 2016.

[8] Veronica Ferrara and Lars E. Bakken. 'Wet Gas Compressor Surge Stability'. In: *GT2015-42650* (2015).

[9] P. E. Hedne et al. 'Åsgard Subsea Compression - technology overview and operational experience'. In: 18th International Conference on Multiphase Production Technology. OnePetro, 7th June 2017.

[10] Øyvind Hundseid and Lars E. Bakken. 'Integrated Wet Gas Compressor Test Facility'. In: ASME Turbo Expo 2015: Turbine Technical Conference and Exposition. American Society of Mechanical Engineers Digital Collection, 12th Aug. 2015. DOI: 10.1115/GT2015-43004.

[11] Tom Irvine. *Shock & Vibration Software*. URL: http://www.vibrationdata.com/software.htm (visited on 8th June 2023).

[12] I. Kassens and M. Rautenberg. 'Flow Measurements Behind the Inlet Guide Vane of a Centrifugal Compressor'. In: ASME 1998 International Gas Turbine and Aeroengine Congress and Exhibition. American Society of Mechanical Engineers Digital Collection, 23rd Dec. 2014. DOI: 10.1115/98-GT-086.

[13] Rainer Kurz et al. 'Operation of Centrifugal Compressors in Choke Conditions'. In: 23rd Feb. 2016.

[14] Grant Musgrove, Cyrus Meher-Homji and Dave Moss. 'Chapter 10 - Downstream'. In: *Compression Machinery for Oil and Gas*. Ed. by Klaus Brun and Rainer Kurz. Gulf Professional Publishing, 1st Jan. 2019, pp. 401–425. ISBN: 978-0-12-814683-5. DOI: 10.1016/B978-0-12-814683-5.00010-9.

[15] Alan V. Oppenheim and Ronald W. Schafer. *Discrete-time signal processing*. 3rd ed. Upper Saddle River: Pearson, 2010. 1108 pp. ISBN: 978-0-13-198842-2.

[16] S. Larry Dixon B. Eng Ph.D and Cesare Hall Ph.D. *Fluid Mechanics and Thermodynamics of Turbomachinery*. 7th edition. Amsterdam ; Boston: Butterworth-Heinemann, 13th Nov. 2013. 556 pp. ISBN: 978-0-12-415954-9.

[17] Erlend Rande. 'Condition monitoring - Validation of flowmeters'. Accepted: 2021-10-09T17:22:06Z. Master thesis. NTNU, 2021.

[18] Hannah Ritchie, Max Roser and Pablo Rosado. 'Energy'. In: *Our World in Data* (2022). URL: https://ourworldindata.org/energy (visited on 8th June 2023).

[19] Alessandro Romei, Paolo Gaetani and Giacomo Persico. 'Computational fluid-dynamic investigation of a centrifugal compressor with inlet guide vanes for supercritical carbon dioxide power systems'. In: *Energy* 255 (15th Sept. 2022), p. 124469. ISSN: 0360-5442. DOI: 10.1016/j.energy.2022.124469.

[20] Razvan Rusovici et al. 'Smart actuation of inlet guide vanes for small turbine engine'. In: *Sensors and Smart Structures Technologies for Civil, Mechanical, and Aerospace Systems 2011*. Sensors and Smart Structures Technologies for Civil, Mechanical, and Aerospace Systems 2011. Vol. 7981. SPIE, 15th Apr. 2011, pp. 969–982. DOI: 10.1117/12.881953.

[21] John M. Schultz. 'The Polytropic Analysis of Centrifugal Compressors'. In: *Journal of Engineering for Power* 84.1 (1st Jan. 1962), pp. 69–82. ISSN: 0022-0825. DOI: 10.1115/1.3673381.

[22] European Committee for standardization. *ISO 5167-2:2022*. ISO. URL: https://www.iso.org/standard/79180.html (visited on 8th June 2023).

[23] Alessio Suman et al. 'A Compressor Fouling Review Based on an Historical Survey of ASME Turbo Expo Papers'. In: *Journal of Turbomachinery* 139.41005 (10th Jan. 2017). ISSN: 0889-504X. DOI: 10.1115/1.4035070.

[24] Fei Tao et al. 'Digital twin-driven product design, manufacturing and service with big data'. In: *The International Journal of Advanced Manufacturing Technology* 94.9 (1st Feb. 2018), pp. 3563–3576. ISSN: 1433-3015. DOI: 10.1007/s00170-017-0233-1.

[25] Gisle Tveit, Tor Bjorge and Lars Bakken. 'Impact of Compressor Protection System on Rundown Characteristics'. In: 1st Jan. 2005, pp. 317–325. DOI: 10.1115/GT2005-68436.

[26] Gisle B. Tveit, Lars E. Bakken and Tor Bjorge. 'Compressor Transient Behaviour'. In: ASME Turbo Expo 2004: Power for Land, Sea, and Air. American Society of Mechanical Engineers Digital Collection, 24th Nov. 2008, pp. 813–821. DOI: 10.1115/GT2004-53700.

[27] Gisle B. Tveit, Lars E. Bakken and Tor Njørge. 'Compressor performance impact on rundown characteristics'. In: 2005.

[28] Sigurd Ueland. 'Digital Compressor Modelling'. Accepted: 2021-09-29T16:19:49Z. Master thesis. NTNU, 2021.

[29] Levi B. Vigdal and Lars E. Bakken. ‘Inlet Guide Vane Performance at Dry and Wet Gas Conditions’. In: ASME Turbo Expo 2015: Turbine Technical Conference and Exposition. American Society of Mechanical Engineers Digital Collection, 12th Aug. 2015. DOI: 10.1115/GT2015-43225.

Appendix

A Timeseries of Case 2-4

This section provides the whole time-series from the experimental campaign in Case 2, 3 and 4. All datapoints are plotted as scatterplots, and pressure ratio vs volumetric flow.

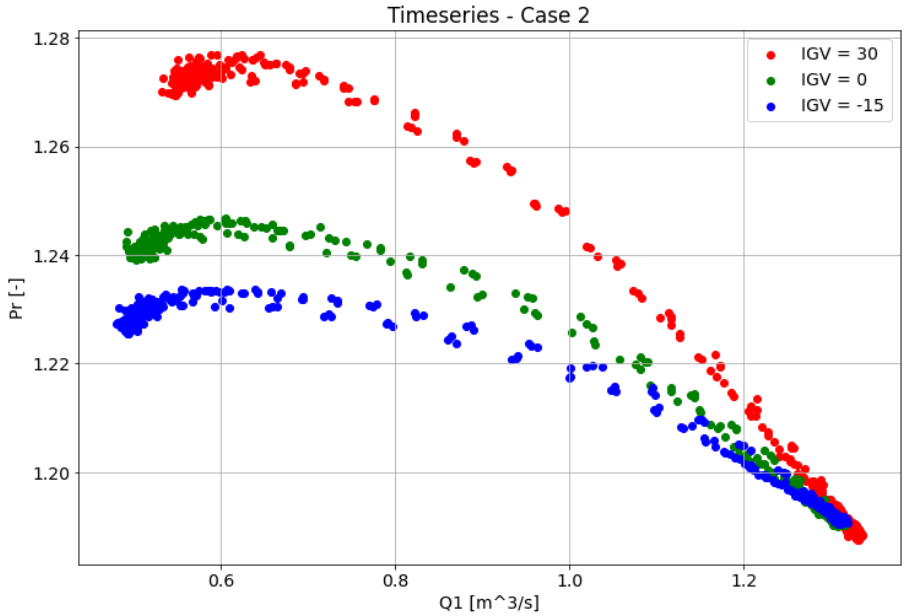

Figure 48: The whole time-series for Case 2. Shown as pressure ratio plotted against volumetric flow.

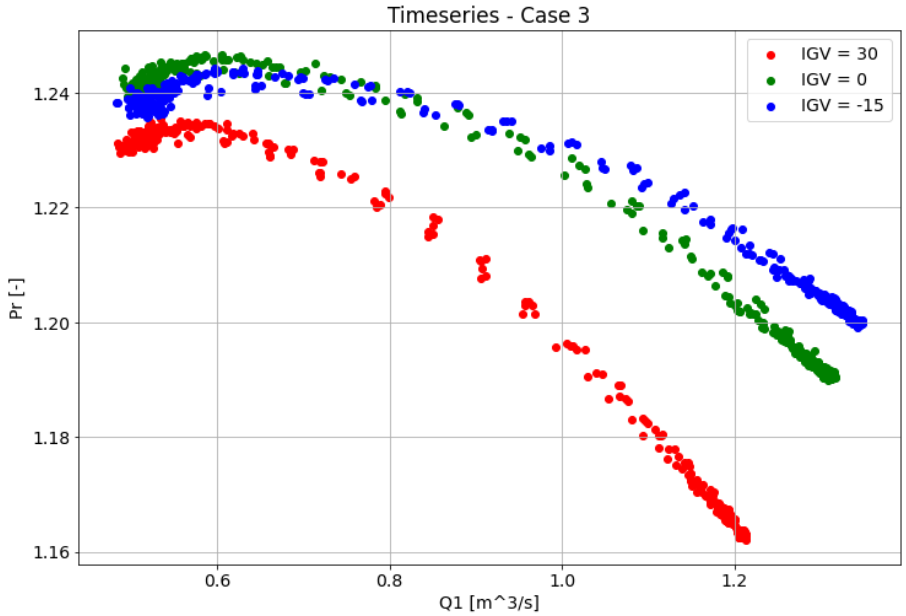

Figure 49: The whole time-series for Case 3. Shown as pressure ratio plotted against volumetric flow.

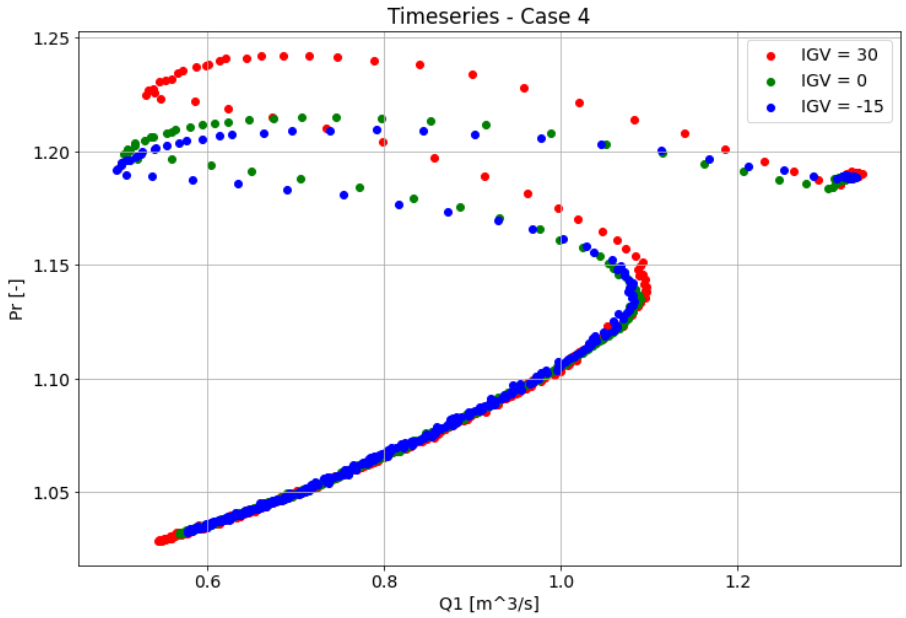

Figure 50: The whole time-series for Case 4. Shown as pressure ratio plotted against volumetric flow.

B FFT and Waterfall

This section provides the waterfall plots in the 500-2000 Hz frequency specter, in the time and magnitude domain not included in the main thesis. This includes the plots for the flat characteristics from Case 3, and the round 1 plot from Case 2.

B.1 Case 2

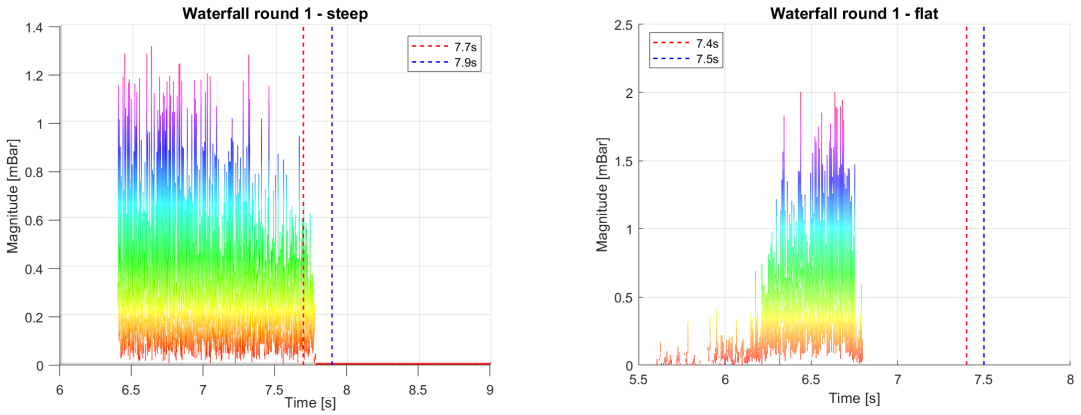

(a) (b)

Figure 51: Waterfall in the time and frequency domain of the path to surge for the flat and steep characteristics in Case 2, for round 1. Normal characteristic is the same as for case 3.

B.2 Case 3

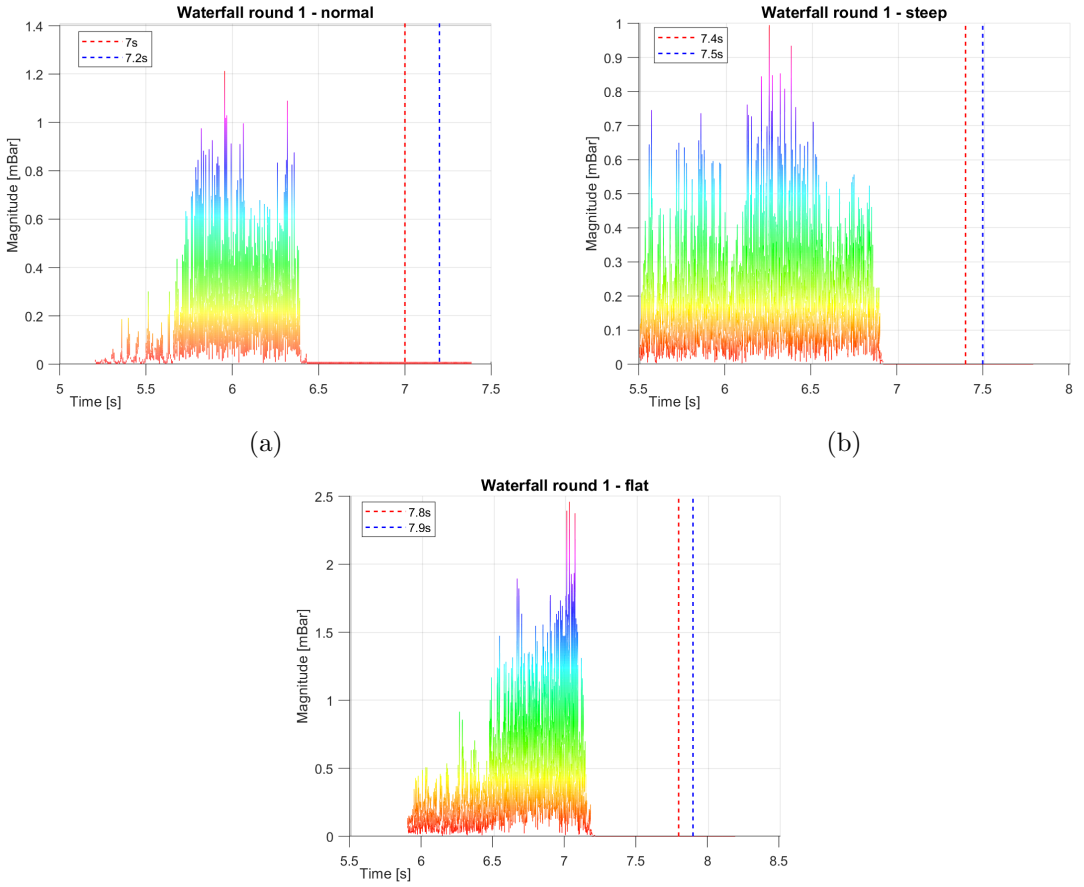

(a) (b)

(c)

Figure 52: Waterfall in the time and frequency domain of the path to surge for each characteristic in Case 3, for round 1.

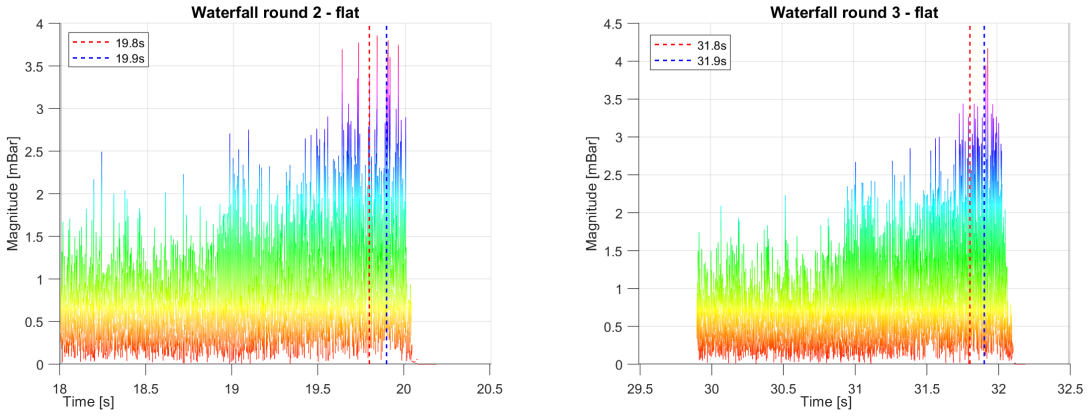

(a) (b)

Figure 53: Waterfall in the time and frequency domain of the path to surge for flat curve characteristics, in round 2 and 3. For Case 3.

C Risk Assessement

NTNU SINTEF

FORM FOR SAFE JOB ANALYSIS

SJA name: Master thesis - Simen Ormstad	
Date: 02.02.2023	Location:
Mark for completed checklist:	Kompressor lab

Participators: Erik Langørgen (Senior Engineer), Simen Ormstad (Student), Ola Pronk (student)		
SJA-responsible: Erik Langørgen		

Specification of work (What and how?):
Master thesis of Simen Ormstad
Experiments conducted at the NTNU Compressor lab.

Risks associated with the work:
Electric motor failure.
Vibrations in pipes.
Temperature and pressure in the compressor rig.

Safeguards: (plan for actions, see next page):
Multiple temperature and pressure sensors on the inlet and outlet.
Manually monitor changes in temperature, pressure, and vibrations.
Adjusting the anti-surge and discharge valve, from closed to fully opened.
Gradually adjusting the compressor rounds per minute from the control panel.

Conclusions/comments:
The laboratory compressor system has been approved by the department.

Recommended/approved	**Date/Signature:**	**Recommended/approved**	**Date/Signature:**
SJA-responsible:	02.02.2023	HSE responsible:	Erik Langørgen

Responsible for work:		Other, (position):	

HSE aspect	Yes	No	NA	Comments / actions	Resp.
Documentation, experience, qualifications					
Known operation or work?	X				
Knowledge of experiences / incidents from similar operations?	X				
Necessary personnel?		X			
Communication and coordinating					
Potential conflicts with other operations?		X			
Handling of an eventually incident (alarm, evacuation)?	X				
Need for extra assistance / watch?		X			
Working area					
Unusual working position		X			
Work in tanks, manhole?		X			
Work in ditch, shaft or pit?		X			
Clean and tidy?	X				
Protective equipment beyond the personal?		X			
Weather, wind, visibility, lighting, ventilation?	X				
Usage of scaffolding/lifts/belts/ straps, anti-falling device?		X			
Work at heights?		X			
Ionizing radiation?		X			
Influence of escape routes?		X			
Chemical hazards					
Usage of hazardous/toxic/corrosive chemicals?		X			
Usage of flammable or explosive chemicals?		X			
Risk assessment of usage?	X				
Biological materials/substances?		X			
Dust/asbestos/dust from insulation?		X			
Mechanical hazards					
Stability/strength/tension?	X				
Crush/clamp/cut/hit?		X			
Dust/pressure/temperature?		X			
Handling of waste disposal?		X			
Need of special tools?		X			
Electrical hazards					
Current/Voltage/over 1000V?	X				
Current surge, short circuit?	X				
Loss of current supply?	X				
Area					
Need for inspection?		X			
Marking/system of signs/rope off?		X			
Environmental consequences?		X			
Key physical security systems					
Work or demounting of safety systems?		x			

where RC is the relative change, V_f is the final value, and V_i is the initial value. The relative change is a measure of how much a quantity has changed in comparison to its initial size.

D Uncertainty of Mass Flow Rate

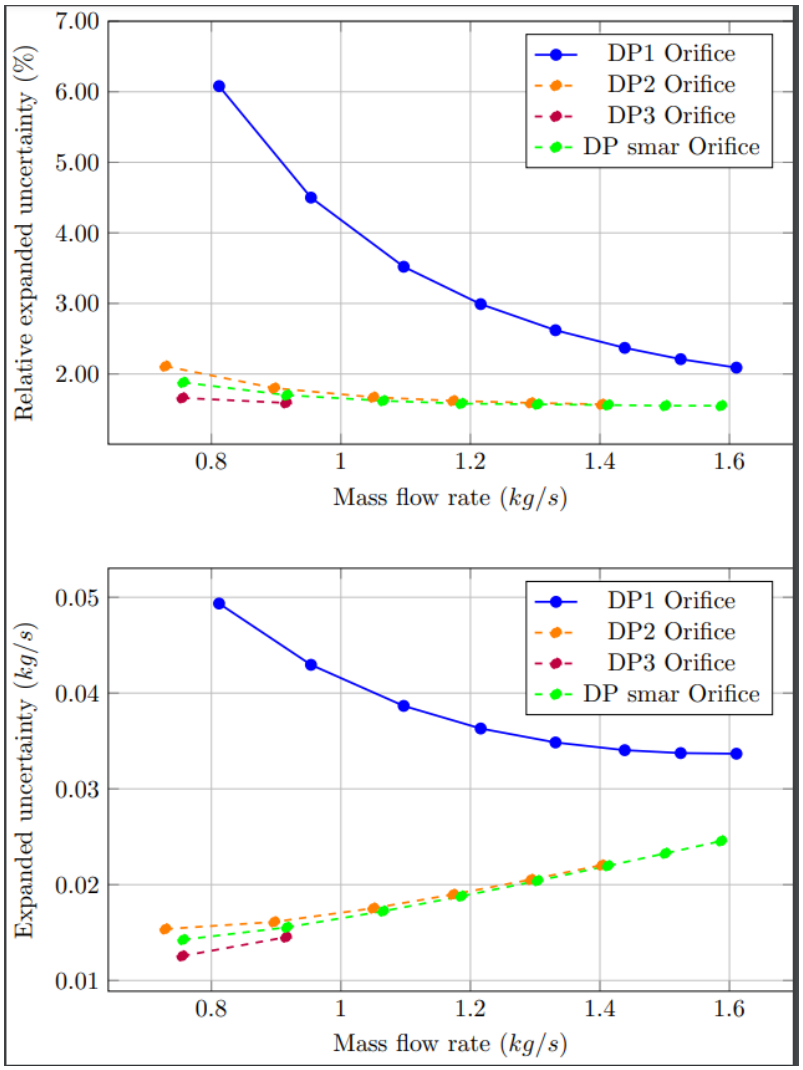

Figure 54: Expanded uncertainty and relative expanded uncertainty of the DP sensors on the orifice.

Figure 54 shows both the expanded uncertainty and relative expanded uncertainty of the DP sensors on the orifice. Only the DP1 sensor is relevant to this thesis, as the others were not used. There is a clear increase in uncertainty as the operating point moves toward lower flow. The calculations behind the figure will not be expanded upon in this thesis. This figure is taken from a master thesis written concurrently with this thesis in the same lab, by Jonas Trovåg Amundsen.

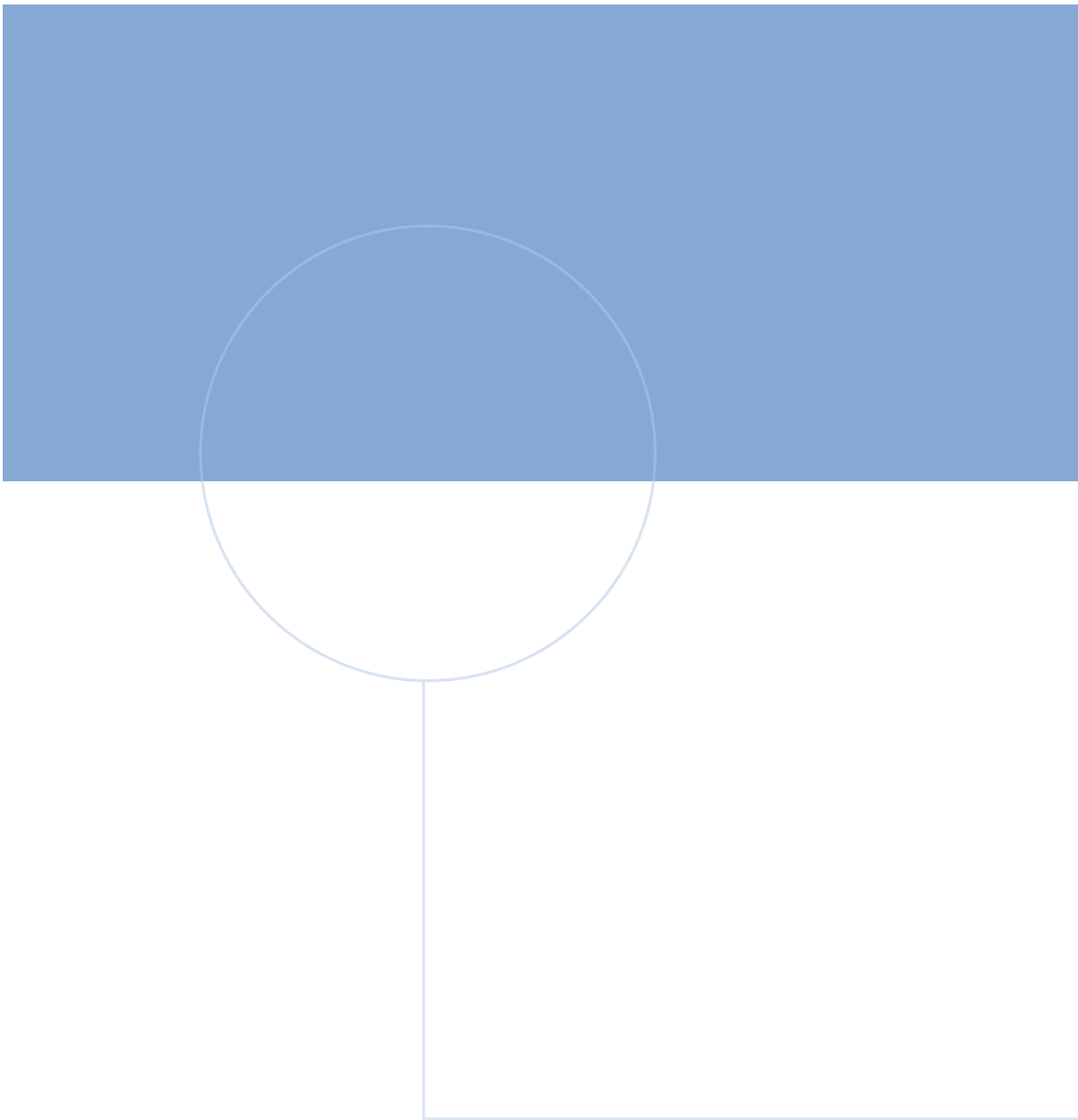

NTNU

Norwegian University of
Science and Technology